

MODIFICATION OF THE $\pi\omega\rho$ VERTEX
IN NUCLEAR MEDIUM AND ITS INFLUENCE
ON THE DILEPTON PRODUCTION RATE
IN RELATIVISTIC HEAVY-ION COLLISIONS

Agnieszka Bieniek

PhD Thesis

Department of Theoretical Physics

The Henryk Niewodniczański

Institute of Nuclear Physics

Polish Academy of Sciences

Kraków

SUPERVISOR: Assoc. Prof. Wojciech Broniowski

This PhD thesis is supported by the Polish State Committee for Science Research, grant 2P03B 13324.

Abstract

In this PhD thesis we analyze the medium modification of the $\pi\omega\rho$ coupling and subsequently discuss its possible influence on the dilepton production rate in relativistic heavy-ion collisions.

The first part of the thesis is devoted to the medium modifications of the $\omega \rightarrow \pi^0\gamma^*$, $\rho^a \rightarrow \pi^a\gamma^*$ and $\pi^0 \rightarrow \gamma\gamma^*$ decays in nuclear matter. We use the relativistic field theory formalism describing modifications of the coupling by one-loop Feynman diagrams with nucleons and $\Delta(1232)$ isobars. For simplicity we work in the leading baryon density approximation and at zero temperature. We consider cases when the decaying particle is at rest or at motion with respect to the medium. The kinematics is considered in the rest frame of the medium. In the medium, the structure of the $\pi\omega\rho$ amplitude is more complex than in the vacuum, which is due to the presence of the additional four-vector describing the velocity of the medium. We investigate the dependence of medium effects on the dilepton invariant mass and observe a sizeable increase of the effective coupling constants compared to their vacuum values. The $\pi\omega\rho$ coupling constant increases by about a factor of 2 for the $\omega \rightarrow \pi^0\gamma^*$ decay and by about a factor of 5 for the $\rho^a \rightarrow \pi^a\gamma^*$ decay. The effect grows with density. Similar conclusions are obtained for a particle moving with respect to the medium.

In the second part of the thesis we apply our model to evaluate the influence of the medium effects on the dilepton production from the Dalitz decays. In the calculations of the dilepton spectrum we use the model of the hydrodynamic expansion of the fire cylinder, including the longitudinal and transverse expansion. In our comparison to the CERES dilepton data we take into account the experimental cuts, which is very important in the detailed numerical analysis. The medium modifications enhance the effect of the Dalitz decays, however, the numbers are still below the experimental data.

It is worth to point out that in the medium the ρ decay due to the isospin degeneracy becomes as important as the ω decay. The main new and original results of the thesis are:

1. Significant in-medium increase of the $\pi\omega\rho$ coupling constant.
2. Large enhancement of the Dalitz $\omega \rightarrow \pi^0\gamma^*$ and $\rho^a \rightarrow \pi^a\gamma^*$ decays in the range $0.2 - 0.6$ GeV of the dilepton invariant mass.

Acknowledgements

First and foremost I have the pleasure to thank my supervisor Dr. Wojciech Broniowski for guiding me through my PhD.

I am also very grateful to Prof. Wojciech Florkowski for many valuable comments.

I would like to thank Prof. Edward Kapuścik, the head of International PhD studies at IFJ PAN for help and for many interesting discussions.

Many warm thanks to the staff and colleagues of Theory Department in the Institute of Nuclear Physics for numerous discussions during my PhD studies.

I warmly thank my sister Marta and Steven Steinke from University of Arizona for linguistic help.

Finally I would like to thank my family for support, and all people who in some way have helped and encouraged me.

Special thanks to Piotr Czerski.

Contents

Introduction	11
I Modification of the $\pi\omega\rho$ coupling in nuclear medium	19
1 Modification of Hadrons in medium	21
1.1 The Walecka model	22
1.2 Quark condensate in medium	23
1.3 Brown-Rho scaling	24
1.4 QCD sum rules	24
1.5 Predictions from dispersion relations	25
1.6 Lowering of the position of ρ^0 peak	26
1.7 Modification of coupling constants	27
2 $\pi\omega\rho$ vertex in nuclear medium	29
2.1 Our model	30
2.2 Decays of particles at rest with respect to the medium	38
2.3 Decay of particles moving with respect to the medium	47
3 Summary of Part I	53
II Dilepton production rate	55
4 Electromagnetic signals from hot and dense matter	57
4.1 Overview of experimental measurements	59
4.1.1 CERES/NA45 experiments	60
4.1.2 HELIOS experiments	61
4.1.3 NA38/NA50 experiments	63
4.1.4 Dilepton spectra at BEVALAC energies	64
4.1.5 Other experiments	65

4.2	Overview of theoretical models	65
5	Formalism of the dilepton production from vector mesons	69
5.1	Vector Dominance Model (VDM)	70
5.2	Dalitz decays	71
5.3	Model of the hydrodynamic expansion of the fire-cylinder	73
5.4	Kinematics for dilepton yield	74
6	Results of our model	83
7	Summary and discussion	87
8	Appendices	91
8.1	Appendix A	91
8.2	Appendix B	92
8.3	Appendix C	94
8.4	Appendix D	96

Introduction

Physics of ultra-relativistic heavy-ion collisions is a quickly developing branch of science which allow us to investigate the properties of nuclear matter in terms of elementary interactions. The production of dileptons (e^+e^- , $\mu^+\mu^-$) is one of the most important probes in studying the dynamical evolution of the nuclear collision processes. Since they do not interact strongly, the dileptons escape unthermalized from the hot and dense matter during all stages of the evolution. A major source of dileptons comes from the direct and the Dalitz decays of meson resonances in particular the ω , ρ , η , η' or ϕ . The properties of vector mesons such as masses or widths, are known to be significantly modified in nuclear matter, [1, 2, 3]. These in-medium properties play an important role in the low mass dilepton production region, namely between 0.2 – 0.6 GeV of invariant masses, covered recent heavy-ion collision experiments, [4, 5, 6]. The dilepton production enhancement in central nucleus-nucleus collisions in the low-mass region has been a topic of great interest in the last years, [7, 8, 9, 10, 11]. This phenomenon is frequently explained by assuming that the vector meson spectral functions undergo substantial modifications through the strong interactions with the nucleons in the medium. Many research groups search for a theoretical description of the low-mass dilepton enhancement however, a convincing explanation has not been reached and the problem still remains a major puzzle in relativistic heavy-ion physics.

Trying to explain this relevant problem, in this thesis we investigate modifications of the $\pi\omega\rho$ coupling constant in the context of the ω and ρ Dalitz decays. We analyze these decays in nuclear matter applying a relativistic hadronic framework incorporating nucleons and $\Delta(1232)$ isobars. We find that the $\pi\omega\rho$ coupling constant for $\omega \rightarrow \pi^0 e^+ e^-$ and $\rho^a \rightarrow \pi^a e^+ e^-$ decays are considerably enhanced by the medium as compared to the vacuum values. We observe an enhancement by about a factor of 2 for the ω meson and by about a factor of 5 for the ρ meson. We have to stress that the Dalitz decay of the ρ meson is found to be equally important to the omega decay, [12]. The in-medium-modified $\pi\omega\rho$ coupling constant increases the corresponding widths

of considered decays. In order to estimate the dilepton yields we use the vector dominance model (VDM) and include the effect of the expansion of the medium. Next, we compare our model results to the dilepton yield from the CERES Pb+Au experiment in the low-mass region carefully including the experimental kinematic cuts. Finally, our results show that medium effects from the ω and ρ Dalitz decays are significant and about two times larger compared to the vacuum.

Highlights of the experimental situation

The physics of ultra-relativistic heavy ion collisions, *i.e.*, collisions of atomic nuclei in which the center-of-mass energy per nucleon is much larger than the nucleon rest mass, has been studied experimentally with immense intensity. First experiments have been performed at the Alternating Gradient Synchrotron (AGS) in the Brookhaven National Laboratory (BNL) and at the Super Proton Synchrotron (SPS) at CERN, where ion beams were accelerated with the center of mass energies around $\sqrt{s} \sim 5$ A GeV and $\sqrt{s} \sim 20$ A GeV, respectively.

In 2001 the first data were collected from the Relativistic Heavy Ion Collider (RHIC) at BNL at the energy of $\sqrt{s} \sim 200$ A GeV. Between the years 2001-2004 the next three runs took place. In the near future heavy ions will also be injected into the CERN Large Hadron Collider (LHC) reaching the energy of $\sqrt{s} = 10$ A TeV. The principal goal of experimental and theoretical initiative in ultra-relativistic heavy-ion collisions is the observation and understanding the physics of hot and dense medium.

Many probes have been proposed to analyze the behavior of hot and dense hadronic matter. Among these probes the dileptons stand out, because they couple directly to vector mesons and interact only electromagnetically. Therefore they are likely to bring information about the hot and dense matter formed in the early stages of nuclear collisions. A schematic view of characteristic dilepton sources in ultrarelativistic heavy-ion collisions is given in Fig. 1. One can distinguish three basic regions with respect to the invariant mass of the dilepton pair.

In the high-mass region, $M_{e^+e^-} = 3$ GeV, dileptons come dominantly from hard processes such as the Drell-Yan annihilation occurring in the early stage, where the excited hadronic system is far from thermal equilibrium. After rapid thermalization the QGP phase may be established, where the dilepton production proceeds predominantly via the quark-antiquark annihilation. Upon expansion and cooling, the QGP is converted into a hot hadron gas. At this stage dileptons are radiated from pion and kaon annihilation processes as well as other collisions between various hadrons. In contrast to the light vector mesons (ω , ρ), the lifetime for the heavy quarkonium

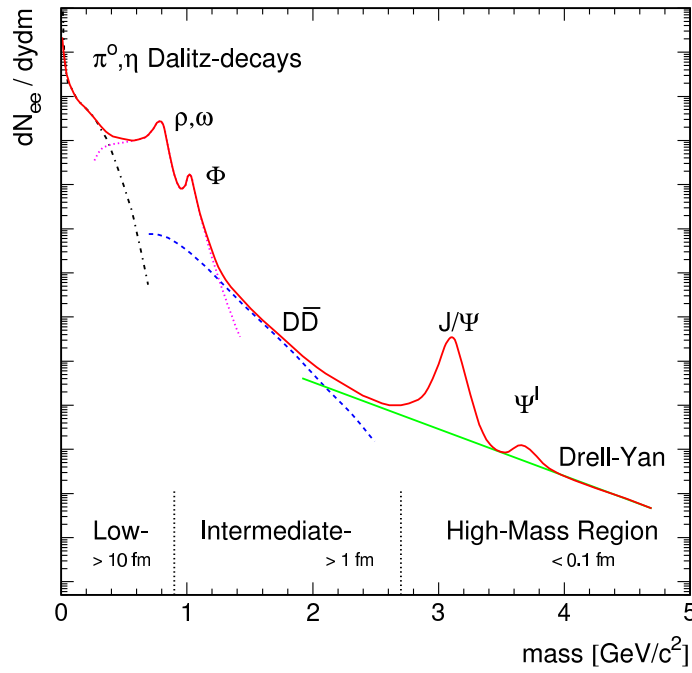


Figure 1: Major dilepton sources as a function of invariant mass in ultrarelativistic heavy-ion collisions. In the high-mass region above invariant masses $M_{e^+e^-} = 3$ GeV, dileptons come mostly from hard Drell-Yan annihilation processes. Here strong J/Ψ suppression and Ψ' abundance are interpreted as a sign of color deconfinement. In the intermediate-mass region between 1 – 2.5 GeV, the thermal signal from QGP could be related to the observation of associated $D\bar{D}$ production. In the low-mass region below 1 GeV, dileptons originate from Dalitz decays of neutral mesons such as π^0 , η , $\eta' \rightarrow e^+e^-\gamma$, $\omega \rightarrow \pi^0 e^+e^-$, and from direct decays, ω , ρ , $\phi \rightarrow e^+e^-$. This region is very sensitive to hadron modifications in the nuclear matter.

states such as J/Ψ and Υ is substantially longer than the typical life-time in the hadronic fireball. Therefore these mesons will mostly decay after freezeout, and hence will not feel the medium.

The intermediate mass region, above ~ 1.5 GeV, might be proper to observe a thermal signal from the plasma radiation, because QGP can only be formed at higher temperatures than a hadronic gas. This signal could be revealed by the observation of the associated $D\bar{D}$ production in this intermediate region.

Next, when the freezeout stage is reached, the dominant sources are hadronic resonances as well as Dalitz decays, mostly from π^0 , η , ω , and ρ mesons. The two-body annihilation processes are dynamically enhanced through the formation of light vector meson resonances such as the ρ , ω , and ϕ mesons, which directly couple to

lepton pairs. Thus, the invariant mass distribution of the lepton pairs reflects the mass distribution of the vector mesons at the moment of decay. Therefore, vector mesons, possibly modified by medium effects, play an important role in the measurement of dilepton rates in relativistic heavy-ion reactions. All these above-mentioned dominant sources feed into the low mass region, $M_{l+l-} \leq 1$ GeV, which is particularly sensitive to in-medium modifications of the light hadrons.

The experimental measurements of the dilepton spectra in relativistic heavy-ion collisions have mainly been carried out at the CERN SPS by the CERES/NA45 (low-mass region)[4, 13, 14], HELIOS-3 (low- and intermediate-mass region) [5] and NA38/NA50 (intermediate- and high-mass region) [15, 16, 17]. In the near future, at RHIC and CERN-SPS, dilepton spectra will be measured by the PHENIX and NA60 [18] collaborations, respectively. At much lower bombarding energies, dilepton data have also been taken by the DLS collaboration at SIS (GSI) [19, 20], where only the low-mass region up to the kinematical limit of around 1 GeV may be accessible. These experiments focused on the role of high baryon density.

Recently, the CERES [4] and HELIOS [5] collaborations have observed that central nucleus-nucleus collisions exhibit a strong enhancement of low-mass dilepton production as compared to proton-nucleus reactions. The data analysis is based on the so-called *hadronic cocktail model* which works very well to describe the proton-nucleus data. On the other hand, the hadronic cocktail strongly underestimates the dilepton yield from nucleus-nucleus collisions. The model is based on data from proton-induced collisions which are scaled with the multiplicity of charged particles. A lot of efforts have been undertaken in order to understand the phenomenon of the low-mass enhancement.

In theoretical attempts to address the problem, the increased dilepton yield in nucleus-nucleus collisions was attributed to enhanced ρ -meson production via $\pi^+\pi^-$ annihilation. Thus, many theoretical groups, [21, 22, 23], have included the $\rho \rightarrow \pi^+\pi^-$ process within different models for the space-time evolution of nucleus-nucleus reactions. Their calculations are based on the vacuum meson properties, and all results are in disagreement with the data. This has led to the suggestion of various medium effects, such as the reduction of the vector meson masses, that might be responsible for the observed enhancement. Brown and Rho suggested the hypothesis that the vector meson masses drop in the medium according to a simple scaling law, [1, 7].

There are also many approaches based on QCD sum rules [24, 25], which confirm the scaling hypothesis.

The conclusion from the existing studies is that although conventional mechanisms are sufficient to account for the dilepton spectra from proton-induced reactions, medium effects are needed to explain the low-mass dilepton enhancement observed in nucleus-nucleus reactions. Thus, in this thesis we examine the in-medium $\pi\omega\rho$ vertex and its large influence on the dilepton production rate in relativistic heavy-ion collisions. We believe that our model together with other medium effects may resolve the dilepton puzzle. This is the main reason of our study.

Organization of the Thesis

The first part of this dissertation is devoted to the modification of hadron properties, in particular the $\pi\omega\rho$ vertex, in the presence of nuclear medium.

As the introduction to the subject, in Chapter 2 we first review some theoretical approaches describing the medium modifications of hadron properties. Next, we present our original analysis, describing our model (section 2.1). The model is based on fully relativistic hadronic theory where mesons and nucleons interact with each other and with the Δ isobars. The presentation concentrates on Dalitz decays such as $\pi^0 \rightarrow \gamma\gamma^*$, $\omega \rightarrow \pi^0\gamma^*$ and $\rho^a \rightarrow \pi^a\gamma^*$. In such processes the $\pi\omega\rho$ coupling constant appears. We present propagator, vertices for the interactions with and without Δ resonance, and the in-medium structure of the $\pi\omega\rho$ amplitude. This structure is more complicated because of the additional four-vector, the four-velocity of the medium. We analyze the Dalitz decays at rest, section 2.2, as well at motion, section 2.3, with respect to the medium. In the case when the decaying particles are moving with respect to the medium we consider the kinematics in a convenient and non-textbook way. The kinematics is usually analyzed in the rest frame of the decaying particle, whereas we consider it in the rest frame of the nuclear medium (with the four-velocity of the medium $u = (1, 0, 0, 0)$). We investigate the dependence of medium effects in the dilepton invariant mass and observe their influence on the effective $\pi\omega\rho$ coupling constant compared to its vacuum value. We point out that the $\pi\omega\rho$ coupling constant is considerably enhanced in the presence of the nuclear medium for both the ω and ρ Dalitz decays. The ω and ρ can have two polarizations. When the decaying particle moves with respect to the medium each polarization behaves differently, thus the properties of decaying particle are different. We calculate the dependence of the width for both the transverse and longitudinal polarizations as a function of the invariant mass of the dileptons, and show significant medium effects. Finally, in Chapter 3 we discuss how nuclear matter influences the $\pi\omega\rho$ coupling constant in the previously mentioned Dalitz processes.

In the second part of the thesis, we focus on applying our model to the production of dileptons in relativistic heavy-ion collisions. We begin this part with a review of major dilepton experiments and some theoretical models connected to the low-mass region. This part starts out by describing the experimental measurements of the dilepton yield. Here we concentrate on the experimental background and discuss relevant dilepton experiments, mainly at CERN SPS in the proton-nucleus and nucleus-nucleus reactions. We discuss results at high bombarding energies of 158 A GeV or 200 A GeV and at the lower energies of 40 A GeV and 1 – 5 A GeV. We focus on the low-mass region, because here in particular the experimental results are in disagreement with many theoretical models. The experimental data are usually compared to the hadronic cocktail model, therefore we present a short description of this approach. In section 4.2 of Chapter 4, we describe the most popular theoretical explanations related to the low-mass dilepton enhancement, based on the in-medium modifications of vector mesons.

In order to estimate the dilepton production rate from the Dalitz decays of vector mesons we use the vector dominance model (VDM) reviewed in section 5.1 of Chapter 5. Section 5.2 discusses in detail the structure of the three-body Dalitz decays. In section 5.3 we describe briefly the model considered for the hydrodynamic evolution of the fire cylinder from Ref. [26, 27]. Next, in section 5.4, we present details of our formalism used to calculate the dilepton production from the Dalitz and direct decays of the ω and ρ mesons. We use the experimental acceptance cuts in our analysis. It is quite nontrivial how to construct and include these cuts in the calculations, therefore in many other theoretical works the acceptance cuts are frequently not taken into account.

In section 5.5 we present our numerical results, starting from calculations without expansion of the fireball and without the CERES acceptance function. Our plots are done for two typical temperatures of the fireball. Next, we present the dilepton yield from direct and Dalitz decays with expansion and acceptance cuts. We compare our numerical results to the CERES experimental data also for two different temperatures.

In the medium we observe a significant enhancement for the Dalitz decays of the ω and ρ mesons in the dilepton mass region 0.2 – 0.6 GeV compared to the vacuum case.

Although the modification of the $\pi\omega\rho$ vertex increases the contribution from the Dalitz decays, the obtained yields alone fall short of describing the data. Yet, they help by contributing more to the theoretical curves, and together with other effects not considered here (such as dropping masses, broadening widths, or Dalitz decays

of η and η' mesons), may help to explain the long standing problem of the low-mass dilepton enhancement seen in relativistic heavy-ion collisions.

The new and original material of this thesis is contained in Chapter 2, section 5.4 and Chapter 6, while Chapter 1, Chapter 4 and sections 5.1, 5.2, 5.3 contain useful reviews necessary for the integrity of the text.

Part I

Modification of the $\pi\omega\rho$ coupling in nuclear medium

Chapter 1

Modification of Hadrons in medium

As mentioned in the Introduction, in heavy-ion collisions the particle production is related to the evolution of hot and dense matter. Heavy-ion collisions provide the only way to compress and heat up nuclear matter in the laboratory conditions. From these heavy-ion data we obtain important information useful in construction of models for the early universe, supernova explosions or neutron stars. In the so-called *relativistic regime*, at energies above 1 GeV per nucleon, heavy-ion collisions are likely to yield particle densities of the order of a few times the normal nuclear matter density. In such system the particles cannot propagate completely freely (the Compton wavelength is comparable with mean free paths of particles). In this situation we expect that in hot and dense environment the particle properties, *i.e.* their masses, widths, or coupling constants, are changed and these *in-medium modifications* may lead to experimentally observed phenomena.

The problem of how the properties of hadrons change in hadronic or nuclear matter in comparison to their free values has attracted a lot of attention [2, 3, 8, 9, 24, 25, 28, 29, 30, 31, 32, 33, 34, 35, 36, 37, 38, 39, 40, 41, 42]. Till a few years ago there were only theoretical predictions [28, 29, 30], for the in-medium modifications. At present we also have some indirect experimental evidence from the dilepton production in hadronic collisions, (which we discuss in more detail in the Part II, Chapter 4) [4, 5] or from data on the $\pi^+\pi^-$ correlations from STAR, where the ρ meson peak moves to lower masses [43]. The existing calculations are based on simple scaling of masses [1, 7], numerous hadronic models [2, 3, 8, 9, 31, 32, 33, 34, 35, 36, 37, 38, 39, 40, 41], or QCD sum rule techniques [24, 25, 42]. More fundamental predictions are based on low-density expansion and dispersion relations [44, 45, 46]. In all these calculations properties of hadrons are changed by the presence of the medium through strong interactions with nucleons from the medium.

Below we will briefly review major theoretical approaches for in-medium properties of vector mesons, namely, ρ , ω , and ϕ mesons.

1.1 The Walecka model

A simple and very illustrative approach showing the effects of medium modifications is Quantum Hydrodynamics (QHD) [2, 41] in its simplest form known as the Walecka model. It is based on the mean-field theory of hadrons, where the scalar and vector mean fields generated by the nucleon sources are themselves self-consistently responsible for the modification of the nucleon mass. The Lagrangian density for the Walecka model is

$$\begin{aligned}\mathcal{L} = & \bar{\Psi} [\gamma_\mu (i\partial^\mu - g_v V^\mu) - (M - g_s \phi)] \Psi + \frac{1}{2} (\partial_\mu \phi \partial^\mu \phi - m_s^2 \phi^2) \\ & - \frac{1}{4} F_{\mu\nu} F^{\mu\nu} + \frac{1}{2} m_v^2 V_\mu V^\mu + \delta\mathcal{L},\end{aligned}\tag{1.1}$$

where Ψ is the baryon field of mass M , ϕ is the neutral scalar-meson field with mass m_s , V^μ is the neutral vector meson field of mass m_v , and $F^{\mu\nu} \equiv \partial^\mu V^\nu - \partial^\nu V^\mu$. The term $\delta\mathcal{L}$ contains renormalization counterterms. The nucleons interact via the exchange of isoscalar mesons with the coupling of the scalar field ϕ to the baryon scalar density $\bar{\Psi}\Psi$, and the vector field V^μ to the conserved baryon current $\bar{\Psi}\gamma_\mu\Psi$, obtained through minimal substitution. Because the exact solutions to the field equations are very complicated, a mean-field approximation is used. In a mean-field approximation, the meson field operators are replaced by their expectations values, which are classical fields:

$$\begin{aligned}\phi & \rightarrow \langle\phi\rangle \equiv \phi_0, \\ V_\mu & \rightarrow \langle V_\mu\rangle \equiv \delta_{\mu 0} V_0.\end{aligned}\tag{1.2}$$

Now the mean-field equations can be solved exactly with the solution becoming increasingly valid with increasing baryon density. Usually, the mean-field equations are solved in two approximations. In the mean-field theory one calculates a baryon self-energy which is generated by the presence of all the nucleons in the occupied Fermi sea, and the effect of the Dirac sea is neglected. In contrast, in the relativistic Hartree approximation one includes the contribution to the baryon self-energy arising from the occupied Fermi sea as well as from the full Dirac sea. In consequence, the baryon self-energy diverges in the relativistic Hartree approximation and must be renormalized. In both approximations, the mean scalar meson field ϕ_0 is responsible for a shift of the nucleon mass M^* in the nuclear medium relative to its vacuum value M . In

contrast to the ground-state expectation value of the vector field, which is determined by the conserved baryon density, ρ_B :

$$V^0 = \frac{g_v}{m_v^2} \langle \bar{\Psi} \gamma^0 \Psi \rangle = \frac{g_v}{m_v^2} \rho_B. \quad (1.3)$$

The expectation value of the scalar field, and consequently the effective mass of the nucleon, is a dynamical quantity that must be determined self-consistently from the equations of motion

$$M^* = M - g_s \phi_0 = M - \frac{g_s^2}{m_s^2} \langle \bar{\Psi} \Psi \rangle = M - \frac{g_s^2}{m_s^2} \rho_s, \quad (1.4)$$

where $\rho_s = \langle \bar{\Psi} \Psi \rangle$ is the scalar density of the nucleons. Since $\rho_s > 0$, from the above equation we see that indeed nucleon mass, M^* , is lower in medium than in vacuum.

The model has already been used extensively in calculations of nuclear matter and finite nuclei. The saturation of nuclear matter and the strong spin-orbit splitting observed in finite nuclei were among the first successes of the model [41, 47, 48, 49]. The model has also been used with considerable success to analyze such diverse topics as collective modes in nuclear matter, isoscalar magnetic moments, and electroweak and hadronic responses from finite nuclei.

1.2 Quark condensate in medium

The authors of Ref. [50] have studied quark and gluon condensates in nuclear matter. These condensates are expectation values of local composite operators such as $\bar{q}q$ and $G_{\mu\nu}^a G^{a\mu\nu}$, where q is an up or down quark field and $G_{\mu\nu}^a$ is the gluon field-strength tensor. The authors of Ref. [50] focused on describing the properties of hadrons in nuclear matter in terms of *in-medium* quark and gluon condensates, which are shifted from their vacuum values. The condensates are analyzed in the ground state of nuclear matter. Simple expressions for these quantities, which are model independent to first order in the nucleon density, have been developed.

As a result, the ratio of the in-medium quark condensate to its vacuum value is given by

$$\langle \bar{q}q \rangle_{\rho_N} = \langle \bar{q}q \rangle_{vac} \left(1 - \frac{\sigma_N \rho_N}{m_\pi^2 f_\pi^2} \right), \quad (1.5)$$

where $\langle \bar{q}q \rangle_{\rho_N}$ and $\langle \bar{q}q \rangle_{vac}$ are the medium and vacuum values of the quark condensate, m_π is the pion mass and f_π is the pion decay constant. The quark condensate at low densities is related to the nucleon σ term, σ_N , which can be expressed as

$\sigma_N = \langle N | m \bar{q}q | N \rangle$, where m is the current mass of light quarks. Eq. 1.5 shows the in-medium quark condensate to first order in the nucleon density. There are higher-order corrections, see Ref. [50]; therefore, the model-independent results are valid at sufficiently low nucleon densities. To first order in the nucleon density, the relationship of the in-medium quark condensate to its vacuum value depends on the values of the pion mass (138 MeV), the pion decay constant (93 MeV) and the σ term (about 45 MeV). The value of nucleon density at saturation is $\rho_N = 0.17 \text{ fm}^{-3}$. Depending on the precise value of the σ term, the quark condensate is reduced considerably at nuclear matter saturation density - it is roughly 25 – 50% smaller than the vacuum value, thus the shift in the quark condensate is large. This description is complementary to the Walecka model from QCD ($M \sim \langle \bar{q}q \rangle$). On the other hand, the finite-density effects modify the gluon condensate to a much smaller extent than they do for the quark condensate. The decrease in the gluon condensate at nuclear matter saturation density is around 5%. Hence, it does not affect the particle properties as much.

1.3 Brown-Rho scaling

Brown and Rho (BR) have suggested the hypothesis that the hadron masses drop in the medium according to a simple scaling law [1], given by

$$\frac{m_N^*}{m_N} = \frac{m_\rho^*}{m_\rho} = \frac{m_\omega^*}{m_\omega} = \frac{f_\pi^*}{f_\pi}, \quad (1.6)$$

where f_π is a pion decay constant and the medium-modified parameters are indicated by asterisks. This hypothesis is based on phenomenological implementation of the restoration of chiral symmetry in the framework of an effective theory.

At least qualitatively, this scaling conjecture is supported by studies based on the QCD sum rule approach, as well as by other hadronic models [2, 3, 31, 8, 9, 32, 33, 34, 35, 36, 37, 38, 39, 40, 41].

1.4 QCD sum rules

A natural and direct use for in-medium condensates is made in QCD sum rule calculations of hadronic properties in nuclear matter. This approach can be used to predict in-medium spectral properties (effective masses or self-energies) of baryons and mesons.

The QCD sum rule approach aims to understand the physical current-current correlation functions in terms of QCD. It is done by relating the observed hadron

spectrum to the non-perturbative vacuum structure of QCD. Through the use of this technique Hatsuda and Lee, [24] have extracted the medium dependence of the non-strange vector-meson masses. They have obtained the following result

$$\frac{m_{\rho,\omega}^*}{m_{\rho,\omega}} \approx 1 - 0.18\left(\frac{\rho_N}{\rho_0}\right), \quad (1.7)$$

and

$$\frac{m_\phi^*}{m_\phi} \approx 1 - 0.15a\left(\frac{\rho_N}{\rho_0}\right) \quad (1.8)$$

where a is the nucleon strangeness content, $a = \langle N|\bar{s}s|N\rangle/\langle N|\bar{q}q|N\rangle$, taken to be $a = 0.17$. The ρ and ω meson masses decrease significantly with density due to the strong density dependence of the light quark condensate. Since the strange quark condensate does not change much in nuclear media as a result of the small nucleon strangeness content, the ϕ meson mass shows a weaker density dependence. The fact that these masses decrease as density increases has been taken as a confirmation of the Brown-Rho scaling [1].

The QCD sum rules for vector mesons were reanalyzed in Ref. [51]. The uncertainties in various in-medium quark condensates were assessed using the Monte-Carlo method analysis. It was found that at normal nuclear matter density $m_\rho^*/m_\rho = 0.78 \pm 0.08$, in nice agreement with the results of Refs. [24]. In Ref. [52] a decrease of the ρ meson mass with increasing density like that of Ref. [24] has also been obtained. The predictive power of the QCD sum rule approach was addressed in Ref. [25] taking into account the possible modifications of the ρ meson mass and width. In this approach the ρ meson spectral function was parameterized by a simple Breit-Wigner form containing two fitting parameters, the pole mass and the width, and the values for mass and width are determined by requiring that the QCD sum rules are satisfied. It was found that in the case of vanishing width, the ρ meson mass indeed decreases in nuclear matter. On the other hand if the width increases it is then possible to satisfy the QCD sum rules with a constant or even an increasing ρ meson mass. The predictive power of the QCD sum rule approach thus depends on how well one can constrain the phenomenological ρ meson spectral function in the nuclear medium.

1.5 Predictions from dispersion relations

The in-medium mass shift and broadening of the width are due to interactions of the hadron with the medium. Thus, one can use phenomenological information on this interaction to calculate the mass shifts. The authors of [53] have used the result that

the mass shift of a particle in medium is related to the forward scattering amplitude, f_{sc} , of this particle on the constituents of the medium.

This gives the mass shift

$$\Delta m = -2\pi \frac{\rho}{m} \text{Re} f_{sc} \quad (1.9)$$

where m is the vacuum mass of the particle and ρ denotes the density of the medium. The width broadening is given by

$$\Delta \Gamma = \frac{\rho}{m} k \sigma, \quad (1.10)$$

where k is the particle momentum and $k\sigma = 4\pi \text{Im} f_{sc}$. Equations 1.9 and 1.10 are correct when the particle's momentum k is larger than few hundred MeV, and $\text{Re} f_{sc}$ fulfils the requirement $|\text{Re} f_{sc}| < d$, (where d is the distance between medium constituents). Additionally the main part of the scattering should proceed through small angles, less than 1, and the medium constituents should have some momentum distributions, such as Fermi-Dirac or Bose-Einstein distributions, for finite temperatures and chemical potentials. In such cases, in the right-hand sides of Eqs. 1.9 and, 1.10 an averaging over the momentum distribution of constituents must be performed. Thanks to this approach one may formulate explicitly the applicability conditions discussed above. When gas in thermal equilibrium plays the role of the medium, the equivalents of Eqs. 1.9 and, 1.10 can be derived in the framework of the thermal field theory.

Using this approach, authors of Ref. [53] have estimated ρ meson mass shift and width broadening in the case of ρ -mesons produced in heavy-ion collisions, with following conclusions: For ρ -mesons produced in high energy heavy ion collisions the mass shift is small, but the width broadening is so large that one can hardly observe a ρ -peak in e^+e^- or $\mu^+\mu^-$ mass distributions. In low energy heavy-ion collisions a ρ -peak may be observed in e^+e^- or $\mu^+\mu^-$ mass distributions as a broad enhancement approximately at the position of ρ -mass.

1.6 Lowering of the position of ρ^0 peak

Experimental indications for in-medium physics also come from RHIC [43], where the data obtained by the STAR collaboration have been interpreted as the lowering of the position of the ρ^0 meson peak, see Fig. 1.1. This is the first direct measurement of $\rho(770)^0 \rightarrow \pi^+\pi^-$ in heavy-ion collisions. The important observation is that the ρ^0 mass is lower in peripheral Au+Au collisions than in p+p collisions. Apart from

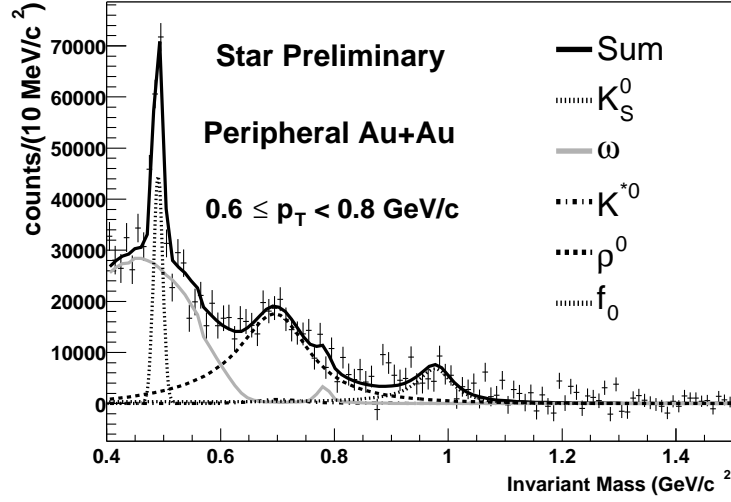


Figure 1.1: The $\pi^+\pi^-$ invariant mass distributions for peripheral Au+Au interactions. The ρ peak is around 700 MeV, much lower than the vacuum value.

the dynamical interactions with the surrounding matter, interference between various $\pi^+\pi^-$ scattering channels, phase space distortions due to the rescattering of pions forming ρ^0 , and Bose-Einstein correlations between ρ^0 decay daughters and pions in the surrounding matter are among possible explanations for the apparent change of the ρ^0 meson. Hopefully, more detailed information will be provided by future correlation experiments.

1.7 Modification of coupling constants

Meson properties are changed due to strong interactions with nucleons of the medium. If the mass and widths of hadrons can be significantly modified, one can expect that also the coupling constants are altered. There are numerous studies of mesonic two-point functions in the literature, Ref. [54], which in general contained medium modified mass M^* and medium modified width Γ^* , but only a few devoted to meson three-point functions. In their studies of the ρ meson in-medium spectral function in Ref. [8], Herrmann, Friman and Norenberg have analyzed the $\rho\pi\pi$ vertex for the ρ at rest with respect to the medium. They have considered the above vertex on the basis of a hadronic model with the Δ isobar and with nonrelativistic couplings. Song and Koch in Ref. [55] have taken into account the temperature effects on the $\rho\pi\pi$ interaction. Krippa in Ref. [56] has computed the effects of density on chiral mixing of meson three-point functions. The authors of Ref.[57, 58, 59, 60] have analyzed the

$\omega \rightarrow \pi\pi$ and $\rho \rightarrow \pi\pi$ decays in nuclear medium. They have studied the $\rho\pi\pi$ vertex in the fully relativistic framework with relativistic interactions, incorporating nucleons and $\Delta(1232)$ isobars, and found that the medium effects on the $\rho\pi\pi$ constant are large, and dominantly come from the processes where the Δ is excited in the intermediate state. This has immediate consequences for the direct decay of the ρ meson into dileptons (such as broadening of width).

An important factor brought in by the presence of the medium is that processes which are forbidden in the vacuum by symmetry principles are now made possible. In this work we concentrate on the $\pi\omega\rho$ coupling constant and analyze its significance for the Dalitz decays of vector mesons.

Chapter 2

$\pi\omega\rho$ vertex in nuclear medium

So far we have discussed major theoretical approaches related to the medium modifications of particle properties. In this chapter we begin the original material of the thesis. We focus on the $\pi\omega\rho$ coupling constant and its medium modifications. The $\pi\omega\rho$ vertex appears in such processes as: $\omega \rightarrow \pi^0\gamma^*$, $\rho^a \rightarrow \pi^a\gamma^*$, and $\pi^0 \rightarrow \gamma\gamma^*$, see Fig 2.1. We expect that medium effects may have a significant influence and may

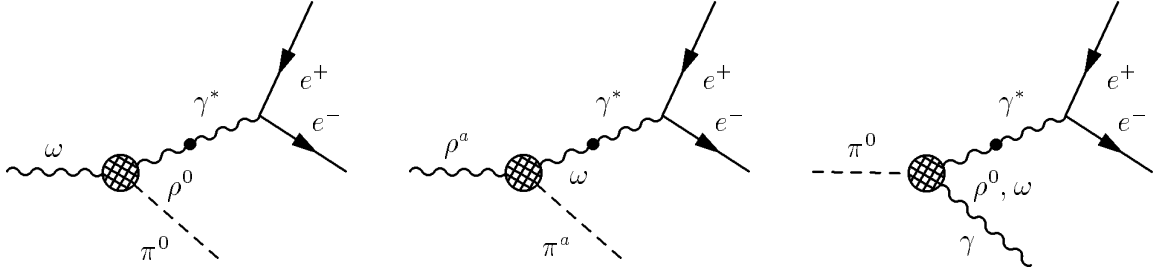


Figure 2.1: The physical processes where the $\pi\omega\rho$ vertex appears. Wavy lines indicate the ρ or ω , dashed lines the pions, the hatched blob indicates the medium-modified vertex, the black dot is equal to $\frac{em_\omega^2}{g_\omega}$ or $\frac{em_\rho^2}{g_\rho}$ as follows from the Vector Dominance Model (VDM).

affect the existing calculations based solely on the vacuum values. Our calculation of the in-medium $\pi\omega\rho$ vertex is made in the framework of a fully relativistic hadronic theory, where mesons interact with nucleons and Δ isobars. Among the baryon resonances, the Δ is most important due to the small $\Delta - N$ mass splitting and a large value of the $\pi N\Delta$ coupling constant. In our investigation we work at zero temperature to obtain the vertices of Fig. 2.1, at least as a first approximation. We use the *leading-density* approximation, which makes the calculation simpler, as no integration over the nucleon momenta is necessary. This Chapter is divided into three sections. In section 2.1 we present our model with all the needed diagrams, propagators and

vertices for interactions of mesons with nucleons and with Δ resonances which we use in our calculations. Also, the tensor structure of the $\pi\omega\rho$ vertex is presented. Next, we look at how the effective coupling constant is changed compared to the vacuum value. First, in section 2.2 we analyze our decays in the rest frame with respect to the medium. Later, in section 2.3, keeping non-zero three momenta of the ω and ρ we look separately at the longitudinal and transverse polarizations. In both cases we observe that the effective coupling constant is significantly enhanced in the presence of nuclear matter.

2.1 Our model

In our analysis we apply a conventional hadronic model with meson, nucleon and Δ degrees of freedom. This model is similar to the Walecka Model, which we have discussed in Chapter I. In Fig. 2.2 the considered diagram for the $\pi\omega\rho$ coupling consists of two parts, the vacuum one and the induced by the medium.

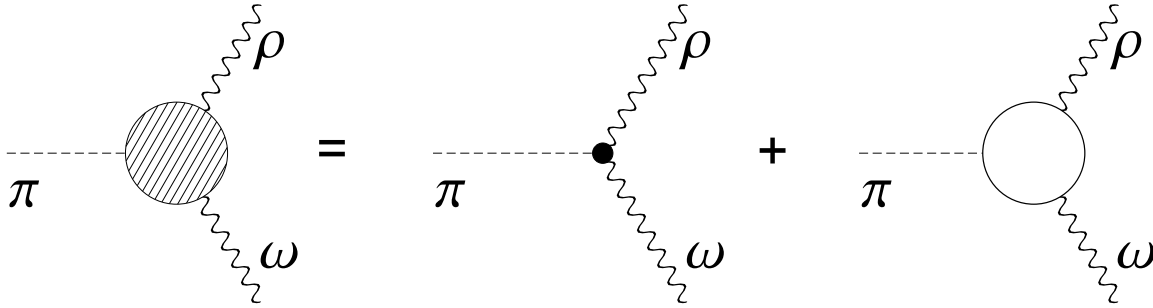


Figure 2.2: The full $\pi\omega\rho$ vertex consisting of two parts, the vacuum part and the medium part, respectively.

There are three types of in-medium diagrams, see Fig. 2.3: diagrams with three nucleons, Fig. 2.3 (a), two nucleons and one Δ isobar, Fig. 2.3 (b), and with one nucleon and two Δ isobars, Fig. 2.3 (c).

The diagrams of interest are those which include at least one nucleon, because only these depend on the baryon density, carried by the Fermi sea. Since the Δ isobar has a large coupling constant it has a large contribution to the considered processes. The diagram with three Δ is not considered, because such a diagram corresponds to vacuum polarization effects, which are not considered.

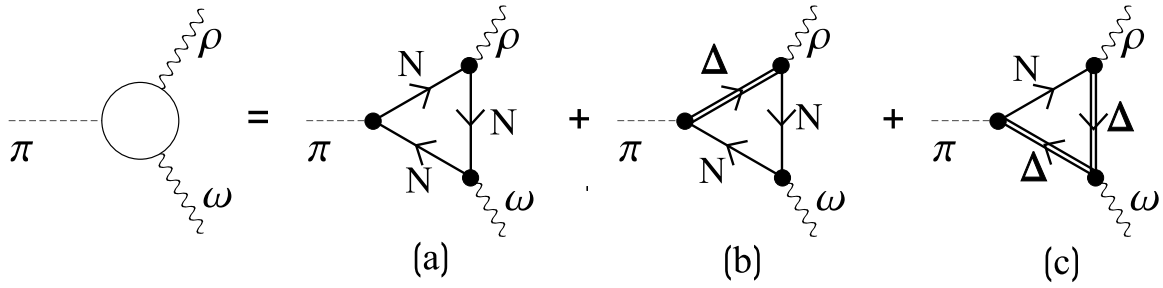


Figure 2.3: In-medium diagrams included in the present calculation (crossed diagrams not shown). Solid lines indicate the in-medium nucleon propagator, double lines the Δ propagator.

The in-medium nucleon propagator

Next, we introduce the in-medium nucleon propagator and the Rarita-Schwinger Δ propagator which we use in our calculations. We show also all the needed vertices, and the in-medium tensor structure of the in-medium $\pi\omega\rho$ coupling constant.

Solid lines in Fig. 2.3 denote the in-medium nucleon propagator, which can be conveniently decomposed into the *free* and *density* parts [2]:

$$iS(k) = iS_F(k) + iS_D(k) = i(\gamma^\mu k_\mu + m_N) \left[\frac{1}{k^2 - m_N^2 + i\varepsilon} + \frac{i\pi}{E_k} \delta(k_0 - E_k) \theta(k_F - |k|) \right], \quad (2.1)$$

where m_N denotes the nucleon mass, $E_k = \sqrt{m_N^2 + k^2}$, and k_F is the Fermi momentum. The density effects are produced when exactly one of the nucleon lines in each of the diagrams of Fig. 2.3 involves the nucleon density propagator, S_D . The diagrams with more than one S_D vanish for kinematic reasons, see Appendix D. On the other hand, diagrams with only S_F propagators do not contain Fermi-sea effects. Therefore, these vacuum diagrams are not considered in the present study. Finally, we have only one possibility of having exactly one nucleon density propagator in each of the diagrams of Fig. 2.3.

The Rarita-Schwinger propagator for the Δ baryon

In relativistic field theory the covariant description of spin 3/2 particles is based on the Rarita-Schwinger formalism [61], where the fundamental object is the spin-vector field Ψ^μ . The most general Lagrangian for the massive spin 3/2 field has the following form:

$$\mathcal{L} = \bar{\Psi}^\alpha \Lambda_{\alpha\beta} \Psi^\beta, \quad (2.2)$$

with

$$\begin{aligned}\Lambda_{\alpha\beta} = & -[(-i\partial_\mu\gamma^\mu + M_\Delta)g_{\alpha\beta} - iA(\gamma_\alpha\partial_\beta + \gamma_\beta\partial_\alpha) - \frac{i}{2}(3A^2 + 2A + 1)\gamma_\alpha\partial^\mu\gamma_\mu\gamma_\beta \\ & - M_\Delta(3A^2 + 3A + 1)\gamma_\alpha\gamma_\beta],\end{aligned}\quad (2.3)$$

where M_Δ is the mass of the spin $\frac{3}{2}$ particle ($\Delta(1232)$ is the most familiar example), and A is an arbitrary parameter ($A \neq -\frac{1}{2}$). This Lagrangian is invariant under the transformation

$$\begin{aligned}\Psi^\mu & \rightarrow \Psi^\mu + \alpha\gamma^\mu\gamma^\nu\Psi_\nu, \\ A & \rightarrow \frac{A - 2\alpha}{1 + 4\alpha},\end{aligned}\quad (2.4)$$

where $\alpha \neq -\frac{1}{4}$, but is otherwise arbitrary. The Lagrangian 2.2 leads to the equations of motion

$$\Lambda_{\alpha\beta}\Psi^\beta = 0. \quad (2.5)$$

The propagator for the massive spin $3/2$ particle satisfies the following equation in momentum space

$$\Lambda_{\alpha\beta}(k)G_\delta^\beta(k) = g_{\alpha\delta}, \quad (2.6)$$

where $g_{\alpha\delta}$ is the metric tensor, and

$$\begin{aligned}\Lambda_{\alpha\beta} = & -[(-\gamma \cdot k + M_\Delta)g_{\alpha\beta} - A(\gamma_\alpha k_\beta + \gamma_\beta k_\alpha) - \frac{1}{2}(3A^2 + 2A + 1)\gamma_\alpha\gamma \cdot k\gamma_\beta \\ & - M_\Delta(3A^2 + 3A + 1)\gamma_\alpha\gamma_\beta].\end{aligned}\quad (2.7)$$

Solving for G , one gets

$$\begin{aligned}G_{\alpha\beta}(k) = & \frac{\gamma \cdot k + M_\Delta}{k^2 - M_\Delta^2} \left[g_{\alpha\beta} - \frac{1}{3}\gamma_\alpha\gamma_\beta - \frac{1}{3M_\Delta}(\gamma_\alpha k_\beta - \gamma_\beta k_\alpha) - \frac{2}{3M_\Delta^2}k_\alpha k_\beta \right] - \\ & - \frac{1}{3M_\Delta^2} \frac{A+1}{2A+1} \left[\gamma_\alpha k_\beta + \frac{A}{2A+1}\gamma_\alpha k_\beta + \left[\frac{1}{2} \frac{A-1}{2A+1}\gamma \cdot k - \frac{AM_\Delta}{2A+1} \right] \gamma_\alpha\gamma_\beta \right].\end{aligned}\quad (2.8)$$

The physical properties of the free field are independent of the parameter A , so finally, with the parameter choice $A = -1$, we obtain the Rarita-Schwinger [62, 61] propagator for the spin Δ particle,

$$iS_\Delta^{\mu\nu}(k) = i\frac{\gamma^\mu k_\mu + M_\Delta}{k^2 - M_\Delta^2}(-g^{\mu\nu} + \frac{1}{3}\gamma^\mu\gamma^\nu + \frac{2k^\mu k^\nu}{3M_\Delta^2} + \frac{\gamma^\mu k^\nu - \gamma^\nu k^\mu}{3M_\Delta}). \quad (2.9)$$

This propagator, often found in the literature, is denoted by the double lines in the diagrams of Fig. 2.3.

We incorporate phenomenologically the effects of the non-zero width of the Δ by the replacement $M_\Delta \rightarrow M_\Delta - i\Gamma_\Delta/2$. This treatment of the finite width of the Δ is consistent with the Ward-Takahashi identities for the $\pi\rho\omega$ vertex. This would not be true if Γ_Δ were introduced in the denominator of Eq. (2.9) only.

Feynman rules

In the vacuum, the $\pi\omega\rho$ vertex has the form

$$-iV_{\pi\omega\rho} = i\frac{g_{\pi\omega\rho}}{F_\pi}\epsilon^{\mu\nu pQ}, \quad (2.10)$$

where $g_{\pi\omega\rho}$ is a $\pi\omega\rho$ coupling constant, and $F_\pi = 93$ MeV is the pion coupling constant. We have also used a convenient short-hand notation

$$\epsilon^{\mu\nu pQ} = \epsilon^{\mu\nu\alpha\beta}p_\alpha Q_\beta. \quad (2.11)$$

We choose Q as the incoming momentum of the π , p as the outgoing momentum of the ρ , and $q \equiv Q - p$ as the outgoing momentum of the ω , see Fig. 2.4.

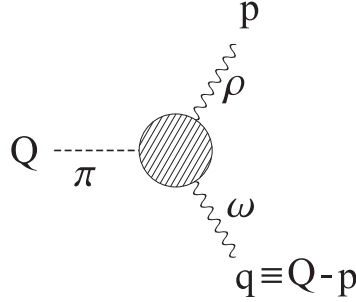


Figure 2.4: The assignment of momenta in the $\pi\omega\rho$ vertex.

In the general case ω and ρ are virtual particles. The value of $g_{\pi\omega\rho}$ can be obtained with the help of the Vector Meson Dominance Model from the anomalous $\pi\gamma\gamma$ decay. According to this model the electromagnetic interactions of hadrons are described by intermediate coupling to vector mesons, see Fig. 2.1. The vector meson is subsequently converted into a virtual photon and finally the photon decays into the lepton pair, e^+e^- .

The vacuum $\pi^0 \rightarrow \gamma\gamma$ decay

One can calculate the $g_{\pi\gamma\gamma}$ coupling constant from the width of the $\pi^0 \rightarrow \gamma\gamma$ decay in the vacuum. The transition amplitude of $\pi^0 \rightarrow \gamma\gamma$ decay has the form

$$\mathcal{M} = g_{\pi\gamma\gamma}\epsilon^{\mu\nu pQ}\epsilon^{\nu'}\epsilon^\nu, \quad (2.12)$$

where the value of $g_{\pi\gamma\gamma} = \frac{e^2}{4\pi^2 F_\pi}$ is model independent and results from Adler-Bell-Jackiw anomaly. The formula for the decay width is

$$d\Gamma_{\pi\gamma\gamma} = \frac{1}{32\pi^2} \sum_{\epsilon\epsilon'} |\mathcal{M}|^2 \frac{|\mathbf{p}|}{m_\pi^2} d\Omega \times \frac{1}{2}, \quad (2.13)$$

where, $|\mathbf{p}| = m_\pi/2$ is momentum of one of the photons in the rest frame of the pion, and the factor of $1/2$ comes from the symmetrization over the indistinguishable bosons in the final state. Since the sum over all photon polarizations with momentum p gives

$$\sum_a \epsilon_{(a)}^\mu \epsilon_{(a)}^{\nu*} = g^{\mu\nu} - \frac{p^\mu p^\nu}{p^2}, \quad (2.14)$$

and from kinematics $q^2 = m_\pi^2$, $(Q - p)^2 = 0$, we find

$$\sum_{\epsilon\epsilon'} |\mathcal{M}|^2 = g_{\pi\gamma\gamma}^2 \frac{m_\pi^4}{2}. \quad (2.15)$$

Consequently, the width has a form

$$\Gamma_{\pi\gamma\gamma} = g_{\pi\gamma\gamma}^2 \frac{m_\pi^3}{64\pi}, \quad (2.16)$$

where $g_{\pi\gamma\gamma}$, applying the VDM (see Fig. 2.1), can be expressed in terms of the $g_{\pi\omega\rho}$ coupling constant as (see Fig. 2.5)

$$g_{\pi\gamma\gamma}^2 = g_{\pi\omega\rho}^2 \frac{e^2}{F_\pi^2 g_\rho^2 g_\omega^2}. \quad (2.17)$$

Finally, the width is

$$\Gamma_{\pi\gamma\gamma} = g_{\pi\omega\rho}^2 \frac{e^2}{F_\pi^2 g_\rho^2 g_\omega^2} \frac{m_\pi^3}{64\pi}. \quad (2.18)$$

Using the physical parameters which we collect in Eq. 2.23, as well as $\Gamma_{\pi\gamma\gamma} = 7.6\text{eV}$, $m_\pi = 135\text{MeV}$, $e^2 = 4\pi\alpha$ (where $\alpha = \frac{1}{137}$), we obtain the value of coupling constant $g_{\pi\omega\rho}$ by comparison of the $\pi^0 \rightarrow \gamma\gamma$ and $\pi^0 \rightarrow \rho\omega$ diagrams, Fig. 2.5. It gives $g_{\pi\omega\rho} = -\frac{g_\rho g_\omega}{e^2} g_{\pi\gamma\gamma} = -1.36$ (in our convention the sign of the coupling is negative).

Meson-NN and meson-N Δ vertices

The meson-NN vertices needed for our calculation have the standard form

$$\begin{aligned} -iV_{\omega^\mu NN} &= ig_\omega \gamma^\mu, \\ -iV_{\rho_b^\mu NN} &= i\frac{g_\rho}{2} (\gamma^\mu - \frac{i\kappa_\rho}{2m_N} \sigma^{\mu\nu} p_\nu) \tau^b, \\ -iV_{\pi^a NN} &= \frac{g_A}{2F_\pi} \bar{Q} \gamma^5 \tau^a, \end{aligned} \quad (2.19)$$

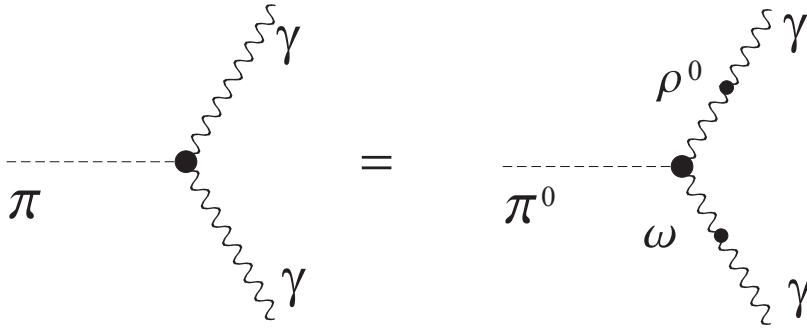


Figure 2.5: Comparison of two diagrams, $\pi \rightarrow \gamma\gamma$ and $\pi^0 \rightarrow \omega\rho$. Black dot indicates $g_{\pi\gamma\gamma} = \frac{e^2}{4\pi^2 F_\pi}$ and $\frac{g_{\pi\omega\rho}}{F_\pi^2} = \frac{g_\omega g_\rho}{F_\pi e^2}$ coupling constants. The smaller black dot is equal to $\frac{em_\omega^2}{g_\omega}$ or $\frac{em_\rho^2}{g_\rho}$, according to VDM.

where p is the outgoing momentum of the virtual ρ , Q is the incoming four-momentum of the π , and a, b are the isospin indices of the π , and ρ respectively, g_ω and g_ρ are coupling constants for the ω and ρ meson, κ_ρ is tensor coupling of the ρ meson, and g_A denotes the axial coupling constant.

For the interactions involving the Δ we use the same choice as in Ref. [60]:

$$\begin{aligned} -iV_{N\Delta^\alpha\pi^a} &= g_{N\Delta\pi}Q^\alpha T^a, \\ -iV_{N\Delta^\alpha\rho_b^\mu} &= ig_{N\Delta\rho}(p^\mu\gamma^5 g^{\alpha\mu} - \gamma^\mu\gamma^5 p^\alpha)T^b, \\ -iV_{\Delta^\alpha\Delta^\beta\omega^\mu} &= -ig_\omega(\gamma^\alpha\gamma^\mu\gamma^\beta - \gamma^\beta g^{\alpha\mu} - \gamma^\alpha g^{\beta\mu} + \gamma^\mu g^{\alpha\beta}), \end{aligned} \quad (2.20)$$

where T^a are the isospin $\frac{1}{2} \rightarrow \frac{3}{2}$ transition matrices [63]. They are defined through the Clebsch-Gordan coefficients as follows: $\langle \frac{3}{2}, I_3 | T^\mu | \frac{1}{2}, i_3 \rangle = \langle \frac{1}{2} 1 i_3 \mu | \frac{1}{2} \frac{3}{2} I_3 \rangle$, with i_3 and I_3 denoting the isospin of the nucleon and Δ , respectively. In the Cartesian basis the explicit form reads

$$T^1 = \begin{pmatrix} -\frac{1}{\sqrt{2}} & 0 \\ 0 & -\frac{1}{\sqrt{6}} \\ \frac{1}{\sqrt{6}} & 0 \\ 0 & \frac{1}{\sqrt{2}} \end{pmatrix}, \quad T^2 = i \begin{pmatrix} \frac{1}{\sqrt{2}} & 0 \\ 0 & \frac{1}{\sqrt{6}} \\ \frac{1}{\sqrt{6}} & 0 \\ 0 & \frac{1}{\sqrt{2}} \end{pmatrix}, \quad T^3 = \begin{pmatrix} 0 & 0 \\ \sqrt{\frac{2}{3}} & 0 \\ 0 & \sqrt{\frac{2}{3}} \\ 0 & 0 \end{pmatrix}, \quad (2.21)$$

where the columns are labeled by $i_3 = \frac{1}{2}, -\frac{1}{2}$, left to right, and the rows by $I_3 = \frac{3}{2}, \frac{1}{2}, -\frac{1}{2}, -\frac{3}{2}$, top to bottom. The following useful relation holds:

$$T^{a\dagger}T^b = \frac{2}{3}\delta^{ab} - \frac{1}{3}\varepsilon^{abc}\tau_c. \quad (2.22)$$

The values of the $N\Delta$ coupling constants follow from the non-relativistic reduction of the vertices and comparison to the non-relativistic values [63]. The $\Delta\Delta\omega$ coupling

incorporates the principle of universal coupling. It is obtained by replacing $k^\mu \rightarrow k^\mu + \omega^\mu$ in the Rarita-Schwinger Lagrangian, Eq. 2.7.

Note that the $\rho\Delta\Delta$ vertex does not appear in this study. Presence of $\rho\Delta\Delta$ coupling in diagram 2.3 implies that the $\omega N\Delta$ coupling should also appear. This is impossible from the Wigner-Eckart theorem, since ω is an isoscalar particle.

The choice of physical parameters is taken from other works [64] and is as follows:

$$\begin{aligned} g_\omega &= 10.4, & g_\rho &= 5.2, & g_A &= 1.26, \\ g_{N\Delta\pi} &= \frac{2.12}{m_\pi}, & g_{N\Delta\rho} &= \frac{2.12\sqrt{2}}{m_\pi}. \end{aligned} \quad (2.23)$$

In the results presented below we have chosen the tensor coupling of the ρ meson, $\kappa_\rho = 3.7$. The principle of universal coupling and the field current identity imply that the isovector part of the anomalous magnetic moment of the nucleon, κ_V , is equal to the tensor coupling of the ρ meson, *i.e.* $\kappa_\rho = \kappa_V = 3.7$, [65], κ_V is the isovector anomalous magnetic moment of the nucleon. However, the empirical value of κ_ρ/κ_V extracted by Hohler and Pietarinen [66] using a dispersion relation analysis of the πN scattering data is 1.78. Qualitatively, in our analysis similar conclusions follow when $\kappa_\rho = 6$ is used.

We have to admit here that the relativistic form of couplings to the Δ , as well as the values of the coupling constants, are the subjects of an on-going discussion and research [62, 67, 68, 69]. We are interested in estimating the size of the medium effect on the $\pi\omega\rho$ vertex and we do not search for precise and accurate predictions of tensor couplings.

In order to simplify the approach we do not include any form factors in the vertices. In general, a vertex may depend on outgoing meson momentum squared, p^2 , q^2 , Fig. 2.4, and the Lorentz scalars, $\mathbf{p} \cdot \mathbf{k}$ and $\mathbf{q} \cdot \mathbf{k}$, which enter the so-called sidewise form factors. Those form factors are not included in our calculations, because they lead to fundamental problems with gauge symmetry conservation. In particular the current conservation identities, Eq. 2.30, are violated.

Tensor structure of the $\pi\omega\rho$ vertex in nuclear medium

In our calculation we evaluate the diagrams of Fig. 2.3 and obtain the in-medium $\pi\omega\rho$ vertex function

$$A^{\mu\nu} = \int \frac{d^4k}{(2\pi)^4} \frac{m_N}{E_k} \theta(k_f - |\mathbf{k}|) A'^{\mu\nu} \delta(k_0 - E_k), \quad (2.24)$$

where

$$\begin{aligned}
A'^{\mu\nu} &= A_1 \varepsilon^{\mu\nu p Q} + A_2 \varepsilon^{\mu\nu k Q} + A_3 \varepsilon^{\mu\nu p k} + (A_4 p^\nu + A_5 Q^\nu + A_6 k^\nu) \varepsilon^{\mu k p Q} \\
&+ (A_7 p^\mu + A_8 Q^\mu + A_9 k^\mu) \varepsilon^{\nu k p Q}.
\end{aligned} \tag{2.25}$$

Thus in medium we have 9 possible tensor structures, while in the vacuum there was only one, $\varepsilon^{\mu\nu p Q}$, Eq 2.10. All coefficients A_i are scalar functions of the four-vectors Q , p and k , with $k^0 = E_k$. The occupation function is made explicitly Lorentz-invariant when we write $|\mathbf{k}| = \sqrt{(k \cdot u)^2 - m_N^2}$, where u is the four-velocity of the medium.

The term with k^μ , upon the evaluation of the integral can be in general proportional to the three Lorentz vectors present in the problem, p^μ , Q^μ , and u^μ , where u^μ is the four-velocity of the medium.

$$\int \frac{d^4 k}{(2\pi)^4} \frac{m_N}{E_k} A k^\mu \theta(k_f - |\mathbf{k}|) \delta(k_0 - E_k) = A_p p^\mu + A_q Q^\mu + A_u u^\mu, \tag{2.26}$$

where A_p , A_q and A_u are scalar functions of p^2 , Q^2 , $p \cdot Q$, $p \cdot u$, $q \cdot u$, and k_F . Contracting Eq. 2.26 with Q_μ , p_μ and u_μ we obtain a linear algebraic equations for A_p , A_q and A_u which may be solved. To make this problem simpler we use the leading density approximation. This is equivalent to putting the three-vector \mathbf{k} to zero in the functions $A_2 - A_9$ in Eq. 2.24 in the rest frame of the medium. Then we replace the loop momentum integration by

$$\int \frac{d^4 k}{(2\pi)^4} \theta(k_f - |\mathbf{k}|) \delta(k_0 - E_k) \rightarrow \frac{1}{8\pi} \rho_B, \tag{2.27}$$

where ρ_B is the baryon density. Now, with $\mathbf{k} = 0$, $k^0 = m_N$, the contraction of Eq. 2.26 with q_μ , p_μ , and u_μ gives the set of equations

$$\begin{aligned}
\frac{1}{8\pi} \rho_B m_N p^0 A(\mathbf{k} = 0) &= A_p p^2 + A_q Q \cdot p + A_u p^0, \\
\frac{1}{8\pi} \rho_B m_N Q^0 A(\mathbf{k} = 0) &= A_p p \cdot q + A_q Q^2 + A_u q^0, \\
\frac{1}{8\pi} \rho_B m_N u^0 A(\mathbf{k} = 0) &= A_p p \cdot u + A_q Q \cdot u + A_u u^0,
\end{aligned} \tag{2.28}$$

where $u^0 = 1$ in the rest frame of the medium.

Since in the general case the vectors p , Q , and u are linearly-independent, the solution of Eqs. 2.28 is $A_p = A_q = 0$, $A_u = \frac{1}{8\pi} \rho_B m_N A(\mathbf{k} = 0)$. Thus, only the term proportional to u^μ in Eq. (2.26) is present in the leading-density approximation. Summarizing, above calculations, similarly as in [60], are equivalent to replacing k^μ by $m_N u^\mu$, what is valid for every occurrence of k in Eq. 2.24. For the terms in this equation involving second powers of k , the same prescription holds, as may be simply verified by an analysis analogous to the one presented above.

Finally, we obtain the most general tensor structure of the form

$$\begin{aligned}
A^{\mu\nu} &= A_1 \varepsilon^{\mu\nu p Q} + A_2 \varepsilon^{\mu\nu u Q} + A_3 \varepsilon^{\mu\nu p u} + (A_4 p^\nu + A_5 Q^\nu + A_6 u^\nu) \varepsilon^{\mu p Q} \\
&+ (A_7 p^\mu + A_8 Q^\mu + A_9 u^\mu) \varepsilon^{\nu p Q}.
\end{aligned} \tag{2.29}$$

This structure, restricted by the Lorentz invariance and parity, is more general than in the vacuum case Eq. 2.10 due to the availability of the four-velocity of the medium, u . The result of any dynamical calculation will assume the form Eq 2.29. The vertex $A^{\mu\nu}$ satisfies the current conservation identities:

$$Q_\mu A^{\mu\nu} = 0, \quad \text{and} \quad p_\nu A^{\mu\nu} = 0, \tag{2.30}$$

which serves as a useful check of the algebra.

For the numerical analysis we have developed a program written in 'Mathematica'. In order to calculate traces from all diagrams of Fig. 2.3, we have to apply the Feynmann rules, use Lorentz index contractions, and compute traces of the Dirac matrices (up to as many as 14). It is rather complicated from the technical point of view, thus we use FeynCalc [70]. This is a package for algebraic calculation in elementary particle physics, which is very useful for many problems involving baryon loops with density-dependent nucleon propagators. All our calculations are covariant.

2.2 Decays of particles at rest with respect to the medium

We begin the presentation of our results for the case where the decaying particle is at rest with respect to the nuclear matter, $\mathbf{q} = 0$.

The in-medium $\pi^0 \rightarrow \gamma\gamma$ decay

First, numerical results are discussed for the process $\pi^0 \rightarrow \gamma\gamma$, because of its fundamental nature. This is the decay into two real photons, where the pion is at rest with respect to the medium. In this case the four-vectors Q and u are parallel, and out of the 9 structures in Eq. 2.29 only A_1 and A_3 survive:

$$A^{\mu\nu} = A_1 \varepsilon^{\mu\nu p Q} + A_3 \varepsilon^{\mu\nu p u}. \tag{2.31}$$

Thus in the rest frame of the medium, where $Q = (m_\pi, 0, 0, 0)$, it is found that

$$\begin{aligned}
A^{\mu\nu} &= A_1 Q_0 \varepsilon^{\mu\nu p 0} + A_3 u_0 \varepsilon^{\mu\nu p 0} \\
&= (m_\pi A_1 + A_3) \varepsilon^{\mu\nu p 0} = (A_1 + A_3/m_\pi) \varepsilon^{\mu\nu p Q}.
\end{aligned} \tag{2.32}$$

The following notation is introduced, which combines the vacuum and medium pieces:

$$A^{\mu\nu} = \frac{i}{F_\pi} \frac{e^2}{g_\rho g_\omega} (g_{\pi\rho\omega} + \rho_B B) \epsilon^{\nu\mu p Q}. \quad (2.33)$$

All the medium effects are collected in the constant B . The results of the medium-modified vertex at the nuclear-saturation density ($\rho_B = \rho_0 = 0.17 \text{ fm}^{-3}$) are presented relative to the vacuum value $g_{\text{vac}} = g_{\pi\rho\omega}$. In this analysis the medium effects are linear in the baryon density. We define

$$g_{\text{eff}} = g_{\pi\rho\omega} + \rho_B B, \quad (2.34)$$

with B denoting the medium contribution. Separate contributions to B coming from diagrams (a), (b) and (c) of Fig. 2.3 for the process $\pi^0 \rightarrow \gamma\gamma$ are as follows:

$$\begin{aligned} B_{(a)} &= \frac{g_A g_\rho g_\omega (\kappa_\rho + 1)}{m_N (4m_N^2 - m_\pi^2)}, \\ B_{(b)} &= \frac{g_{N\Delta\pi} g_{N\Delta\rho} g_\omega F_\pi m_\pi}{9M_\Delta^2 m_N [(m_N^2 - M_\Delta^2)^2 - m_\pi^2 m_N^2]} (m_N^4 + M_\Delta m_N^3 - 2M_\Delta^2 m_N^2 - \\ &\quad - m_\pi^2 m_N^2 - M_\Delta^3 m_N + M_\Delta^4), \\ B_{(c)} &= \frac{g_{N\Delta\pi} g_{N\Delta\rho} g_\omega F_\pi m_\pi}{27M_\Delta^4 [(m_N^2 - M_\Delta^2)^2 - m_\pi^2 m_N^2]} (-4m_N^5 - 6M_\Delta m_N^4 + 8M_\Delta^2 m_N^3 + \\ &\quad + 5M_\Delta^3 m_N^2 + (4m_N + 3M_\Delta) m_\pi^2 m_N^2 - 16M_\Delta^4 m_N - 11M_\Delta^5), \end{aligned} \quad (2.35)$$

where M_Δ is understood to carry the width $i\Gamma_\Delta$. With parameters (2.23) we find numerically for the formal case $\Gamma_\Delta = 0$,

$$B_{(a)} = 97 \text{ GeV}^{-3}, B_{(b)} = -3.1 \text{ GeV}^{-3}, B_{(c)} = -102 \text{ GeV}^{-3}. \quad (2.36)$$

For the physical vacuum value of the Δ width, $\Gamma_\Delta = 0.12 \text{ GeV}$, we find

$$B_{(a)} = 97 \text{ GeV}^{-3}, B_{(b)} = -(2.6 + 1.5i) \text{ GeV}^{-3}, B_{(c)} = -(87 + 42i) \text{ GeV}^{-3}, \quad (2.37)$$

and

$$|g_{\text{eff}}/g_{\text{vac}}|^2 = |0.99 + 0.04i|^2 = 0.99, \quad (2.38)$$

whereas for nucleons only (diagram (a)) we would have

$$|g_{\text{eff}}^{(a)}/g_{\text{vac}}|^2 = 0.91^2 = 0.82. \quad (2.39)$$

The imaginary values come from the $i\Gamma_\Delta$ term. From Eq. 2.38 and 2.39 we see that the effects of the Δ act in the opposite direction than the nucleons, resulting in an almost complete cancellation between diagrams (a) and (a+b+c) of Fig. 2.3.

The $\pi^0 \rightarrow \gamma\gamma^*$ decay

The Dalitz decay of π^0 into a photon and a lepton pair proceeds through the decay into a real and a virtual photon, and subsequently the decay of the virtual photon into the lepton pair, $\pi^0 \rightarrow \gamma\gamma^* \rightarrow \gamma e^+ e^-$, see Fig. 2.6. The contributions to the constant

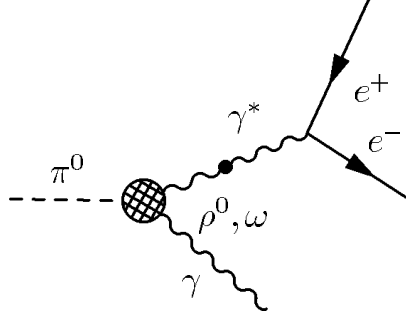


Figure 2.6: The $\pi^0 \rightarrow \gamma\gamma^* \rightarrow \gamma e^+ e^-$ decay. Wavy lines indicates the ρ , ω or γ , dashed lines the pions, the hatched blob denotes the medium-modified vertex, the black dot is equal to $\frac{em_\omega^2}{g_\omega}$ or $\frac{em_\rho^2}{g_\rho}$ according to VDM.

B from all diagrams of Fig. 2.3 for the processes $\pi^0 \rightarrow \gamma_{(\omega)}\gamma^*$ and $\pi^0 \rightarrow \gamma_{(\rho)}\gamma^*$, are listed in Appendix A.

The virtual photon can be either isovector (ρ -type) or isoscalar (ω -type); thus $\gamma_{(\omega)}$ denotes a photon which couples as an isoscalar and $\gamma_{(\rho)}$ a photon which couples as an isovector. We denote the virtuality of γ^* as M_{γ^*} and investigate the dependence of g_{eff} on M_{γ^*} . The results both for the process $\pi^0 \rightarrow \gamma_{(\omega)}\gamma^*$ and $\pi^0 \rightarrow \gamma_{(\rho)}\gamma^*$, are displayed in Fig. 2.7. All calculations are done at the saturation density $\rho_B = \rho_0$ and with the vacuum value of the Δ width, $\Gamma_\Delta = 120$ MeV. In the two upper plots of Fig. 2.7 the solid lines show the real and imaginary parts of the full calculations, which means that we take into account all diagrams of Fig. 2.3 (with nucleons and delta isobars), whereas the dashed lines show the calculations with nucleons only which, of course, are real. The Δ resonance has imaginary contribution for $Im\Gamma_\Delta$, whereas for nucleons the result is always real.

In the two bottom plots of the same figure, the solid and dashed curves indicate full calculations with deltas and nucleons, respectively. The results displayed in Fig. 2.7, indicate that the change of M_{γ^*} in the allowable kinematic range from 0 to m_π has very little effect on the ratio of $g_{\text{eff}}/g_{\text{vac}}$ and $|g_{\text{eff}}/g_{\text{vac}}|^2$. A somewhat different behavior for the isoscalar and isovector photons at M_{γ^*} approaching m_π is noticed. We observe that curves corresponding to the calculations with the Δ isobar shift the curve slightly up for $\pi^0 \rightarrow \gamma_{(\omega)}\gamma$ decay, whereas for isovector photons the curves are pulled down,

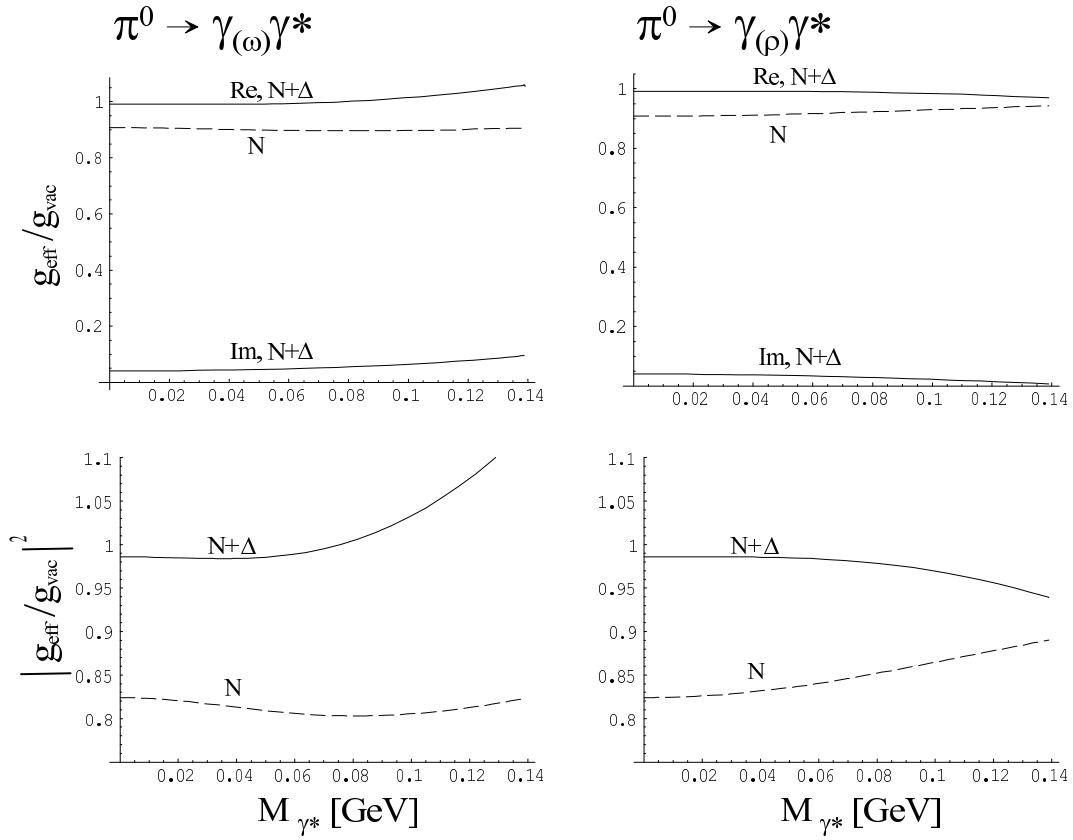


Figure 2.7: The quantity $g_{\text{eff}}/g_{\text{vac}}$ and $|g_{\text{eff}}/g_{\text{vac}}|^2$ for the processes $\pi^0 \rightarrow \gamma_{(\omega)}\gamma^*$ and $\pi^0 \rightarrow \gamma_{(\rho)}\gamma^*$, plotted as a function of the virtual mass of γ^* , M_{γ^*} . The solid lines show the results of the full calculation with all diagrams (a+b+c) of Fig. 2.3 included, while the dashed lines correspond to the calculations with nucleon diagram (a) only. The upper plots include results of real and imaginary parts. All plots are done for the case $\rho_B = \rho_0$ and $\Gamma_\Delta = 120$ MeV.

when approaching m_π value. On the other hand for both of those decays the shape of curves without the Δ isobar is similar. By comparing the curves corresponding to the calculation with the Δ (diagrams (a+b+c) of Fig. 2.3) and with nucleons only (diagram (a)), it is visible that they act in opposite directions in diagrams (a) and (a+b+c), and it holds for the whole kinematically-available range.

In Fig. 2.8, we show the result of the calculation with fixed Γ_Δ , but with m_N and M_Δ scaled down to 70% of their vacuum value. Such a reduced baryon mass is typical at the nuclear saturation density and is predicted by the Brown-Rho scaling hypothesis, see Chapter 1. The reduced mass of Δ is expected to behave similarly to the nucleon case. We notice that g_{eff} is practically unchanged, and Fig. 2.7 and Fig. 2.8 show a similar behavior.

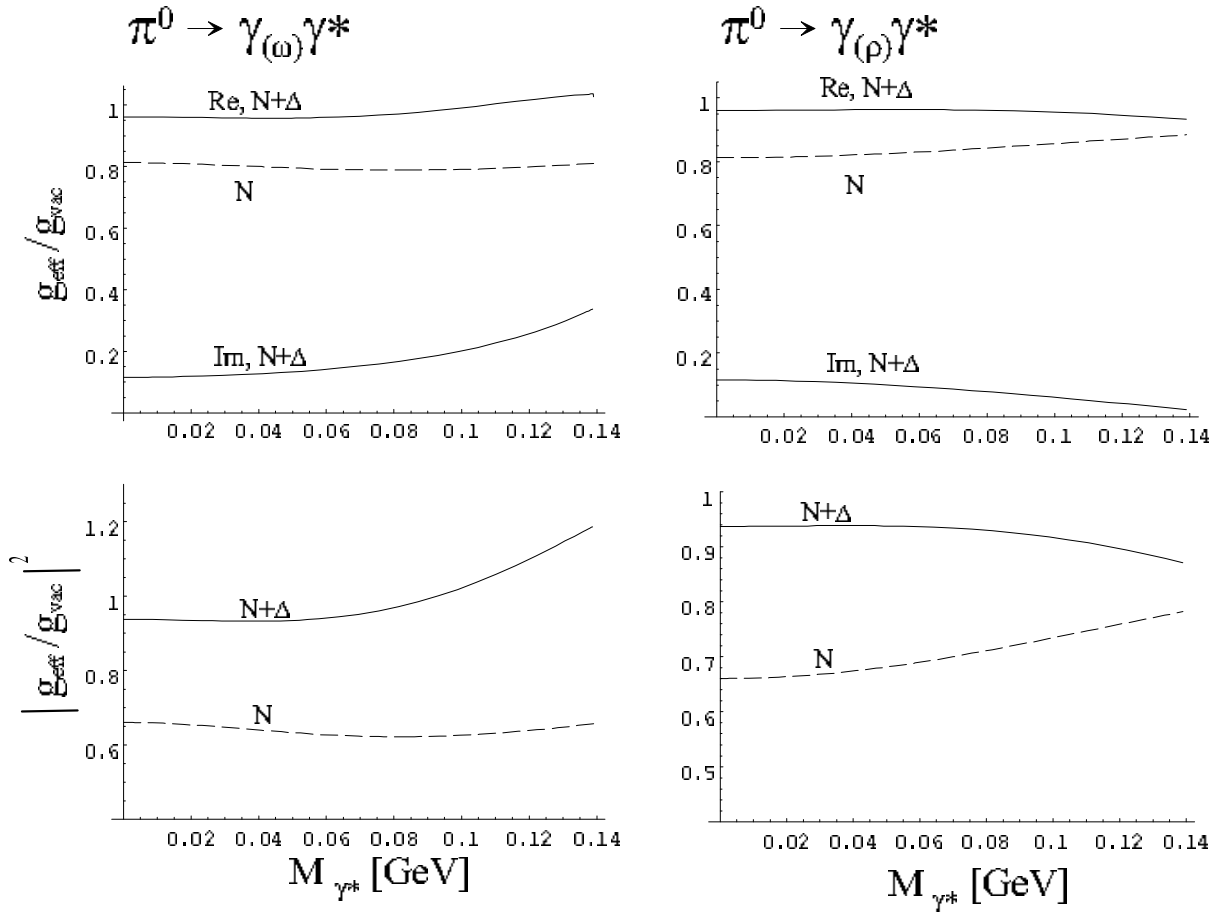


Figure 2.8: Same as Fig. 2.7, but for the values of m_N and M_Δ reduced to 70% of their vacuum values.

The $\omega \rightarrow \pi^0 \gamma^*$ and $\rho^a \rightarrow \pi^a \gamma^*$ decays

Next, we consider the processes $\omega \rightarrow \pi^0 \gamma^*$ and $\rho^a \rightarrow \pi^a \gamma^*$, where ω and ρ are on the mass shell. In these cases the following vacuum values of the coupling constants are used, $g_{\omega \rightarrow \rho \pi} = -1.13$ and $g_{\rho \rightarrow \omega \pi} = -0.76$. They are calculated from the experimental partial decay widths

$$\Gamma_{\omega \pi \gamma} = 717 \text{keV} \quad \text{and} \quad \Gamma_{\rho \pi \gamma} = 79 \text{keV}. \quad (2.40)$$

Let us concentrate on the first decay. The decay width for the process $\omega \rightarrow \pi^0 \gamma$ has the form

$$\Gamma_{\omega \pi \gamma} = \sum_{\epsilon_{(1)} \epsilon_{(2)}} \frac{4\pi \mathcal{M}^2 p_\rho^2}{32\pi^2 3m_\omega^2}, \quad (2.41)$$

where

$$\mathcal{M} = g_{\omega \pi \gamma} \epsilon^{\mu\nu\rho\sigma} \epsilon_{(1)}^\mu \epsilon_{(2)}^\nu = \frac{e g_{\omega \pi \rho}}{F_\pi g_\rho} \epsilon^{\mu\nu\rho\sigma} \epsilon_{(1)}^\mu \epsilon_{(2)}^\nu, \quad (2.42)$$

and with the momentum of the ρ

$$p_\rho^2 = \frac{(m_\omega^2 + m_\rho^2 - m_\pi^2)^2}{4m_\omega^2} - m_\rho^2. \quad (2.43)$$

Putting together all the needed parameters from Eq. 2.23 we obtain the physical value of the coupling constant, $g_{\omega\pi\rho} = -1.13$. In a similar way we obtain $g_{\rho\pi\omega}$. Note that these coupling constants differ from each other, as well as from $g_{\pi\omega\rho} = -\frac{g_\rho g_\omega}{e^2} g_{\pi\gamma\gamma} = -1.36$ used earlier for the π^0 decay. These differences may be attributed to form-factor effects: the virtuality of the vector mesons is changed from 0 in the $\pi^0 \rightarrow \gamma\gamma$ decay to the on-shell value in the vector meson decay. For the case $\mathbf{q} = \mathbf{0}$ the contributions to B from Eq. 2.33 corresponding to the diagram (a,b,c) from Fig. 2.3, can be written as

$$A_{(i)}^{\mu\nu} = \frac{i}{F_\pi} \frac{e^2}{g_\rho g_\omega} \left(g_{\pi\rho\omega} + \rho_B \frac{N_{(i)}}{D_{(i)}} \right) \epsilon^{\nu\mu p Q}, \quad (2.44)$$

The formulas for $N_{(i)}$ and $D_{(i)}$ are quite cumbersome, which reflects the presence of many terms in the Rarita-Schwinger propagator. We give them in Appendix B.

There is an interesting phenomenon in the decays of vector mesons, related to the analyticity of the amplitudes of Fig. 2.3(b) and (c) in the virtuality of γ^* . From the denominators of diagrams (b) and (c) of Fig. 2.3, see Appendix B for the case $\Gamma_\Delta = 0$, we can see that the amplitudes from Eq. 8.3 have a pole at the value of M_{γ^*} equal to

$$M_0 = \sqrt{\frac{m_v m_N^2 + m_\pi^2 m_N + m_v^2 m_N - M_\Delta^2 m_v + m_\pi^2 m_v}{m_N}} \approx 0.34 \text{ GeV}, \quad (2.45)$$

where $m_v = m_\rho$ or m_ω . The above analytic structure is manifest in the numerical calculation presented below. For $\Gamma_\Delta \neq 0$ the pole at 2.45 moves away from the real axis. Thus, analyticity is important and immediately leads to large changes of the vertex function near the poles. This formal feature of the presence of the pole can be clearly seen in the plots of Fig. 2.9 for the case of $\Gamma_\Delta = 0$ (dashed lines). For the values of $\Gamma_\Delta = 60$ MeV (dotted line), $\Gamma_\Delta = 120$ MeV, the physical value (solid line) and $\Gamma_\Delta = 240$ MeV (dot-dashed line) the pole is washed-out, but its traces are still visible, with the curves reaching maxima around $M_0 = 0.4$ GeV. The upper value of the virtual mass is $M_{\gamma^*} = m_\omega - m_\pi = 0.64$ GeV. The differences between all the curves for various values of Γ_Δ in the range of M_{γ^*} between 0.2 and 0.6 GeV shows that the results are sensitive to the assumed value for Γ_Δ . We can observe that at low values of M_{γ^*} the effective coupling constant remains practically unchanged. However, at higher values of M_{γ^*} , above 0.2 GeV, the value of g_{eff} is significantly

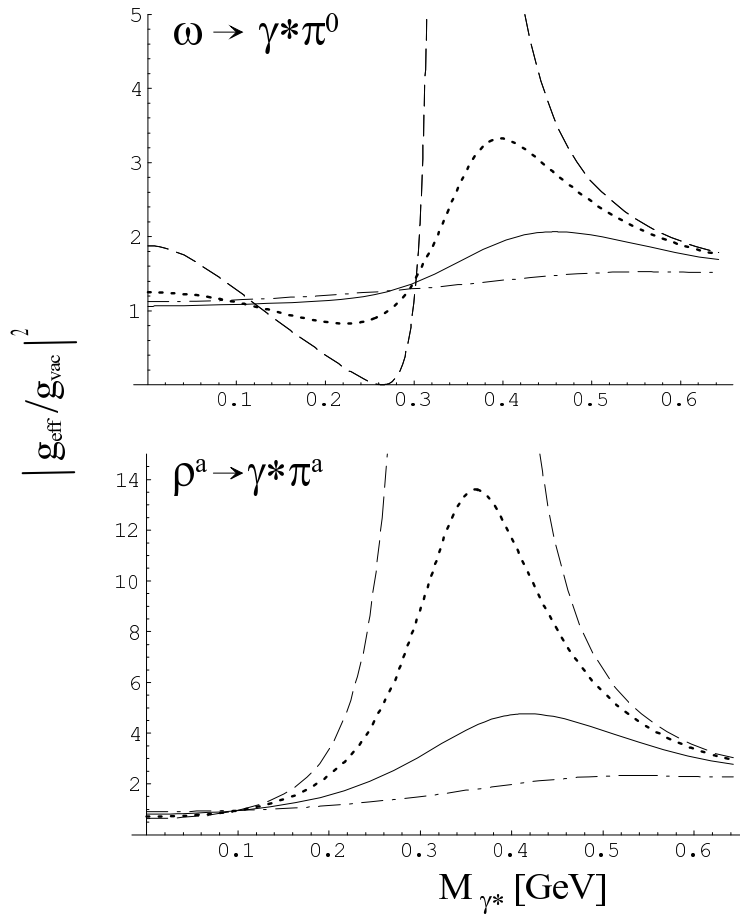


Figure 2.9: Top: $|g_{\text{eff}}/g_{\text{vac}}|^2$ for the decay $\omega \rightarrow \gamma^* \pi^0$ at the nuclear saturation density, plotted as a function of the virtuality of the photon, M_{γ^*} . The dashed, dotted, solid and dot-dash lines correspond to the cases, $\Gamma_\Delta = 0$, $\Gamma_\Delta = 60$ MeV, $\Gamma_\Delta = 120$ MeV, $\Gamma_\Delta = 240$ MeV, respectively. Bottom: the same for the decay $\rho^a \rightarrow \gamma^* \pi^a$.

larger than in the vacuum. For the square of the coupling we find an enhancement by a factor of ~ 2 for the ω decay, and by a factor as large as ~ 5 for the ρ decay. All these numbers are quoted at the saturation density $\rho_B = \rho_0$.

In Fig. 2.10 we display the results for different values of the baryon density, ρ_B . For simplicity we denote the saturation density as

$$y = \frac{\rho_B}{\rho_0}. \quad (2.46)$$

We have done the calculations for both these decays for $\kappa_\rho = 3.7$ (dashed lines) and $\kappa_\rho = 6$ (solid lines). We can see that the effective coupling constant is more enhanced with growing density ratio y .

Our method can be trusted numerically only at sufficiently low values of the baryon density, such that the leading-density approximation holds. For the masses or condensates mentioned in Chapter 1 the nuclear saturation density is low enough to use

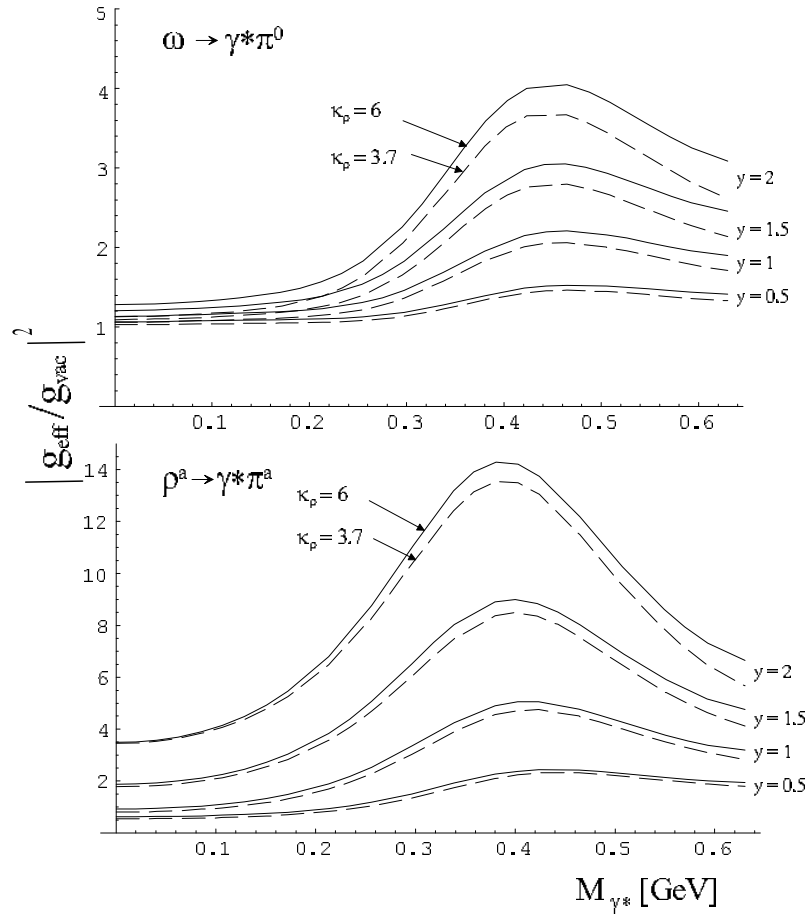


Figure 2.10: Top: $|g_{\text{eff}}/g_{\text{vac}}|^2$ for the decay $\omega \rightarrow \gamma^* \pi^0$ at the nuclear saturation density, plotted as a function of the virtuality of the photon, M_{γ^*} . The solid lines correspond to the case with $\kappa_\rho = 6$, dashed lines for $\kappa_\rho = 3.7$, $y = \frac{\rho B}{\rho_0}$. Bottom: the same for the $\rho^a \rightarrow \pi^a \gamma^*$ decay.

the low density approximation. On the other hand, we can see from Fig. 2.10 that the effects are large already at the saturation density.

Therefore, numerical results at high densities obtained from our consideration are strongly indicative of possible large effects in the Dalitz decays of vector mesons in medium. In the $\omega \rightarrow \pi^0 \gamma^*$ and $\rho^a \rightarrow \pi^a \gamma^*$ decays, we compare the calculation with and without the Δ isobar, see Fig. 2.11.

In the figure we plot the ratio $g_{\text{eff}}/g_{\text{vac}}$ and $|g_{\text{eff}}/g_{\text{vac}}|^2$ as a function of the virtual photon mass, M_{γ^*} at the saturation density $y = 1$ and for $\Gamma_\Delta = 120$ MeV, same as we have done in the previous case of the $\pi \rightarrow \gamma \gamma^*$ decay. In two upper plots we show the imaginary and real (solid line) part of the calculations including nucleons and delta isobars, and the calculation with nucleons only (dashed lines). In Fig. 2.11 we can see that the real and imaginary functions of the considered processes, $\omega \rightarrow \gamma^* \pi^0$ and $\rho^a \rightarrow \gamma^* \pi^a$, are changed in comparison to Fig. 2.7. The features of the dashed lines,

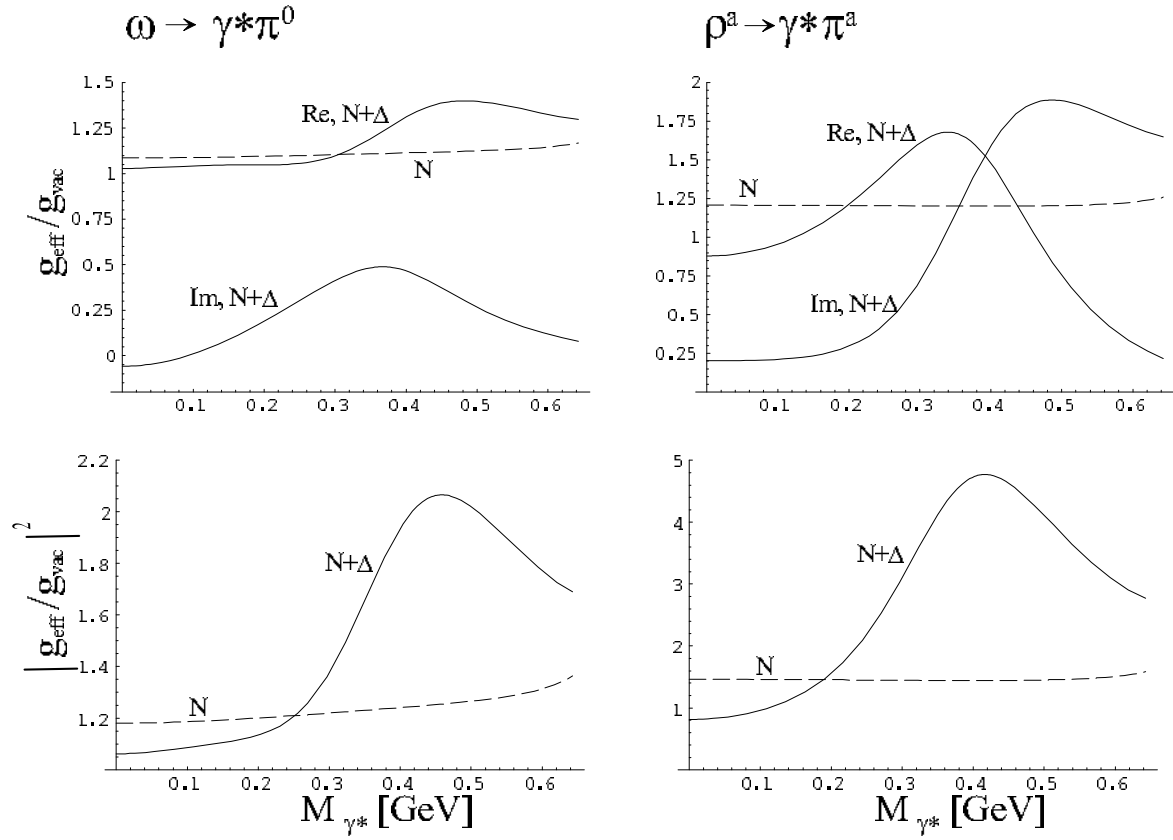


Figure 2.11: The ratio of the effective coupling constant to its vacuum value at the nuclear saturation density for the decays $\omega \rightarrow \gamma^* \pi^0$ and $\rho^a \rightarrow \gamma^* \pi^a$, plotted as a function of the virtuality of the photon, M_{γ^*} . The solid and the dashed lines correspond to the calculations with all diagrams of Fig. 2.3, and calculations with diagrams including only nucleons, respectively. Top plots show the real and imaginary parts for all considered cases. We use $\Gamma_\Delta = 120$ MeV.

corresponding to the calculations with nucleons only, remain practically unchanged. Both lower plots indicate that for the case with the Δ , the change of M_{γ^*} in the kinematic range above 0.2 GeV has a visible effect on the effective coupling constant. We have already mentioned this when discussing Fig. 2.10.

Finally, we complete our discussion of the $\pi\omega\rho$ vertex at $\mathbf{q} = \mathbf{0}$ with Fig. 2.12, which shows the result of the calculation for the values m_N and M_Δ reduced to 70%. In this case there are significant differences compared to the unreduced mass, Fig. 2.11. We can see that the effective coupling constant g_{eff} is enhanced by about 1.5 for the $\omega \rightarrow \pi^0 \gamma^*$ decay and by about 6 for $\rho^a \rightarrow \pi^a \gamma^*$ decay, and shifted to higher values of M_{γ^*} , above 0.4 GeV.

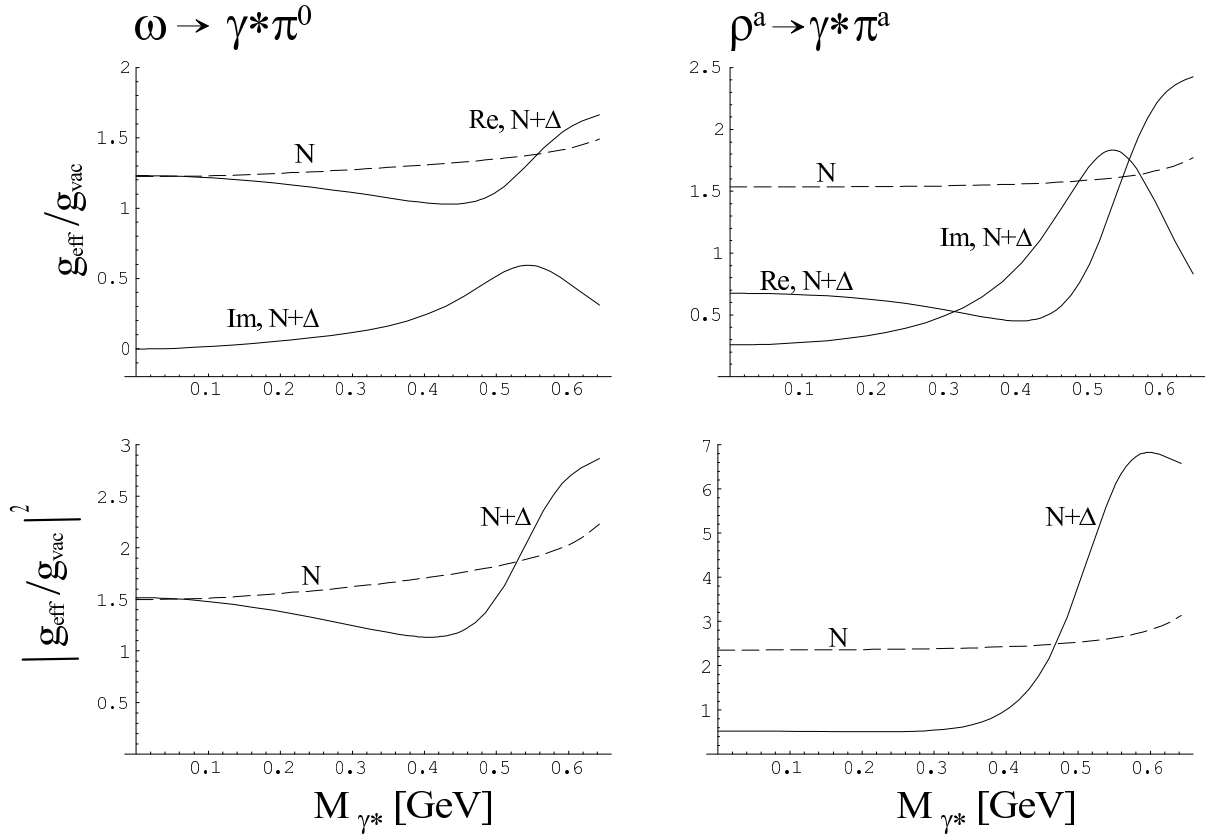


Figure 2.12: Same as Fig. 2.11, but for the values of m_N and M_Δ reduced to 70%.

2.3 Decay of particles moving with respect to the medium

So far we have presented our results for the $\pi\omega\rho$ vertex for the decays of particles at rest with respect to the medium and we have pointed out large medium effects already at the nuclear saturation density. Now, we will introduce the general kinematic case of finite three-momentum of the decaying particle with respect to the medium, and calculate the widths and spectral functions in the transverse and longitudinal polarization channels.

In view of the substantial increase of the coupling constant for the ω and ρ decays when these particles are at rest with respect to the medium, we expect that the effect survives for particles moving with respect to the medium. We analyze the $\omega \rightarrow \pi^0 \gamma^*$ and $\rho^a \rightarrow \pi^a \gamma^*$ processes in the case where the ω and ρ meson move with a non-zero momentum with respect to the medium, denoted by \mathbf{q} . The ω and ρ particles can have transverse or longitudinal polarization, defined by quantizing the spin along the direction of \mathbf{q} . In medium the properties of these particles are different for these two polarizations; in particular, their widths Γ^L and Γ^T are different.

Kinematics

We consider the kinematics for the decay $\omega \rightarrow \pi^0 \gamma^*$ in the rest frame of the medium (not in the rest frame of the decaying particle as it is usually done in calculations in the vacuum). Thus the four-velocity of the medium is $u = (1, 0, 0, 0)$, and

$$\begin{aligned} q^2 &= m_\omega^2, & q \cdot u &= q_0 = \sqrt{m_\omega^2 + |\mathbf{q}|^2}, & p \cdot u &= p_0, \\ p \cdot q &= p_0 q_0 - \cos \alpha |\mathbf{p}| |\mathbf{q}|, & p^2 &= p_0^2 - |\mathbf{p}|^2 = M_{\gamma^*}^2, \end{aligned} \quad (2.47)$$

where q and p are the momenta of the ω and γ^* , respectively. Using the energy conservation:

$$E_\omega = E_{\gamma^*} + E_\pi, \quad (2.48)$$

where

$$\begin{aligned} E_\omega &= \sqrt{m_\omega^2 + |\mathbf{q}|^2}, & E_{\gamma^*} &= \sqrt{M_{\gamma^*}^2 + |\mathbf{p}|^2}, \\ E_\pi &= \sqrt{m_\pi^2 + |\mathbf{p}|^2 + |\mathbf{q}|^2 - 2 \cos \alpha |\mathbf{p}| |\mathbf{q}|}, \end{aligned} \quad (2.49)$$

we find in general two solutions for the momentum $|\mathbf{p}|$:

$$\begin{aligned} |\mathbf{p}^{(1,2)}| &= \frac{|\mathbf{q}| \cos \alpha (m_\pi^2 + M_{\gamma^*}^2 + m_\omega^2)}{2(M_{\gamma^*}^2 + \mathbf{q}^2 \sin^2 \alpha)} \pm \\ & q_0 \sqrt{m_\pi^4 - 2m_\pi^2(M_{\gamma^*}^2 + m_\omega^2) + M_{\gamma^*}^4 + m_\omega^4 - M_{\gamma^*}^2(4 \sin^2 \alpha |\mathbf{q}|^2 + 2m_\omega^2)}, \\ p_0^{(1,2)} &= \sqrt{M_{\gamma^*}^2 + (\mathbf{p}^{(1,2)})^2}, \end{aligned} \quad (2.50)$$

We consider two cases which are shown in Fig. 2.13.

Depending on the value of $|\mathbf{q}|$ we may have a case where only one branch for $|\mathbf{p}|$ is present, or where two branches appear. When $|\mathbf{q}|$ is smaller than some critical value q_{crit} we have the situation of Fig. 2.13(A). The values of $|\mathbf{p}|$ belong to one branch, and α takes all values between $-\pi$ and π . When $|\mathbf{q}|$ is larger than q_{crit} then we have the situation depicted in Fig. 2.13(B). For each value of α in the allowable range we have two branches. The angle α has a maximum value α^* when $|\mathbf{p}^1| = |\mathbf{p}^2|$. Solving the equation corresponding to this condition we find that

$$\alpha^* = \arcsin \left(\frac{1}{2|\mathbf{q}|M_{\gamma^*}} \sqrt{m_\pi^4 - 2(M_{\gamma^*}^2 + m_\omega^2)m_\pi^2 + (M_{\gamma^*}^2 - m_\omega^2)^2} \right). \quad (2.51)$$

The transition between the behavior of Fig. 2.13 A) and B) occurs for $q = q_{\text{crit}}$. The value of q_{crit} follows from the condition $|\mathbf{p}^2| = 0$ for $\alpha = 0$ as is clear from Fig. 2.13. This condition yields, from Eq. 2.50

$$\frac{\sqrt{m_\pi^4 - 2(M_{\gamma^*}^2 + m_\omega^2)m_\pi^2 + (M_{\gamma^*}^2 - m_\omega^2)^2}}{2M_{\gamma^*}} = q_{\text{crit}}. \quad (2.52)$$

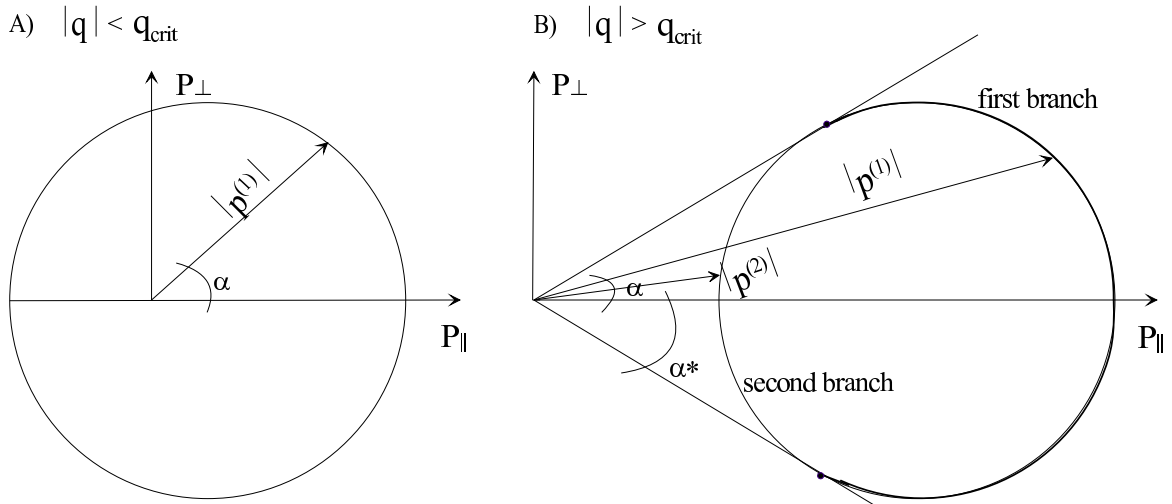


Figure 2.13: The $\omega \rightarrow \pi^0 \gamma^*$ decay in the case where the ω meson moves with a non-zero momentum $|\mathbf{q}|$ with respect to the medium. Figure A): the situation when $|\mathbf{q}|$ is smaller than q_{crit} , and the values of $|\mathbf{p}|$ belong to the first branch of Eq. 2.50. The angle α (between momentum $|\mathbf{p}|$ and $|\mathbf{q}|$) takes values from $-\pi$ to π . Figure B): for each value of α in the allowable range there are two branches. The second branch appears only for $|\mathbf{q}|$ above the critical value.

Transverse and longitudinal polarizations

Now we are equipped with appropriate kinematic expressions to consider the width of the transversely and longitudinally polarized ω meson due to the decay $\omega \rightarrow \pi^0 \gamma^*$. The expression for the width has the form

$$\Gamma_{\omega \rightarrow \pi^0 \gamma^*} = \frac{1}{n_s} \sum_{ss'} \frac{1}{2q_0} \int \frac{d^3 p}{(2\pi)^3 2p_0} \int \frac{d^3 p'}{(2\pi)^3 2p'_0} |\mathcal{M}_{ss'}|^2 (2\pi)^4 \delta^{(4)}(q - p - p'), \quad (2.53)$$

where s is the polarization of the ω , s' is the polarization of the γ^* , n_s is the number of spin states of the ω meson, and $|\mathcal{M}_{ss'}|^2$ is the transition amplitude. We perform the phase-space integral with the kinematics discussed above and obtain

$$\Gamma_{\omega \rightarrow \pi^0 \gamma^*} = \frac{1}{n_s} \sum_s \frac{1}{2q_0} \left[\theta(q_{\text{crit}} - q) \sum_{b=1} \int_0^\pi d\alpha + \theta(q - q_{\text{crit}}) \sum_{b=1,2} \int_0^{\alpha^*} d\alpha \right] \sin \alpha \frac{(\mathbf{p}^{(b)})^2}{8\pi p_0^{(b)} (q_0 - p_0^{(b)}) |a^{(b)}|} |\mathcal{M}_{ss'}|^2, \quad (2.54)$$

where \sum_b is the sum over the one or two branches, and expressions

$$a^{(1,2)} = \frac{d(q_0 - \sqrt{M^2 + r^2} - \sqrt{m_\pi^2 + r^2 - 2r|\mathbf{q}| \cos \alpha + \mathbf{q}^2})}{dr} \Big|_{r=|\mathbf{p}^{(1,2)}|}, \quad (2.55)$$

are the factors from the Dirac delta function $\delta(E_\omega - E_p - E_\pi)$.

The ω meson has transverse polarization described by the polarization vectors $\varepsilon_{(\pm)}^\mu$, and $\varepsilon_{(0)}^\mu$. Using explicit forms of these polarization vectors one finds the following formulas [71, 72]:

$$\begin{aligned} -\varepsilon_{(+)}^{\mu*} \varepsilon_{(+)}^\nu - \varepsilon_{(-)}^{\mu*} \varepsilon_{(-)}^\nu &= \\ g^{\mu\nu} - u^\mu u^\nu - \frac{(q^\mu - q \cdot u u^\mu)(q^\nu - q \cdot u u^\nu)}{q \cdot q - (q \cdot u)^2} &\equiv T^{\mu\nu}(q), \\ -\varepsilon_{(0)}^{\mu*} \varepsilon_{(0)}^\nu &= -\frac{q^\mu q^\nu}{q \cdot q} + u^\mu u^\nu + \frac{(q^\mu - q \cdot u u^\mu)(q^\nu - q \cdot u u^\nu)}{q \cdot q - (q \cdot u)^2} \equiv L^{\mu\nu}(q), \end{aligned} \quad (2.56)$$

The tensors $T^{\mu\nu}$ and $L^{\mu\nu}$ are defined with such signs as to form projection operators, *i.e.*, $T^{\mu\nu} T_\nu^\alpha = T^{\mu\alpha}$, $L^{\mu\nu} L_\nu^\alpha = L^{\mu\alpha}$, and $T^{\mu\nu} L_\nu^\alpha = 0$. Furthermore, we have $T^{\mu\nu} q_\nu = 0$ and $L^{\mu\nu} q_\nu = 0$, which reflects current conservation, as well as $T^{\mu\nu} u_\nu = 0$.

By summing over all polarizations, we find the usual expression

$$-\sum_{s=\pm,0} \varepsilon_{(s)\mu}^* \varepsilon_{(s)\nu} = T^{\mu\nu} + L^{\mu\nu} = g^{\mu\nu} - \frac{q^\mu q^\nu}{q \cdot q} = Q^{\mu\nu}(q). \quad (2.57)$$

Now we return to an expression for the width, Eq. 2.53. We write the transition amplitude

$$\begin{aligned} \frac{1}{n_s} \sum_{ss'} |\mathcal{M}_{ss'}|^2 &= \frac{1}{n_s} \sum_{ss'} [\varepsilon_{(s')\mu} A^{\mu\nu} \varepsilon_{(s)\nu} \varepsilon_{(s)\nu'}^* A^{\nu'\mu'*} \varepsilon_{(s')\mu'}^*] \\ &= \frac{1}{n_s} \sum_s A^{\mu\nu} \varepsilon_{(s)\nu}^{(\omega)} \varepsilon_{(s)\nu'}^{(\omega)*} A^{\nu'\mu'*} (-Q_{\mu\mu'}(p)), \end{aligned} \quad (2.58)$$

where $\varepsilon_{(s')\mu}$ is a polarization vector for γ^* and $\varepsilon_{(s)\nu}$ is the polarization vector for the ω meson. Summing over $s = 0$, and $s = \pm$ we obtain, respectively,

$$\begin{aligned} |\mathcal{M}_L|^2 &= L_{(\omega)}^{\nu\nu'} Q_{(\gamma^*)}^{\mu\mu'} A_{\mu\nu} A_{\mu'\nu'}^* \\ |\mathcal{M}_T|^2 &= \frac{1}{2} T_{(\omega)}^{\nu\nu'} Q_{(\gamma^*)}^{\mu\mu'} A_{\mu\nu} A_{\mu'\nu'}^*. \end{aligned} \quad (2.59)$$

Combining Eq. 2.54 and 2.59 we may write the final expression

$$\begin{aligned} \Gamma_{\omega \rightarrow \pi^0 \gamma^*}^P(|\mathbf{q}|) &= \frac{1}{n_P} \frac{1}{2q_0} \left[\theta(q_{\text{crit}} - |\mathbf{q}|) \sum_{b=1} \int_0^\pi d\alpha + \right. \\ &\quad \left. + \theta(|\mathbf{q}| - q_{\text{crit}}) \sum_{b=1,2} \int_0^{\alpha^*} d\alpha \right] \sin \alpha \frac{(\mathbf{p}^{(b)})^2}{8\pi p_0^{(b)} (q_0 - p_0^{(b)}) |a^{(b)}|} |\mathcal{M}_P|^2, \end{aligned} \quad (2.60)$$

Results for transverse and longitudinal widths

Our numerical results for the $\omega \rightarrow \pi^0 \gamma^*$ decay are shown in Fig. 2.14. We present the dependence of widths for the transverse and longitudinal polarization on the virtuality

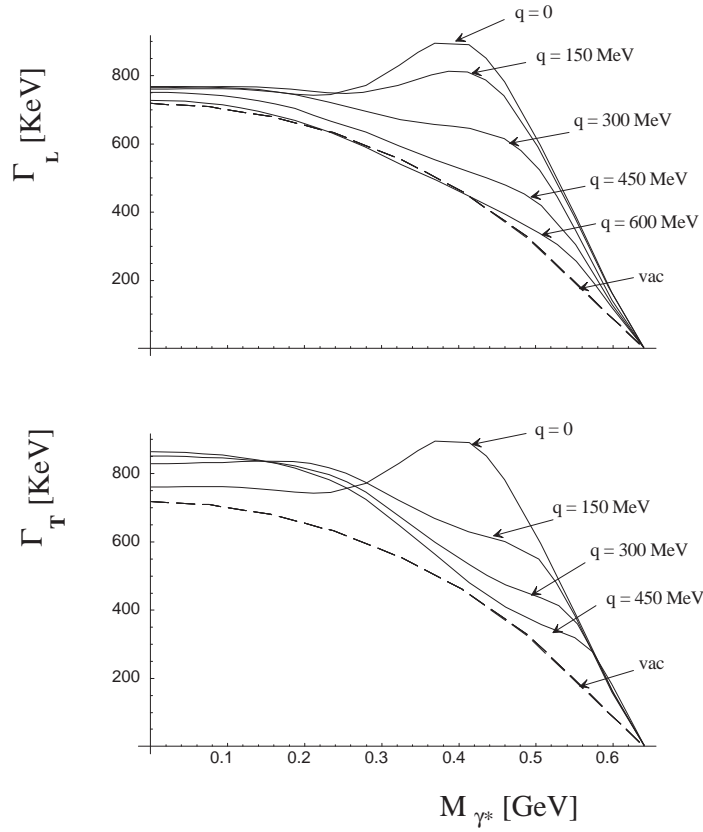


Figure 2.14: The longitudinal (top) and transverse (bottom) widths for the $\omega \rightarrow \pi^0 \gamma^*$ decay, plotted as a function of the virtuality of the photon, M_{γ^*} . The dashed and solid lines show the vacuum and medium cases for $\rho_B = \rho_0$, respectively.

of the photon, M_{γ^*} . We have used here the constant $\Gamma_\Delta = 120$ MeV. Calculations are done for different values of $|\mathbf{q}|$. From Fig. 2.14 we can conclude that the transverse and longitudinal widths decrease with momentum $|\mathbf{q}|$, and the medium effect is weakened with increasing momentum $|\mathbf{q}|$. However, we can observe that the effect remains substantial for $|\mathbf{q}|$ up to ~ 200 MeV, the relevant value for temperatures typical in heavy-ion collisions. As it is commonly known in a fireball formed in relativistic heavy-ion collisions, the momenta are lower than a typical temperature ~ 150 MeV.

We present analogous results for the $\rho^a \rightarrow \pi^a \gamma^*$ decay in Fig. 2.15. We notice again that while $|\mathbf{q}|$ increases from 0 to 600 MeV, the medium effect is weakened, and both the transverse and longitudinal widths decrease.

We see that the medium effect is large for the typical momenta up to ~ 200 MeV. For higher momenta this effect is lower; however it still remains visible compared to the vacuum result, see the dashed line in Fig. 2.15.

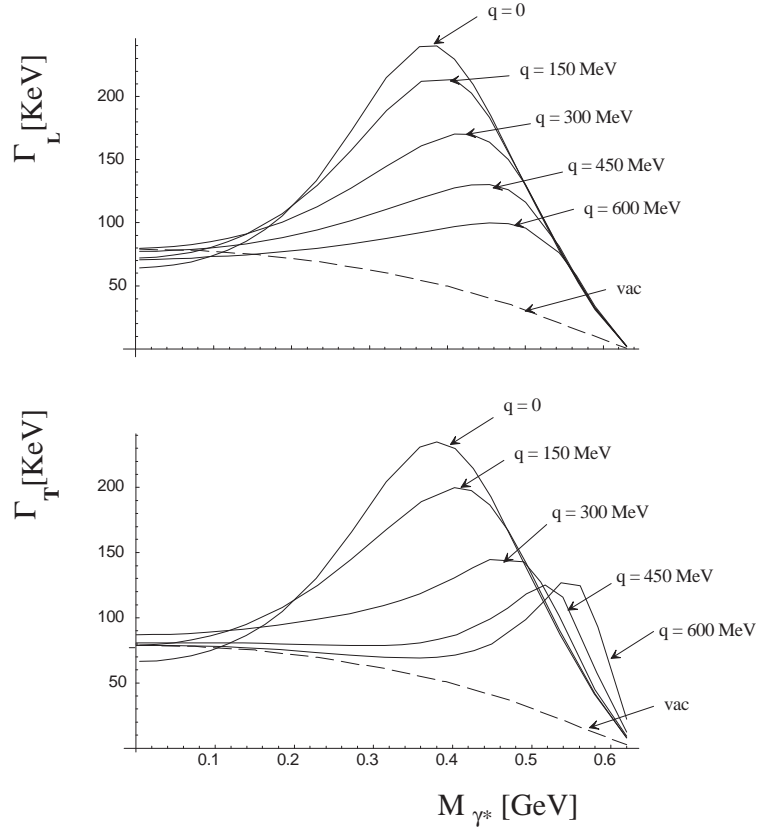


Figure 2.15: The longitudinal (top) and transverse (bottom) width for the $\rho^a \rightarrow \pi^a \gamma^*$ decay, plotted as a function of the virtuality of the photon, M_{γ^*} . The dashed and solid lines show the vacuum and the medium cases, respectively.

Chapter 3

Summary of Part I

The main conclusion of our investigations in this part of the thesis is that the medium effects on the $\pi\omega\rho$ coupling in the discussed Dalitz processes $\omega \rightarrow \pi^0\gamma^*$, $\rho^a \rightarrow \pi^a\gamma^*$ are large. Moreover, these medium effects come dominantly from the processes where the Δ isobar is excited in the intermediate state. On the other hand, for the $\pi^0 \rightarrow \gamma\gamma^*$ the effects of the Δ isobar cancel almost exactly the effects of the nucleon particle-hole excitations, such that the medium effect is small. The Dalitz yields from the π^0 decays are not altered by the medium for two reasons: first, virtually all pions decay outside of the fireball due to their long lifetime; second, the width for this decay is practically unaltered by the medium.

At the nuclear saturation density, for the Dalitz decays from the ρ and ω mesons, the value of the effective coupling constant is enhanced compared to the vacuum value. The increased coupling constant greater by about a factor of 2 for the ω meson and by about a factor of 5 for the ρ , leads directly to large widths of the ω and ρ mesons in medium.

Next, we have analyzed the case where the decaying particle (ρ or ω) moves with respect to the medium. In this case we have to look separately at the longitudinal and transverse polarizations. The properties of mesons are different for these polarizations. We investigated the dependence of the widths for transverse and longitudinal polarization on the invariant mass of dileptons. This leads to the conclusion that the medium effects decrease with growing magnitude of three-momentum, but remain significant for typical momenta in heavy-ion collisions, $q \lesssim 200$ MeV.

The enhancement of the coupling constant directly affects the calculations of the dilepton production in relativistic heavy-ion collisions. An increased value of width results in an increased dilepton yield. In the next part we will apply our model to evaluate the dilepton production from the ρ and ω decays in heavy-ion collisions.

Part II

Dilepton production rate

Chapter 4

Electromagnetic signals from hot and dense matter

In this part of the thesis we use directly the results of Part I. We focus on the production of dileptons in hadronic decays, which is an area of great interest from a theoretical point of view. We will investigate the theoretical yields from the Dalitz decays of vector mesons in the region of $0.2 - 0.6$ GeV, where many existing calculations have problems to explain the CERES and HELIOS experiments [4, 5, 21, 22, 73, 74, 75, 36, 76]. Our purpose is to see to what extent the medium modification of the $\pi\omega\rho$ vertex influences the dilepton production, and may be significant in understanding the experimental data in the region of low invariant masses.

As we mentioned in the Introduction, electron pairs are produced in all stages of ultrarelativistic heavy-ion collisions. Because of the small electromagnetic coupling constant, they carry undistorted information about the densest and hottest phases of the heavy-ion collisions where chiral symmetry restoration and/or quark gluon plasma (QGP) formation are expected.

The first pairs of leptons are created during the stage when two nuclei pass through each other, while the last pairs are formed when the hadrons are decoupled and move freely to the detectors. After decoupling of hadronic matter the greater part of dileptons is produced by the electromagnetic decays of hadronic resonances. For pair masses below $140 \text{ MeV}/c^2$ the π^0 Dalitz decay dominates the spectrum, whereas at higher masses the ω , ρ , η , η' and ϕ decays should be most significant.

The dilepton mass spectra are very important for the study of the in-medium properties of vector mesons, which we have discussed in detail in Part I.

As we have pointed out in the Introduction, experimental measurements of dilepton mass spectra can be divided into three mass regions. The low mass region, below

1 GeV, is dominated by hadronic interactions and hadronic decays at freeze-out. It is particularly sensitive to in-medium modifications of the light hadrons. The intermediate mass region lies between 1 GeV and about 2.5 GeV, where the contribution from the thermalized QGP might be seen. We want to mention that the physical picture of QGP structure has changed in the last year. Now, many theoretical developments [77, 78] suggest that the matter produced at RHIC, in the high temperature region $T_c < T < 4T_c$, is a strongly coupled quark gluon plasma (sQGP) contrary to the previous expectations which were based on weakly coupled quasiparticle gas. In order to understand what sQGP is, one may have a look at two other examples of the strongly coupled systems such as trapped ultra-cold atoms in a large scattering length regime or supersymmetric Yang-Mills gauge theories at strongly coupling limit (Conformal Field Theory with a non-running coupling at finite temperature). Finally, the high mass region at and above $m_{J/\Psi}$ is important in connection with the suppressed J/Ψ production with respect to the background from the Drell-Yan process of the quark-antiquark annihilation.

So far, the experimental measurements of dilepton yields in heavy-ion collisions have mainly been carried out at the CERN SPS facility by three collaborations: the CERES (Cherenkov Ring Electron Spectrometer) collaboration has measured dielectron spectra in the low-mass region [4, 13, 14], the HELIOS-3 collaboration has specialized in dimuon spectra up to the J/Ψ region [5], and the NA38/NA50 [15, 16, 17] collaborations have been dedicated to study of dimuon spectra in the intermediate and high-mass region, emphasizing the J/Ψ suppression. Dilepton data have also been taken by the DLS collaboration at BEVALAC [19, 20] at much lower bombarding energies of about 1 – 2 A GeV.

The study of the low mass dileptons between 0.2 – 0.6 GeV has recently become of considerable interest. In this region the dilepton continuum originates from the Dalitz decays of neutral mesons such as $\pi^0, \eta, \eta' \rightarrow e^+e^-\gamma$ and $\omega \rightarrow e^+e^-\pi^0$. The resonance peaks are due to direct decays, $\omega, \rho, \phi \rightarrow e^+e^-$. In central heavy-ion collisions the low mass dilepton enhancement is observed by the CERES and HELIOS-3 collaborations. This enhancement has been studied in various approaches, ranging from hydrodynamical models to complicated transport models. The calculations based on the cocktail model, which are designed to describe the proton-induced reactions, work very well for light-heavy systems, but fail to explain the observed phenomenon in nucleus-nucleus collisions. Various medium effects, such as the dropping vector meson masses, as first proposed by Brown and Rho [1], the modification of the rho meson spectral functions, or the enhanced production of η have been proposed to explain the observed

enhancement.

In the intermediate-mass region from about 1 GeV to about 2.5 GeV the excess of dileptons has also been observed by both the HELIOS-3 and NA38/NA50 collaborations. This enhancement is observed in central S+W, S+U, and Pb+Pb collisions in comparison to proton-induced reactions [5, 15, 16, 17]. The intermediate-mass dilepton spectra are particularly useful in the search for QGP.

The J/Ψ suppression in the high-mass region above 2.5 GeV is a very interesting problem. It was interpreted as a signal of QGP formation by Matsui and Satz already in 1986 [79]. Nowadays, there is an indication from experimental data that up to central S+Au collisions pre-resonance absorption in nuclear matter is sufficient to account for the observed J/Ψ suppression [80]. However, data for central Pb+Pb collisions from NA50 collaboration show an additional strong J/Ψ suppression, which is interpreted as a signal of color deconfinement [81, 82].

Below we discuss mainly the enhancement of the low-mass dileptons, because we have found, in Part I, that the considered $\pi\omega\rho$ coupling constant is sizeable enhanced in the medium just in the region between 0.2 – 0.6 GeV of the invariant mass of dileptons. Hence in this region the modifications of the vertex directly influence the dilepton production rate.

4.1 Overview of experimental measurements

The CERN SPS is the first machine used for systematic investigations of the dilepton production in ultrarelativistic hadron-nucleus and nucleus-nucleus collisions. In this section we review the CERN-SPS dilepton experiments CERES, HELIOS, and NA38/NA50. Since the dilepton spectra are usually compared to the expected contributions from hadron decays, the co-called *hadronic cocktail*, we begin this section by a short description of the hadronic cocktail model.

Hadronic cocktail

The hadronic cocktail is used to simulate the relative abundance of dielectrons produced by hadron decays in proton-nucleus and nucleus-nucleus collisions at the invariant mass range covered by the CERES acceptance ($m_{ee} < 2$ GeV). This invariant mass range is dominated by the decay of light scalar and vector mesons, such as π^0 , η , η' , ρ^0 , ω , and ϕ . The hadronic cocktail treats proton-nucleus and nucleus-nucleus collisions as a superposition of individual nucleon-nucleon collisions and gives a reference to compare with the experimental observed dilepton yield. As input for this simula-

tion one needs to know differential cross sections, the widths of all decays including dileptons in the final state, and the decay kinematics for all involved particles.

The proton-nucleus collisions are approximated by a superposition of nucleon-nucleon collisions, i.e. the proton-nucleus yield is obtained by rescaling the nucleon-nucleon yield with the mean charge-particle multiplicity of the colliding system. For Pb-Au collisions the relative cross sections (σ/σ_{π^0} , where σ is the cross section for a particular hadron decay into the electron pairs) are taken from a thermal model, [83]. In order to compare with experiments the hadronic cocktail contribution is divided by the total number of charged particles within the acceptance of the detector. The sum of all contributions from hadron decays is calculated with Monte-Carlo event generator. The invariant mass spectrum is calculated including all known hadronic sources. The particle ratios of these sources are assumed to be independent of the collision system and to scale with the number of produced particles. Their p_\perp -distribution are generated assuming m_\perp -scaling, [84] based on the pion p_\perp spectrum from different experiments and fitted [85] to the formula:

$$\frac{dN}{dp_\perp} \sim p_\perp \exp\left[-\frac{m_\perp}{T_{\text{eff}}}\right], \quad (4.1)$$

where for SPS at energy 158 A GeV the inverse slope parameter is parameterized as

$$T_{\text{eff}} = 175 \text{ GeV} + 0.115 \text{ m[GeV]}, \quad (4.2)$$

with meson mass indicated as m. The rapidity distribution is a fit to measured data. All Dalitz decays are treated according to the Krall-Wada [86] expressions with the experimental transition form factors taken from Ref. [87]. The vector meson decays are generated using the expressions derived by Gounaris and Sakurai [88].

Charm production is not taken into account since it is negligible in the low-mass range. Finally the laboratory momenta of the electrons are constructed with the experimental resolution and acceptance.

The differences between hadron cocktail and experiment indicate the existence of in-medium effects or the violation of the scaling behavior.

4.1.1 CERES/NA45 experiments

The only experiment which measures the low-mass dilepton pairs up to about 1.2 GeV is the CERES/NA45 experiment. This collaboration carries out systematic measurements of dilepton spectra in proton-induced reactions. Figure 4.1, taken from [89], shows the data on dielectrons of proton-induced collisions at 450 GeV in comparison to the expected contributions of hadron decays, the *hadronic cocktail*. For instance,

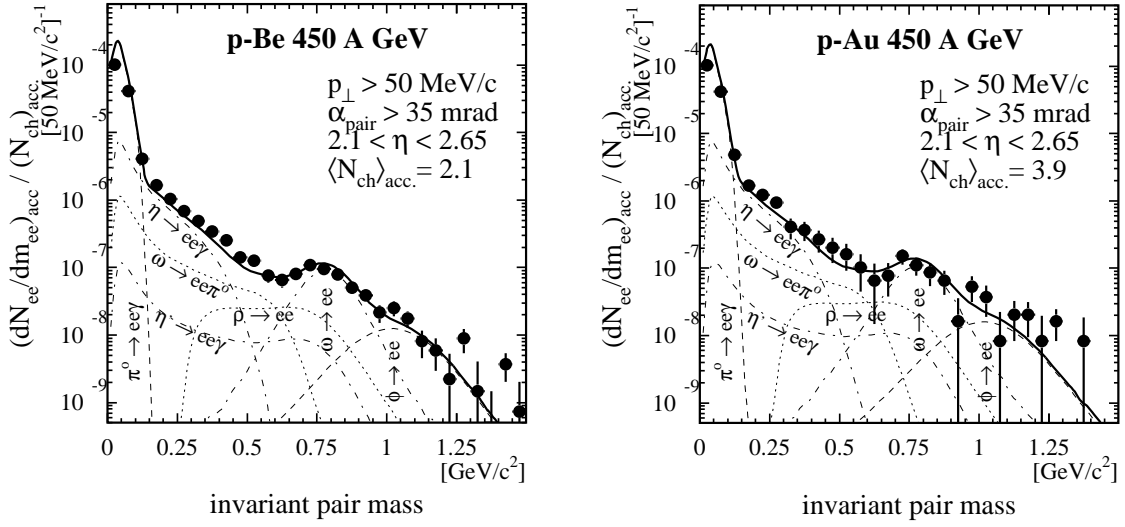


Figure 4.1: Dilepton invariant mass spectrum of p+Be and p+Au collisions at the incident proton energy of 450 GeV, taken from [89]. The expected sources from hadron decay (solid lines) and the experimental points are in excellent agreement.

the dashed curves in Fig 4.1 give the expected dielectron spectra from hadron decays for p-Be and p-Au reactions. The total expected cocktail of hadronic sources is denoted by the solid line. We observe that the dilepton yield is fitted by the cocktail model very well. The situation is different for dilepton spectra in central S+Au and Pb+Au collisions at 200 A GeV and 158 A GeV, respectively, see Fig. 4.2 from [89]. The dielectron yield significantly exceeds the expectations extrapolated from proton-induced reactions. The enhancement is most pronounced in the invariant mass region 0.2 – 0.6 GeV. In both cases the difference between the experimental and the cocktail model is about a factor of 6, whereas in p-induced reactions the spectrum from 0.2 to 0.6 GeV reproduces the data. The CERES collaboration has also studied the low-mass dielectrons in Pb+Au collisions at the lower energy of 40 GeV, see Fig. 4.3. Enhancement of the dilepton yield, related to the expected yield of hadronic sources, is even more pronounced than at the energy of 158 A GeV [90].

The difficulty in explaining this experimental fact has become known as the *dilepton puzzle* and is an important theoretical or experimental problem.

4.1.2 HELIOS experiments

In the HELIOS experiments there are three collaborations. The HELIOS-1 collaboration [91] was the pioneer in the measurement of the dilepton spectrum at CERN SPS. It was the only experiment that measured both the e^+e^- and $\mu^+\mu^-$ pair produc-

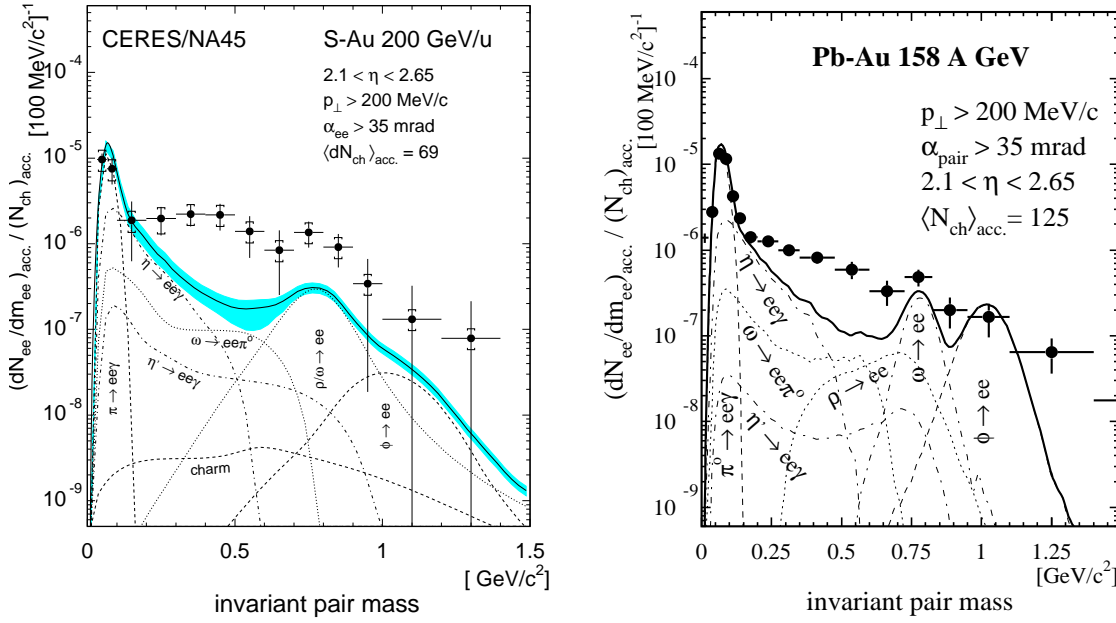


Figure 4.2: Dilepton invariant mass spectrum of S+Au and Pb+Au collisions at 200 GeV and 158 GeV from CERES collaboration, [89]. The data is compared to expected cocktail of hadronic sources. A visible increase of dilepton production is observed in the region $0.2 - 0.6$ GeV.

tion in p+Be reactions at 450 GeV as well as the first in which the hadron cocktail contribution to the dilepton spectra was analyzed. The conclusion is that the measured dielectron and dimuon spectra in p+Be collisions are described by the cocktail hadron decays, which was later confirmed by the CERES collaboration with much greater precision. The HELIOS-2 collaboration [93] was the first to measure the photon signals using the S and O beams at the CERN SPS energy. Very small direct photon enhancement (of about a few percent) was observed in these studies. This observation was later confirmed by the CERES and WA80 collaborations with better statistics.

The HELIOS-3 experiment [5] is designed to study the dimuon production in p+W and S+W collisions at 200 GeV, and covers the low- and intermediate-mass region. In Fig. 4.4, taken from [92], we see the results for p+W collisions (left) and S+W collisions (right). For p+W collisions the low mass dimuons are mainly from the η Dalitz decay, while the omega meson Dalitz decay is important in the mass region $0.2 - 0.6$ GeV. The cocktail contribution is in agreement with the experimental points. For the S+W collisions the dimuon production is enhanced in both the low-mass and intermediate-mass regions, as compared to the proton-nucleus collisions.

In the low dimuon invariant mass region the enhancement factor is smaller than

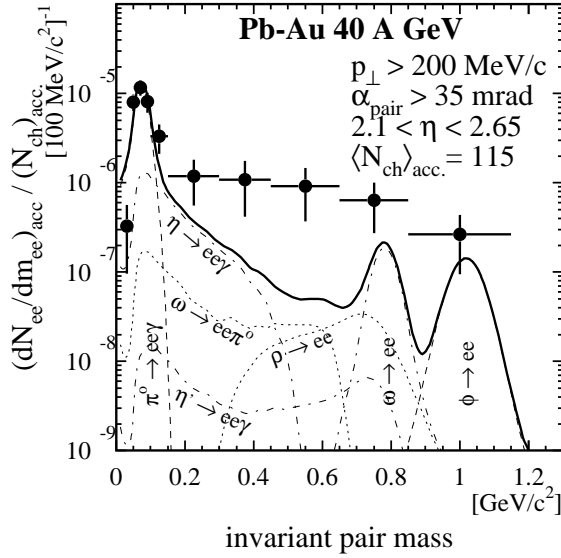


Figure 4.3: Dielectron invariant mass spectrum of Pb+Au collisions at 40 A GeV taken from [89]. The data is compared to the expected cocktail of hadronic sources (solid line).

that found by the CERES collaboration in central collisions. One of the possible reasons for this difference is that the HELIOS-3 experiment covers more forward pseudorapidities, $3.7 \leq \eta \leq 5.2$, than the CERES experiment which is close to the midrapidity region, $2.1 \leq \eta \leq 2.65$. A significant excess in the dimuon yield in the intermediate-mass region is also reported, with an enhancement factor of about 2 [5].

4.1.3 NA38/NA50 experiments

The NA38 and NA50 experiments specialize in the study of the J/Ψ suppression in heavy-ion collisions. These collaborations measured the dimuon spectra in a mass region from the threshold to about 8 GeV. The measurements are carried out at energies of 200 A GeV for the p+W and S+U reactions (NA38), and 160 A GeV for the Pb+Pb reactions (NA50). A situation similar to that described for other experiments occurs.

In proton-induced reactions the data are described with a rather good agreement as compared to the expected sources from hadron decay. On the other hand, for S+U and Pb+Pb reactions significant enhancement for low- and intermediate-mass region is observed. This shift is more visible in Pb+Pb collisions in the mass region around 2 GeV. The data from NA38/NA50 experiments have no centrality selection, whereas the CERES collaboration measures central collisions.

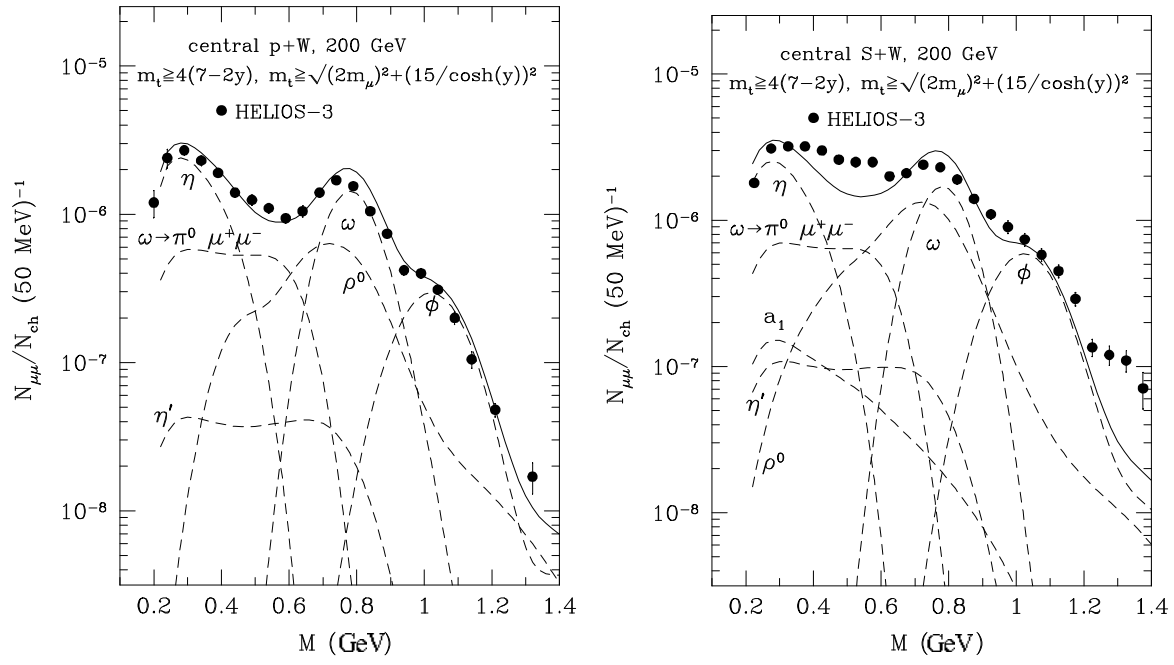


Figure 4.4: Dilepton invariant mass spectrum of p+W (left) and S+W (right) collisions at 200 GeV from HELIOS-3 collaboration. The data is compared to expected cocktail of hadronic sources, [92].

4.1.4 Dilepton spectra at BEVALAC energies

It is worth mentioning that the measurements of the dilepton production at much lower bombarding energies, in the range 1 – 5 A GeV, have been performed by the DLS collaboration at LBL BEVALAC [19, 20]. In this experiment a different temperature and density regime is probed. The dielectron spectra were measured for p+Be collisions at 1, 2.1 and 4.9 A GeV, for Ca+Ca reactions at 1 and 2 A GeV and for Nb+Nb at 1.05 A GeV. In the low invariant mass region from 0.2 – 0.6 A GeV production of dielectrons is found to be enhanced compared to estimates based on the theoretically known dilepton sources.

For ultra-relativistic reactions (SPS) the low-mass dilepton excess is explained by the reduction of the ρ -meson mass in a dense medium. The in-medium broadening of the ρ -meson is also expected to be sufficient to explain the dilepton yield at SPS energies. These explanations fail for the DLS data. This fact is known as the 'DLS puzzle'. The reason probably lies in the fact that the possible pQCD contributions and sufficient $\pi^+\pi^-$ annihilations are absent at this energies.

4.1.5 Other experiments

The new NA60 experiment studies the production of open charm and the production of dimuons instead of dielectrons in proton-nucleus and nucleus-nucleus collisions at CERN SPS. This experiment is a continuation of the NA38 and NA50 experiments but with significantly enhanced detector technology. The aim of the NA60 experiment is to examine various possible signatures of the transition from hadronic to deconfined partonic matter *e.g.*, charmonium suppression, dimuons from thermal radiation, and modifications of vector meson properties. The NA60 experiment is continuing with ^{115}In beams at least up to the year 2005, Ref. [18].

Dilepton spectra were also measured at KEK in p+A reactions at a beam energy of 12 A GeV [94]. Also here considerable enhancement over the expected yield from hadronic decays was observed below the ρ -meson peak. Explanations of the experimental spectrum within a dropping mass scenario or the broadening of vector meson are not proper in this case as they were not at the Bevalac energies. Similar experiments with much better statistics are planned at GSI SIS by the HADES collaboration [95].

Summarizing this section, in the low-mass region between 0.2-0.6 GeV of the invariant mass of the dilepton, experiments reported an unexpected enhancement of dileptons in nucleus-nucleus collisions with comparison to the extrapolation from more elementary proton-induced reactions. This has been a topic of great interest from a theoretical point of view, to which the next section is devoted.

4.2 Overview of theoretical models

In this section we would like to review various theoretical explanations that have been put forward to explain the experimental data discussed in the previous section. A lot of theoretical efforts has been devoted to understanding the experimental results in the low-mass region from the CERES and HELIOS experiments. Theorists have proposed possible explanations of the dilepton puzzle based on transport model calculations, many-body approaches, and the effects of dropping rho meson mass and/or increasing width.

The main contributions to e^+e^- pairs with mass below 300 MeV are: the direct leptonic decay of vector mesons such as ρ^0 , ω and ϕ , the pion-pion annihilation which proceeds through the ρ^0 meson, the kaon-antikaon annihilation that proceeds through the ϕ meson, and the Dalitz decay of π^0 , η , ω and ρ .

The CERES and HELIOS-3 data are in reasonable agreement with each other in

proton-induced reactions. They are well explained by the Dalitz and direct vector meson decays. In nucleus-nucleus collisions the substantial enhancement of low-mass dileptons in the mass region $0.2 - 0.6$ GeV remains unexplained. The difference between proton-induced and nucleus-nucleus reactions may lie in additional contributions from pion-pion and kaon-antikaon annihilation to dilepton production in heavy-ion collisions. Authors of [21, 22, 92, 23] have included the contributions from the pion-pion annihilation but neglected any medium effects.

The theoretical results are still in disagreement with data in the mass region of interest, which leads to the suggestion that medium modifications of vector mesons are needed [34, 36, 76]. It has been found that the models with the use of in-medium vector meson masses describe the CERES data much better than models with vacuum meson masses. The same situation occurs for the dimuon spectra from the central nucleus-nucleus collisions measured by the HELIOS-3 collaboration [92, 96].

The rho meson decays dominantly into two pions. The medium modifications of the pion dispersion relation and the rho-nucleon scattering contribute to the spreading of the rho meson spectral function, which results in enhancement of the production of low-mass dileptons from in-medium rho meson decay. This broadening of the rho meson spectral function provides a better description for the CERES [36, 76] and HELIOS-3 data.

Many calculations and mechanisms have been proposed for the explanation of the low-mass dilepton enhancement. Kapusta et al. [97] and Hung et al. [98] proposed that the in-medium reduction of the η and/or η' masses leads to an enhanced production of these mesons, which in turn increases the low-mass dilepton yield. The authors of [99, 100] studied the effects of an in-medium pion dispersion relation on dilepton production and they indeed found that the dilepton yield is enhanced near 0.4 GeV invariant mass. The contribution from the pion-rho annihilation has been studied in [101, 102]. This contribution was too small to explain the observed enhancement. Hung and Shuryak [103] also emphasized the effect of dropping a_1 meson mass, which is the chiral partner of the rho meson, on the very low-mass dileptons. On the other hand, Kluger et al. [104] studied dilepton production rates from the disoriented chiral condensate (DCC) state, and found that the dilepton yield with mass below 300 MeV from the DCC state can be significantly larger than that from the equilibrium state.

In other words, the low-mass dilepton enhancement reported by the collaborations from the previous section required the introduction of pion-pion annihilation and medium modifications of the meson properties. The dropping rho meson mass scenario, as implied by the Brown-Rho scaling conjectures and QCD sum rule calcu-

lations, provides a possible explanation of the observed enhancement. On the other hand, the medium modification of the rho meson spectral functions due to its interaction with baryons and medium modification of coupling constants also provides a reasonable description of experimental data.

Here we have discussed various theoretical approaches. Next in this thesis we follow the lines of Brown-Rho [1] and Rapp-Wambach [36, 76] and analyze medium modification of vector mesons.

Chapter 5

Formalism of the dilepton production from vector mesons

We are interested in the $\pi\omega\rho$ coupling constant which enters into the Dalitz decay of the ω and ρ meson. The Dalitz ρ decay is usually neglected in other analyses because of its absence in the Particle Data Book [105]. Nevertheless, it may occur and while it is less significant in the vacuum than the ω Dalitz decay, we will show that in the medium it becomes equally important.

We point out that we work at zero temperature. The authors of Ref. [35] have analyzed the finite temperature effects for the $\rho\pi\pi$ coupling. Such effects turn out to be very small, therefore in our analysis they are also neglected.

In our calculations we use the Vector Meson Dominance Model to estimate the dilepton yields from vector-meson decays. Apart from the Dalitz decays, an important source of additional dileptons in the region near twice the pion mass is the $\pi\pi$ annihilation. In this Chapter we first briefly review the VMD model. Next, we describe the structure of three-body Dalitz decays.

In order to calculate the dilepton spectrum one has to assume the evolution model of the collision system. Therefore, we review the Rapp-Wambach [26, 27] model of the hydrodynamic expansion of the fire cylinder, which we are going to apply in our calculations. In section 4.4 we discuss the kinematics for both direct and Dalitz decays with inclusion of effects of medium expansion in heavy-ion collisions. Thus we get the yield of dileptons produced during the expansion. In this analysis the Bose enhancement is neglected for brevity. Finally, we present our results and compare them to the CERES experimental data.

5.1 Vector Dominance Model (VDM)

The dilepton production rate per unit time and volume from the annihilation of pions, Fig. 5.1, is given by the formula

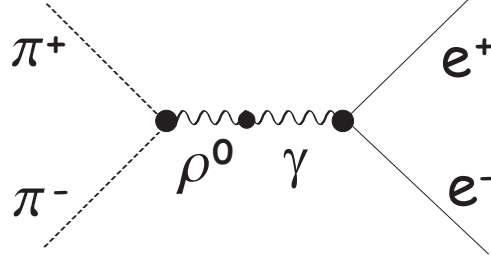


Figure 5.1: Vector Dominance Model of dilepton production from pion annihilation.

$$\frac{dN_{l+l-}}{d^4x} = \sum_{spins} \int dP_1 dP_2 dQ_1 dQ_2 f(p_1) f(p_2) (2\pi)^4 \delta^{(4)}(p_1 + p_2 - q_1 - q_2) |\mathcal{M}_{\pi^+\pi^- \rightarrow l+l-}|^2. \quad (5.1)$$

The sum runs over spins of leptons, where p_1 and p_2 are the four-momenta of the annihilating pions and q_1 and q_2 are the four-momenta of the outgoing leptons. The dP and dQ indicate the integration measures

$$dP_i = \frac{d^3p}{(2\pi)^3 2E_{p_i}}, \quad dQ_i = \frac{d^3q}{(2\pi)^3 2E_{q_i}}, \quad (5.2)$$

where $E_{p_i} = \sqrt{p_i^2 + m_\pi^2}$ and $E_{q_i} = \sqrt{q_i^2 + m_l^2}$, $i = 1, 2$. We use the following normalization for the lepton spinors, $\bar{u}u = \bar{v}v = 2m_l$. In Eq. 5.1 $f(p)$ is the pion distribution function of the form

$$f(p) = \left[\exp \frac{E_p - \mu_\pi}{T} - 1 \right]^{-1}, \quad (5.3)$$

with the pion chemical potential μ_π , incorporated in several works. The positive pion potential increases the number of pions over the equilibrium value, as discussed later on in section 5.3.

The matrix element $\mathcal{M}_{\pi^+\pi^- \rightarrow l+l-}$ is calculated in the framework of the VDM. According to this model the electromagnetic interactions of hadrons are described by the intermediate coupling of hadrons to vector mesons, Fig 5.1. The annihilation of the pions ($\pi^+\pi^- \rightarrow l^+l^-$) can be understood as the formation of a vector meson by the annihilation of pions and, the sequential decay of the vector meson into a lepton pair. Therefore, pions regain an electromagnetic form factor. The matrix element for

this process has the structure

$$\mathcal{M}_{\pi^+\pi^-\rightarrow l^+l^-} = \frac{1}{q^2} e L^\mu \sum_V \frac{e}{f_V} \frac{m_V^2}{m_V^2 - q^2 - im_V \Gamma_V} g_{\pi\pi V} (p_1 - p_2)_\mu, \quad (5.4)$$

where the term $m_V^2/(m_V^2 - q^2 - im_V \Gamma_V)$ comes from the vector meson propagator

$$G_V(q) = \frac{g^{\mu\nu} - \frac{q^\mu q^\nu}{m_V^2}}{q^2 - m_V^2 - im_V \Gamma_V}. \quad (5.5)$$

The quantities m_V and Γ_V are the mass and width of the vector meson V , the coupling of the vector meson to the virtual photon are described by the f_V parameter, $g_{\pi\pi V}$ is the effective coupling constant for the $\pi\pi V$ interaction, and $1/q^2$ comes from the photon propagator such as

$$G_\gamma^{\mu\nu} = \frac{g^{\mu\nu} - \frac{q^\mu q^\nu}{q^2}}{q^2} \quad (5.6)$$

with q denoting the four-momentum of the virtual photon ($q^2 = M^2$, the invariant mass squared of the lepton pair).

The quantity L^μ is the leptonic current which may be expressed in terms of the Dirac bispinors,

$$L^\mu(q_1, s_1; q_2, s_2) = 2m_l \bar{u}(q_1, s_1) \gamma^\mu v(q_2, s_2), \quad (5.7)$$

where s_1 and s_2 denote the spin variables of the outgoing leptons. The term

$$\sum_V \frac{e}{f_V} \frac{m_V^2}{m_V^2 - q^2 - im_V \Gamma_V} g_{\pi\pi V} (p_1 - p_2)_\mu \quad (5.8)$$

from Eq. 5.4, describes the coupling of the photon to two incoming pions via the electromagnetic form factor in the VDM including also the propagator of the intermediate vector meson.

5.2 Dalitz decays

The structure of the three-body Dalitz decays of the form $A \rightarrow B l^+ l^-$ is as follow: a particle decays A into B and a vector meson V which is subsequently converted into a virtual photon according to the vector dominance principle. Finally, the photon decays into the $e^+ e^-$ pair, see Fig 2.1. This process is usually called the 'internal conversion' of a virtual photon into a lepton pair. For these processes, where either a vector meson (V) or pseudoscalar meson (P) decays via $V \rightarrow P l^+ l^-$ or $P \rightarrow V l^+ l^-$, the transition amplitude has the invariant form

$$\mathcal{M}_{A \rightarrow B l^+ l^-} = L^\mu \epsilon^{\alpha\beta\gamma\mu} p_\alpha q_\beta \epsilon_\gamma \frac{e^2}{q^2} f_{AB}(M^2), \quad (5.9)$$

where L^μ is a leptonic current, p_α the four-momentum of meson B , q the four-momentum of the virtual photon γ^* , $q^2 = M^2$ the invariant mass squared of the lepton pair, $f_{AB}(M^2)$ is the electromagnetic form factor describing the $A \rightarrow B$ transition, and $\epsilon^{\alpha\beta\gamma\mu}$ is a totally antisymmetric tensor. We easily obtain the useful decomposition

$$|\mathcal{M}_{A \rightarrow B l^+ l^-}|^2 = |\mathcal{M}_{A \rightarrow B \gamma^*}|^2 \times \frac{1}{M^4} |\mathcal{M}_{\gamma^* \rightarrow l^+ l^-}|^2, \quad (5.10)$$

whereby we can see why this process is called the internal conversion. Here

$$|\mathcal{M}_{\gamma^* \rightarrow l^+ l^-}|^2 = e^2 L^\mu (L^{\mu'})^* \quad (5.11)$$

and

$$|\mathcal{M}_{A \rightarrow B \gamma^*}|^2 = A_\mu (A_\mu)^*, \quad (5.12)$$

where

$$A_\mu = \epsilon^{\alpha\beta\gamma\mu} p_\alpha q_\beta \epsilon_\gamma e f_{AB}(M^2). \quad (5.13)$$

Using the decomposition 5.9 for the differential decay distribution we can write

$$\frac{d\Gamma_{A \rightarrow B l^+ l^-}}{dM^2} = \frac{\Gamma_{\gamma^* \rightarrow l^+ l^-}}{\pi M^4} \Gamma_{A \rightarrow B \gamma^*}, \quad (5.14)$$

where for the width of the internal conversion of the photon we find

$$\Gamma_{\gamma^* \rightarrow l^+ l^-} = \frac{2\alpha_{QED}}{3} \sqrt{1 - \frac{4m_l^2}{M^2}} (2m_l + M^2), \quad (5.15)$$

and

$$\Gamma_{A \rightarrow B \gamma^*} = \Gamma_{A \rightarrow B \gamma} |f_{AB}(M^2)|^2 \frac{[m_A^2 - (m_B + M)^2]^{3/2} [m_A^2 - (m_B - M)^2]^{3/2}}{(m_A^2 - m_B^2)^3} \quad (5.16)$$

is related to the decays where the photon is real. The normalized form factor for the $A \rightarrow B \gamma^*$ transition has a form

$$|f_{AB}(M^2)|^2 = \frac{m_\rho^4 + m_\rho^2 \Gamma_\rho^2}{(m_\rho^2 - M^2)^2 + m_\rho^2 \Gamma_\rho^2}. \quad (5.17)$$

It has the property $|f_{AB}(M^2)|^2 \rightarrow 1$ for $M \rightarrow 0$, for increasing M the form factor also increases. After putting all Eqs 5.14, 5.15, 5.16 and 5.17 together we arrive at the differential decay distribution which we will use to calculate the mass spectrum of dileptons from Dalitz decays. For more details see [106].

5.3 Model of the hydrodynamic expansion of the fire-cylinder

The description of medium effects on the dilepton production in heavy-ion collisions requires modeling of the time evolution of the collision system. The theoretical models can be divided into: transport models [92, 107], hydrodynamical approaches [103, 108, 102], and thermal fireball models [36, 26].

In this work our calculations are based on the fire cylinder hydrodynamic expansion model of Ref. [26, 27]. Lepton pairs are formed in a fire cylinder which undergoes a hydrodynamic expansion. The hadron-chemical analysis of a large body of hadronic heavy-ion data has shown that the final observed particle abundances at the SPS energies are consistent with a common chemical freezeout at temperatures of around 175 MeV and baryon chemical potentials of around 270 MeV. In the two-freezeout scenario, during the subsequent expansion and cooling the system continues to strongly interact via elastic collisions maintaining the thermal equilibrium until the thermal freezeout. The absence of pion-number changing reactions then induces a finite pion chemical potential. To incorporate these features, Rapp *et al.*, have proposed a simple expanding fireball model [26, 27]. This model assumes that the system is in thermal equilibrium up to time t_{max} , when the thermal freeze-out occurs. The velocity field characterizing the expansion depends on space-time coordinates in the following way:

$$\begin{aligned} v_{\parallel}(t, z) &= (v_z + a_z t) \frac{z}{z_{\text{max}}(t)}, \\ v_{\perp}(t, r) &= (v_r + a_r t) \frac{r}{r_{\text{max}}(t)}, \end{aligned} \quad (5.18)$$

where

$$\begin{aligned} z_{\text{max}}(t) &= z_0 + v_z t + \frac{1}{2} a_z t^2, \\ r_{\text{max}}(t) &= r_0 + v_r t + \frac{1}{2} a_r t^2, \end{aligned} \quad (5.19)$$

are the boundaries of the system at time t . We use the following parameters of expansion: $t_{\text{max}} = 11$ fm is fireball lifetime, $z_0 = 4.55$ fm is equivalent to formation time or initial temperature, $r_0 = 4.6$ fm corresponds to the initial transverse nuclear overlap radius, $v_r = 0$, and the parameters $v_z = 0.5$, $a_z = 0.023 \text{ fm}^{-1}$ and $a_r = 0.05 \text{ fm}^{-1}$ are adjusted to the final observed flow velocities. The time dependencies of the temperature and the baryon density are as follows

$$T(t) = (210 \text{ MeV}) \exp\left(-\frac{t}{18.26 \text{ fm}}\right), \quad (5.20)$$

$$\rho_B(t) = \frac{260}{V(t)}, \quad (5.21)$$

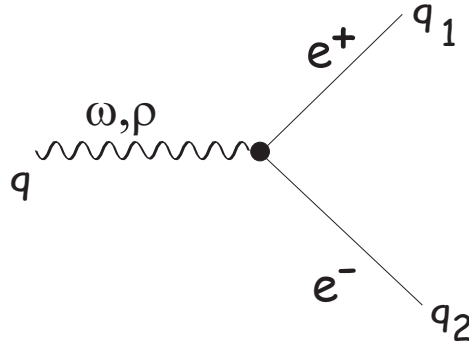


Figure 5.2: The assignment of momenta in the $\omega \rightarrow e^+e^-$ decay, where q is the incoming momentum of the ω or ρ meson, q_1 and q_2 are the outgoing momenta of the leptons

where 260 denotes the number of participating baryons, and

$$V(t) = 2\pi z_{\max}(t)r_{\max}^2(t), \quad (5.22)$$

is the volume of the fire-cylinder at time t .

For the time dependence of the pion chemical potential, $\mu(t)$, we assume, following Ref. [36], the linear rise from 20 MeV at $t = 0$ to 80 MeV at $t = t_{\max}$.

5.4 Kinematics for dilepton yield

Direct decays

A dominant source of dileptons in the low-mass region is the direct leptonic decays of vector mesons. Although we focus on Dalitz decays for dileptons of mass in the region of interest, one also considers the ρ^0 and ω mesons, see Fig. 5.2. The dilepton rate formula for the $\rho^0 \rightarrow e^+e^-$ decay is

$$\frac{dN^{e^+e^-}}{d^4x dM^2} = \int \frac{d^3q}{(2\pi^3)} \Gamma_{\rho \rightarrow e^+e^-} f_\rho(q \cdot u(x)) \frac{1}{\pi} \frac{3M\Gamma_\rho}{(m_\rho^2 - M^2)^2 + (M\Gamma_\rho)^2}, \quad (5.23)$$

where M is the invariant mass of the lepton pair, x is a space time point, and Γ_ρ is the total rho-meson width. The quantity $\Gamma_{\rho \rightarrow l^+l^-}$ is the decay width for $\rho^0 \rightarrow e^+e^-$,

$$\Gamma_{\rho \rightarrow l^+l^-} = \frac{4\pi\alpha_{QED}^2 m_\rho^4}{3g_\rho M^5} \left(1 - \frac{4m_l^2}{M^2}\right)^{1/2} (M^2 + 2m_l^2), \quad (5.24)$$

where α_{QED} denotes the fine structure constant, and m_l is the mass of the lepton. The function $f_\rho(q \cdot u)$ in Eq. 5.23 is the thermal Bose-Einstein distribution of the ρ mesons in the thermal model,

$$f_\rho(q \cdot u(x)) = \exp\left[-\left(\frac{q \cdot u(x) - 2\mu_\pi(x)}{T(x)}\right)\right], \quad (5.25)$$

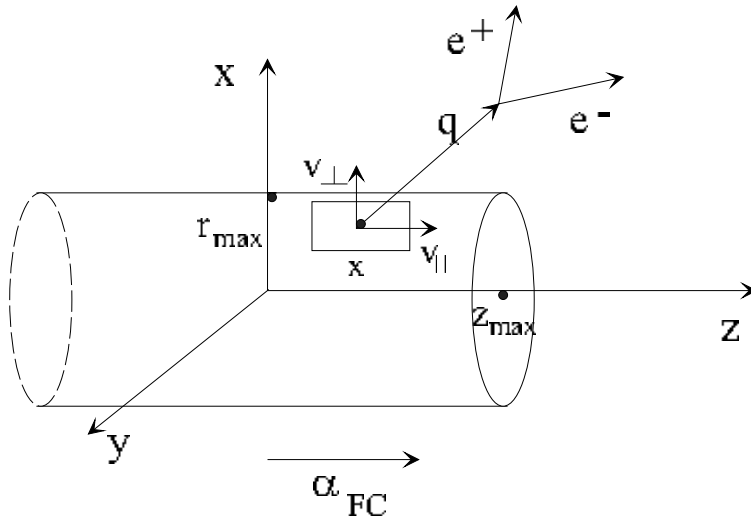


Figure 5.3: The hydrodynamic expansion of the cylinder moving in the lab system with rapidity α_{FC} in its own center-of-mass system. e^+, e^- are the leptons formed in a fire cylinder, whereas v_\perp, v_\parallel are the velocities, which depend on space-time, and z_{max} and r_{max} are the boundaries of the system at time t ; see section 4.3.

with the pion chemical potential μ_π .

Expansion of the fireball

To be as realistic as possible, we include the effects of the expansion of the medium formed in a relativistic heavy-ion collision, Fig 5.3. The lepton pairs are produced in a fire cylinder which moves in the lab system with rapidity α_{FC} . The fire cylinder expands hydrodynamically by itself. In particular, Eqs. 5.18 and 5.19 describe this expansion in the fire cylinder's center-of-mass system (CM). In such a case it is convenient to rewrite Eq. (5.23) in variables which are more convenient for the kinematics of the emission process and the geometry of the experiment. We introduce $M_\perp = \sqrt{M^2 + q_\perp^2}$, the transverse mass of the dilepton pair, y^{lab} , the rapidity of the pair measured in the lab system, \mathbf{u}_\perp , the transverse four-velocity of the fluid element producing dileptons, and α^{lab} , the rapidity of this fluid element in the lab. With these variables we have in the cylinder's rest frame

$$q \cdot u = M_\perp \sqrt{1 + u_\perp^2} \cosh(y^{lab} - \alpha^{lab}) - \mathbf{q}_\perp \cdot \mathbf{u}_\perp. \quad (5.26)$$

The velocity of the fluid element in the lab is a relativistic superposition of the velocity of the fire cylinder in the lab and the hydrodynamic flow considered in the CM system.

Thus we have

$$\alpha^{lab} = \alpha + \alpha_{FC} = \text{arctanh } v_{||} + \alpha_{FC}, \quad u_{\perp} = \frac{v_{\perp} \cosh(\alpha)}{\sqrt{1 - v_{\perp}^2 \cosh^2(\alpha)}}. \quad (5.27)$$

The velocities $v_{||}$ and v_{\perp} are now defined in the CM system and they depend on time and space coordinates.

Next, we analyze the kinematic constraint of the CERES experiment, see Appendix C. The experimental acceptance cuts can be included using the function

$$Acc(M, y^{lab}, q_{\perp}) = \frac{\int d^2 q_{1\perp} d^2 q_{2\perp} dy_1 dy_2 \phi \delta(E_q - E_{q_1} - E_{q_2}) \delta^{(3)}(\mathbf{q} - \mathbf{q}_1 - \mathbf{q}_2)}{\int d^2 q_{1\perp} d^2 q_{2\perp} dy_1 dy_2 \delta(E_q - E_{q_1} - E_{q_2}) \delta^{(3)}(\mathbf{q} - \mathbf{q}_1 - \mathbf{q}_2)}, \quad (5.28)$$

where $\mathbf{q}_{1,2}$ are the momenta of the emitted electrons, $y_{1,2}$ are the electron rapidities, and ϕ is a product of step functions which enforces the experimental setup conditions: $2.1 < y_{1,2} < 2.65$, $q_{1,2}^{\perp} > 200$ MeV, and $\theta_{ee} > 35$ mrad, where θ_{ee} is the angle between the directions of the leptons. We can assume that the rapidities and pseudorapidities of the electrons are equal because of the smallness of the electron mass. The construction of the function $Acc(M, y^{lab}, q_{\perp})$ requires numerical calculation of a two-dimensional integral of a function involving a product of step functions, which can be done by a Monte Carlo method. With the inclusion of the experimental acceptance cuts, the dilepton production rate is

$$\begin{aligned} \frac{dN^{e+e-}}{d^4x dM} &= 2M \int \frac{d^2 q_{\perp}}{(2\pi)^3} \int dy^{lab} Acc(M, y^{lab}, q_{\perp}) \times \\ &\times \frac{1}{\pi} \frac{3M\Gamma_{\rho}}{(m_{\rho}^2 - M^2)^2 + (M\Gamma_{\rho})^2} \Gamma_{\rho \rightarrow l^+ l^-} f_{\rho} \end{aligned} \quad (5.29)$$

To calculate the dilepton spectrum, we have to assume a model of the hydrodynamic expansion of the fire cylinder, as described in the previous subsection. Finally, the yield of dileptons produced during the expansion is

$$\frac{dN^{e+e-}}{dM} = \int_0^{t_{max}} dt \int_0^{r_{max}(t)} 2\pi r dr \int_{-z_{max}(t)}^{z_{max}(t)} dz \left(\frac{dN}{d^4x dM} \right), \quad (5.30)$$

where $\frac{dN}{d^4x dM}$ is given by Eq. (5.29) with elements defined in Eqs. 5.23, 5.25, 5.28. Similarly, we calculate the dilepton rate formula for the $\omega \rightarrow l^+ l^-$ decay.

Dalitz decays

In order to calculate the Dalitz decay $\omega \rightarrow \pi^0 e^+ e^-$, we choose the following kinematics, Fig 5.4: p_1 is the incoming momentum of the ω , q is the outgoing momentum of the

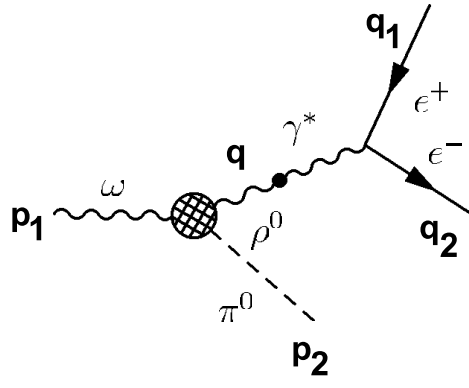


Figure 5.4: The assignment of momenta in the $\omega \rightarrow \pi^0 e^+ e^-$ decay, where p_1 is the incoming momentum of the ω , p_2 is outgoing momentum of the pion, and q is the outgoing momentum of the virtual photon. The outgoing momenta of the leptons are indicated by q_1 and q_2 .

virtual photon, and $p_2 = p_1 - q$ is the outgoing momentum of the pion, where $q^2 = M^2$, and M denotes the invariant mass of the lepton pair.

The particles are on the mass shell, hence $p_1^2 = m_\omega^2$, $p_2^2 = m_\pi^2$, and $p_1 \cdot q = \frac{1}{2}(m_\omega^2 + M^2 - m_\pi^2)$. In Fig. 5.4, q_1 and q_2 are the outgoing momenta of the leptons. The dilepton production rate from the Dalitz decays of the ω is given by the general formula

$$\frac{dN^{e^+e^-}}{d^4x} = \sum_{ss'} \sum_p \int dP_1 f_\omega(p_1 \cdot u) dP_2 [1 + f_\pi(p_2 \cdot u)] \int dQ_1 dQ_2 (2\pi)^4 \times \delta^{(4)}(p_1 - p_2 - q_1 - q_2) |\mathcal{M}^{(p)}|^2 \quad (5.31)$$

where x is a space-time point, $f_\omega(p_1 \cdot u)$ and $f_\pi(p_2 \cdot u)$ are the distribution functions for the ω meson and the pion, respectively, u is the four velocity of the medium, $dP_i = \frac{d^3 p_i}{(2\pi)^3 2E_{p_i}}$, $dQ_i = \frac{d^3 q_i m_i}{(2\pi)^3 E_{q_i}}$, $|\mathcal{M}|^2$ is the transition amplitude, $\sum_{ss'}$ is a sum over spins of the leptons, and \sum_p denotes the sum over the polarizations of the decaying meson. The amplitude for these processes has the invariant form

$$\mathcal{M}^{(p)} = A_{\gamma\sigma} \varepsilon_{(p)}^\gamma(p_1) G(q) \frac{em_\rho^2}{g_\rho} \frac{1}{q^2} e L^\sigma \quad (5.32)$$

where $A_{\gamma\sigma}$ is given by Eq.(2.29), ε^γ is the polarization vector of the ω , $G(q)$ is the denominator of the rho-meson propagator, $\frac{em_\rho^2}{g_\rho}$ is the conversion factor from the vector-dominance model, $\frac{1}{q^2}$ comes from the virtual photon propagator, and $L^\sigma = \bar{u}(q_1, s) \gamma^\sigma v(q_2, s')$, with u and v denoting the lepton spinors. We can write the amplitude in a more convenient notation

$$\mathcal{M}^{(p)} = \tilde{V}_\sigma^{(p)} \frac{e}{q^2} L^\sigma \quad (5.33)$$

where $\tilde{V}_\sigma^{(p)}$ is the $\omega\pi\gamma^*$ vertex, denoted as $\tilde{V}_\sigma^{(p)} = V_\sigma^{(p)} G(q) \frac{em_p^2}{g_\rho}$, and $V_\sigma^{(p)} = A_{\gamma\sigma} \varepsilon_{(p)}^\gamma(p_1)$ is the $\omega\rho\pi$ vertex. We obtain

$$|\mathcal{M}^{(p)}|^2 = \tilde{V}_\sigma^{(p)} \tilde{V}_{\sigma'}^{(p)*} \frac{e^2}{M^4} L^\sigma (L^{\sigma'})^*. \quad (5.34)$$

Now, we rewrite the dilepton-rate formula Eq. 5.31 as

$$\begin{aligned} \frac{dN^{e+e-}}{d^4x} &= \sum_s \int dQ_1 dQ_2 (2\pi)^4 \delta^{(4)}(q - q_1 - q_2) L^\sigma (L^{\sigma'})^* 4\pi\alpha_{e.m.} \times \\ &\sum_p \int d^4q \int dP_1 f_\omega(p_1 \cdot u) dP_2 [1 + f_\pi(p_2 \cdot u)] \delta^{(4)}(p_1 - p_2 - q) \tilde{V}_\sigma^{(p)} \tilde{V}_{\sigma'}^{(p)*} \frac{1}{M^4}, \end{aligned} \quad (5.35)$$

where $\alpha_{e.m.} = e^2/4\pi$ is the fine structure constant, $L^\sigma (L^{\sigma'})^*$ depends on q_1 and q_2 , $\tilde{V}_\sigma^{(p)} \tilde{V}_{\sigma'}^{(p)*}$ depends on p_1 and p_2 , and $M^2 = q^2$. First we compute the integral over dQ_1 and dQ_2 in the above expression. It has the form

$$S^{\sigma\sigma'} = -4\pi\alpha_{e.m.} \int dQ_1 dQ_2 (2\pi)^4 \delta^{(4)}(q - q_1 - q_2) L^\sigma (L^{\sigma'})^*, \quad (5.36)$$

where explicitly,

$$\begin{aligned} L^\sigma (L^{\sigma'})^* &= \bar{u}(q_1, s) \gamma^\sigma \mathbf{v}(q_2, s') \bar{\mathbf{v}}(q_2, s') \gamma^{\sigma'} u(q_1, s) = \\ Tr \left[\gamma^\sigma \frac{q_1 + m_l}{2m_l} \gamma^{\sigma'} \frac{q_2 - m_l}{2m_l} \right] &= \frac{1}{m_l^2} (q_1^\sigma q_2^{\sigma'} + q_1^{\sigma'} q_2^\sigma - g^{\sigma\sigma'} (q_1 \cdot q_2)) - g^{\sigma\sigma'}. \end{aligned} \quad (5.37)$$

In general, we can decompose the symmetric tensor $S^{\sigma\sigma'}$, which depends on the vector q , as

$$S^{\sigma\sigma'} = A Q^{\sigma\sigma'} + B \frac{q^\sigma q^{\sigma'}}{q^2}, \quad (5.38)$$

where $Q^{\sigma\sigma'}$ is a projection operator given by Eq. 2.57. However, due to gauge invariance, $B = 0$. Indeed, contracting $S^{\sigma\sigma'}$ with $q^\sigma q^{\sigma'}$ we find

$$\begin{aligned} S^{\sigma\sigma'} q_\sigma q_{\sigma'} 4\pi\alpha_{e.m.} \int dQ_1 dQ_2 (2\pi)^4 \delta^{(4)}(q - q_1 - q_2) \times \\ \left[\frac{1}{m_l^2} (2q_1 \cdot q q_2 \cdot q - q^2 q_1 \cdot q_2) - q^2 \right] &= B q^2. \end{aligned} \quad (5.39)$$

The term in square brackets is 0 due to the condition $q = q_1 + q_2$ and the lepton on the mass shell condition $q_1^2 = q_2^2 = m_l^2$; hence, as required by general principles, $B = 0$. To extract A we contract $S^{\sigma\sigma'}$ with $g_{\sigma\sigma'}$, obtaining

$$A = \frac{1}{3} S^{\sigma\sigma'} g_{\sigma\sigma'} = 4\pi\alpha_{e.m.} \int dQ_1 dQ_2 (2\pi)^4 \delta^{(4)}(q - q_1 - q_2) \frac{1}{3m_l^2} (M^2 + 2m_l^2) \quad (5.40)$$

The phase-space integral is most easily obtained in the rest frame of the decaying virtual photon of mass M . We get

$$\int dQ_1 dQ_2 (2\pi)^4 \delta^{(4)}(q - q_1 - q_2) = \frac{m_l^2}{2\pi} \left(1 - \frac{4m_l^2}{M^2}\right)^{\frac{1}{2}}, \quad (5.41)$$

and the partial decay width for the virtual photon is

$$\Gamma_{\gamma^* \rightarrow l^+ l^-} = \frac{A}{2M} = \frac{\alpha_{e.m.}}{3M} \left(1 - \frac{4m_l^2}{M^2}\right)^{\frac{1}{2}} (M^2 + 2m_l^2). \quad (5.42)$$

Thus

$$\begin{aligned} \frac{dN^{e+e-}}{d^4x} &= \sum_p \int d^4q \int dP_1 f_\omega(p_1 \cdot u) dP_2 [1 + f_\pi(p_2 \cdot u)] \\ &\times \delta^{(4)}(p_1 - p_2 - q) T^p(p_1, q) \frac{2}{M^3} \Gamma_{\gamma^* \rightarrow l^+ l^-}, \end{aligned} \quad (5.43)$$

where we have defined

$$T^p(p_1, q) = \tilde{V}_\sigma^{(p)} \tilde{V}_{\sigma'}^{(p)*} Q^{\sigma\sigma'}. \quad (5.44)$$

A useful form of the dilepton-rate formula can be obtained through the use of the identity

$$\int d^4q = \int d^4q \int dM^2 \delta(M^2 - q^2) = \int d^3q \int dM^2 \frac{1}{2E_q}. \quad (5.45)$$

We have

$$\begin{aligned} \frac{dN^{e+e-}}{d^4x dM^2} &= \sum_p \int \frac{d^3q}{2E_q} \int dP_1 f_\omega(p_1 \cdot u) dP_2 [1 + f_\pi(p_2 \cdot u)] \times \\ &\delta^{(4)}(p_1 - p_2 - q) \frac{2}{M^3} T^p(p_1, q) \Gamma_{\gamma^* \rightarrow l^+ l^-} = \sum_p \int dQ \int dP_1 f_\omega(p_1 \cdot u) \times \\ &dP_2 [1 + f_\pi(p_2 \cdot u)] (2\pi)^4 \delta^{(4)}(p_1 - p_2 - q) \frac{1}{\pi M^3} T^p(p_1, q) \Gamma_{\gamma^* \rightarrow l^+ l^-}. \end{aligned} \quad (5.46)$$

Explicitly, the quantity $T^p(p_1, q)$ is equal to

$$T^p(p_1, q) = A_{\gamma\sigma} \varepsilon_{(p)}^\gamma(p_1) A_{\gamma'\sigma'}^* \varepsilon_{(p)}^{*\gamma'}(p_1) Q^{\sigma\sigma'}(q) |F|^2. \quad (5.47)$$

The transversely polarized ω has two helicity states, with projection equal to ± 1 on the direction of q , while the longitudinally polarized ω has one helicity state, with the corresponding projection equal to 0. Taking this into account we find:

$$T^L(p_1, q) = L^{\gamma\gamma'} Q^{\sigma\sigma'} A_{\gamma\sigma} A_{\gamma'\sigma'}^*, \quad (5.48)$$

and

$$T^T(p_1, q) = T^{\gamma\gamma'} Q^{\sigma\sigma'} A_{\gamma\sigma} A_{\gamma'\sigma'}^*, \quad (5.49)$$

which we may rewrite as

$$\sum_p T^p(p_1, q) = (T_L + 2T_T) |F|^2, \quad (5.50)$$

where

$$|F|^2 = |G(q)|^2 \frac{4\pi\alpha_{e.m.}m_\rho^2}{g_\rho^2} = \frac{4\pi\alpha_{e.m.}}{g_\rho^2} \left(\frac{m_\rho^4}{(m_\rho^2 + M^2)^2 + M^2\Gamma_\rho^2} \right), \quad (5.51)$$

and Γ_ρ is the width of the ρ meson of virtual mass M . The width is dominated by the $\rho \rightarrow \pi\pi$ channel, hence $\Gamma_\rho = \frac{g_{\rho\pi\pi}^2}{48\pi M^2}(M^2 - 4m_\pi^2)^{\frac{3}{2}}$. Then we can write

$$\begin{aligned} \frac{dN^{e+e-}}{d^4x dM^2} &= \int \frac{d^3q}{(2\pi)^3 2E_q} \int \frac{d^3p_1}{(2\pi)^3 2E_{p_1}} f_\omega(p_1 \cdot u) \int \frac{d^3p_2}{(2\pi)^3 2E_{p_2}} (2\pi)^4 \times \\ &[1 + f_\pi(p_2 \cdot u)] \delta(E_{p_1} - E_{p_2} - E_q) \delta^{(3)}(\vec{p}_1 - \vec{p}_2 - \vec{q}) \times \\ &(T_L + 2T_T) |F|^2 \frac{1}{\pi M^3} \Gamma_{\gamma^* \rightarrow l+l^-}. \end{aligned} \quad (5.52)$$

The distribution functions have the thermal form $f_\omega = f_\omega(p_1 \cdot u) = \exp[-(p_1 \cdot u)/T(t)]$ and $f_\pi = [1 + f_\pi(p_2 \cdot u)] = 1 + \exp[-(p_2 \cdot u)/T(t)]$, where $(p_1 \cdot u) = E_{p_1}u_0 - p_{1\parallel}u_\parallel - p_{1\perp}u_\perp(\cos\alpha \cos\theta - \sin\alpha \sin\theta)$, and $u_0 = \sqrt{1 + u_\perp^2 + u_\parallel^2}$. Integrating our expression over the p_2 momentum and substituting d^3q as $q_\perp dq_\perp dq_\parallel d\alpha$ and d^3p_1 as $p_{1\perp} dp_{1\perp} dp_{1\parallel} d\theta$, where the angle α is between \vec{q}_\perp and \vec{u}_\perp , and θ between $\vec{p}_{1\perp}$ and \vec{q}_\perp , we obtain

$$\begin{aligned} \frac{dN^{e+e-}}{d^4x dM^2} &= \int \frac{q_\perp dq_\perp dq_\parallel d\alpha}{(2\pi)^3 2E_q} \int \frac{p_{1\perp} dp_{1\perp} dp_{1\parallel} d\theta}{(2\pi)^3 2E_{p_1}} f_\omega f_\pi \frac{\pi}{E_{p_2}} \times \\ &\delta(E_{p_1} - E_{p_2} - E_q) (T_L + 2T_T) |F|^2 \frac{1}{\pi M^3} \Gamma_{\gamma^* \rightarrow l+l^-}. \end{aligned} \quad (5.53)$$

The on-mass-shell conditions are

$$\begin{aligned} E_{p_1} &= \sqrt{m_\omega^2 + p_{1\perp}^2 + p_{1\parallel}^2}, \\ E_{p_2} &= \sqrt{m_\pi^2 + p_2^2} = \sqrt{m_\pi^2 + (\vec{p}_1 + \vec{q})^2} = \sqrt{m_\pi^2 + (p_{1\parallel} - q_\parallel)^2 + p_{1\perp}^2 + q_\perp^2 - 2p_{1\perp}q_\perp \cos\theta}, \\ E_q &= \sqrt{M^2 + q_\perp^2 + q_\parallel^2}. \end{aligned} \quad (5.54)$$

Thanks to energy conservation we can eliminate integration over the angle θ , from the Dirac delta in Eq. 5.53. We get $\delta(\theta - \theta_0)$, where

$$\cos\theta_0 = \frac{-(M^2 + m_\omega^2 - m_\pi^2 + 2p_{1\parallel}q_\parallel - 2\sqrt{m_\omega^2 + p_{1\parallel}^2 + p_{1\perp}^2}\sqrt{M^2 + q_\parallel^2 + q_\perp^2})}{2p_{1\perp}q_\perp}. \quad (5.55)$$

We have to remember that $\cos\theta_0$ must be in the range $[-1, 1]$. For dilepton production from ω -meson decays we can write:

$$\frac{dN^{e+e-}}{d^4x dM^2} = \int \frac{\pi dq_\perp dq_\parallel d\alpha}{(2\pi)^3 2E_q} \frac{dp_{1\perp} dp_{1\parallel}}{(2\pi)^3 2E_{p_1}} f_\omega f_\pi \frac{2 \Theta(1 - |\cos\theta_0|)}{|\sin\theta_0|} \frac{1}{\pi M^3} (T_L + 2T_T) |F|^2 \Gamma_{\gamma^* \rightarrow l+l^-}, \quad (5.56)$$

where the factor 2 in the numerator comes from the two solutions of the equation $\cos\theta = \cos\theta_0$.

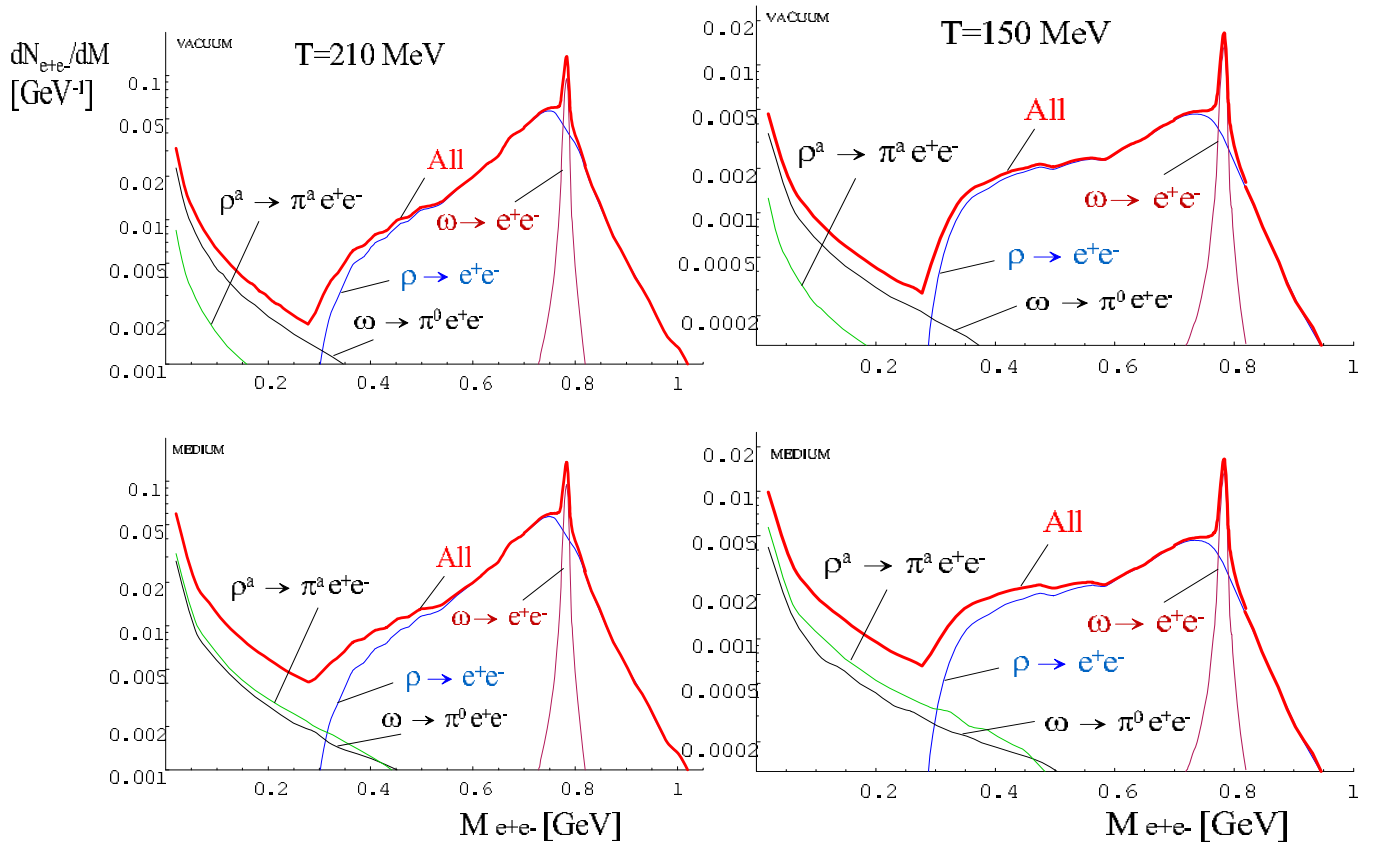


Figure 5.5: The dilepton yield for the direct decays $\omega \rightarrow e^+e^-$ and $\rho \rightarrow e^+e^-$, and the Dalitz decays $\omega \rightarrow \pi^0 e^+e^-$ and $\rho^a \rightarrow \pi^a e^+e^-$, plotted as a function of the invariant mass, $M_{e^+e^-}$. The two upper plots are for the vacuum value of the coupling constant; lower plots include the medium-modified $\pi\omega\rho$ vertex. We show our results for two different temperatures, $T = 210$ MeV (left), from Ref. [26] and $T = 150$ MeV (right), [109]. The thick line indicates the sum of all contributions.

Next, we apply the experimental acceptance cuts, which are included in the function

$$Acc(M, q_{\parallel}, q_{\perp}) = \frac{\int d^2q_{1\perp} d^2q_{2\perp} dq_{1\parallel} dq_{2\parallel} \frac{1}{E_{q1}E_{q2}} \phi \delta(E_q - E_{q1} - E_{q2}) \delta^{(3)}(\mathbf{q} - \mathbf{q}_1 - \mathbf{q}_2)}{\int d^2q_{1\perp} d^2q_{2\perp} dq_{1\parallel} dq_{2\parallel} \frac{1}{E_{q1}E_{q2}} \delta(E_q - E_{q1} - E_{q2}) \delta^{(3)}(\mathbf{q} - \mathbf{q}_1 - \mathbf{q}_2)}, \quad (5.57)$$

where the electron rapidities, see eq. 5.28, were rewritten as $dy = dq_{\parallel}/E_q$, with $E_q = \sqrt{M^2 + q_{\perp}^2 + q_{\parallel}^2}$. Finally, after using the fire-cylinder hydrodynamic expansion model of [26, 27] described in sec. 4.3, the yield of dileptons produced during the expansion is (the Bose enhancement is neglected for brevity)

$$\frac{dN^{e^+e^-}}{dM^2} = \int_0^{t_{\max}} dt \int_0^{r_{\max}(t)} 2\pi r dr \int_{-z_{\max}(t)}^{z_{\max}(t)} dz \left(\frac{dN^{e^+e^-}}{d^4x dM^2} Acc(M, q_{\parallel}, q_{\perp}) \right). \quad (5.58)$$

In the case of the Dalitz decay of the ρ meson we apply the same formulas.

Chapter 6

Results of our model

In the following we present our numerical results. We begin with calculations without expansion of the fire-cylinder and without the acceptance cuts, Eqs. 5.28 and 5.57, shown in Fig. 5.5. We do this in case to compare with other works. New and important result of this study is to applying in our calculations the CERES experimental kinematic cuts, what in other theoretical works is usually skipped.

In Fig. 5.5 we plot the dilepton yield as a function of the invariant mass, $M_{e^+e^-}$. On the left-hand side we show the results for the temperature of 210 MeV of Ref. [26]; see section 4.3. The upper plot is for the vacuum value of the $\pi\omega\rho$ coupling constant. We display the direct contributions, such as $\omega \rightarrow e^+e^-$ and $\rho \rightarrow e^+e^-$, which are indicated by pink and blue curves, and the Dalitz contributions of both ω (black curve) and ρ (green curve) mesons. On the lower plot we present the same results but with medium modified $\pi\omega\rho$ vertex. The thick red line indicates the sum of all direct and Dalitz contributions. We see that the Dalitz decays are enhanced by about a factor of 2 compared to the vacuum values. On the right-hand side we show the results for a lower temperature of 150 MeV, with similar conclusions. It is visible that the direct decays are dominant in the region above 0.35 GeV and that the number of produced particles increases with growing temperature. Here we also observe the peak from the direct decay of the omega meson, which is not observed in the data because of the too low experimental resolution.

Next, we include in our calculations the expansion effects and the CERES acceptance function. In Fig. 6.1 we illustrate the dilepton yield for the $\omega \rightarrow \pi^0 e^+ e^-$ (left-hand side) and $\rho^a \rightarrow \pi^a e^+ e^-$ (right-hand side) decays, plotted as a function of the invariant mass of dileptons, $M_{e^+e^-}$. The plots are done for the maximum fireball temperature of 210 MeV and for different values of the baryon density, $\rho_B(t)$ (green dotted curve) and $2 \rho_B(t)$ (red curve). In our calculations we use the Rapp-Wambach

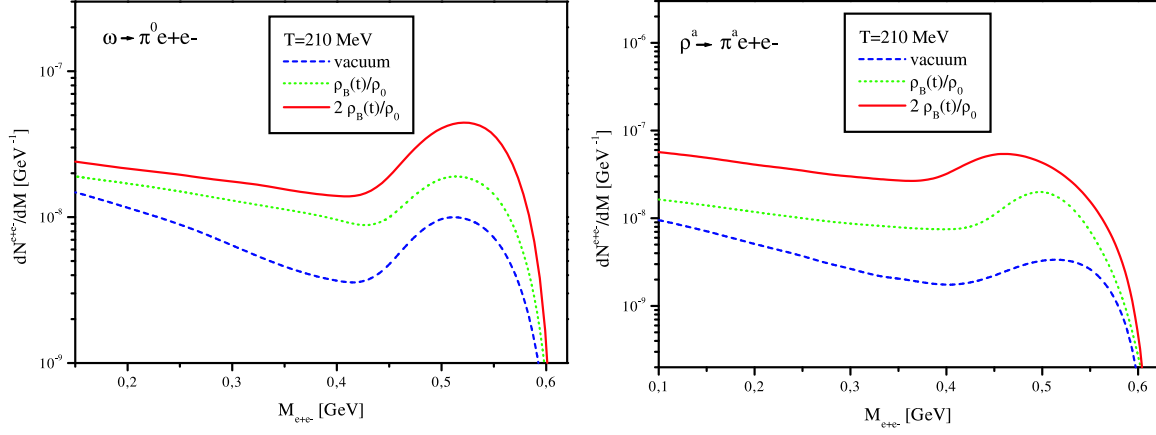


Figure 6.1: The dilepton yield for the Dalitz decays. The dashed lines are for the vacuum value of coupling constant, whereas the solid lines include the medium modified $\pi\omega\rho$ vertex. Green and red lines show the results for different value of baryon density $\rho_B(t)$ and $2\rho_B(t)$, respectively. We show our results for $T = 210$ MeV.

model of the fireball, but we change the temperature from $T=210$ to $T=300$ and increase two times the baryon density. This significantly enhances the medium effects. By the blue dashed line we indicate the case with the vacuum value of the $\pi\omega\rho$ vertex. We can observe that the medium effects from the Dalitz decays of vector mesons are clearly visible, over the entire region of $M_{e^+e^-} = 0.2 - 0.6$ GeV. For both Dalitz decays $\omega \rightarrow \pi^0 e^+ e^-$ and $\rho^a \rightarrow \pi^a e^+ e^-$ there is a difference of about a factor of 2 for the case with normal baryon density compared to the vacuum value. Simultaneously, we notice that this enhancement factor rises to a higher value of about a factor of 5 with the growing fireball density.

We have a similar situation in Fig. 6.2, where the same results as in Fig. 6.1, but for temperatures of 300 MeV, are presented. The dilepton production from Dalitz decays is found to be strongly enhanced for the medium-modified vertex compared to the vacuum for this value of the temperature. This difference grows even larger, to about one order of magnitude, with the growing baryon density. It is naturally explained since we expect to observe more particles produced at higher temperatures than at lower ones.

We continue our discussion with Fig. 6.3 and 6.4, where we present the dilepton spectra from the direct and Dalitz decays compared to the CERES experimental data, taken from Ref. [89], for two different temperatures, $T=210$ MeV and $T=300$ MeV. Both plots are for the same density equal to twice the normal baryon density. As we can see the medium modifications help, but not enough to reproduce the experimental

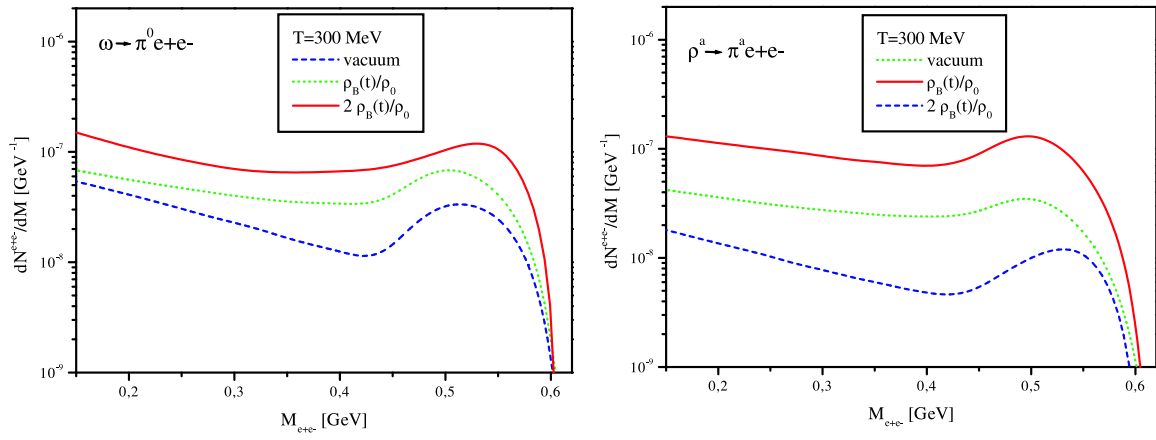


Figure 6.2: Same as Fig. 6.1, but for the $T = 300$ MeV. Left side, the dilepton yield for the Dalitz decay $\omega \rightarrow \pi^0 e^+ e^-$; right side, for $\rho^a \rightarrow \pi^a e^+ e^-$, plotted as a function of the, $M_{e^+e^-}$. Dashed lines correspond to the vacuum value of the coupling constant, solid lines include medium modified $\pi\omega\rho$ vertex. Green and red lines show the results for different values of the baryon density $\rho_B(t)$ and $2 \rho_B(t)$, respectively.

data. However, for the higher temperature of the fireball, $T=300$ MeV, results lie much closer to the data. We notice that the medium effects from Dalitz decays of the ω and ρ mesons are large and are specifically about two times larger than in vacuum. We see that the contributions from the $\rho^a \rightarrow \pi^a e^+ e^-$ decay are equally important as the ones from the Dalitz decay of the ω meson and should not be neglected during the considerations connected with the low-mass dilepton spectrum, as is frequently done. It is visible from our analysis that in the region of interest, $0.2 - 0.6$ GeV, where the existing calculations have problems explaining the experimental data, our effect helps but still fails to reproduce the experimental data.

We have to admit that there are other processes which contribute in the explored region of $M_{e^+e^-}$, like Dalitz decays of η and η' mesons which we do not include in our calculation. We have not taken into account other effects such as shift of the ρ meson peak position or broadening of the widths. We also do not show the 'cocktail' contribution of decays of hadrons on top of our results, which would not be consistent.

After all, we stress that the $\pi\omega\rho$ coupling constant undergo substantial modification in the nuclear medium and directly influence the dilepton production rate, to which this thesis was devoted.

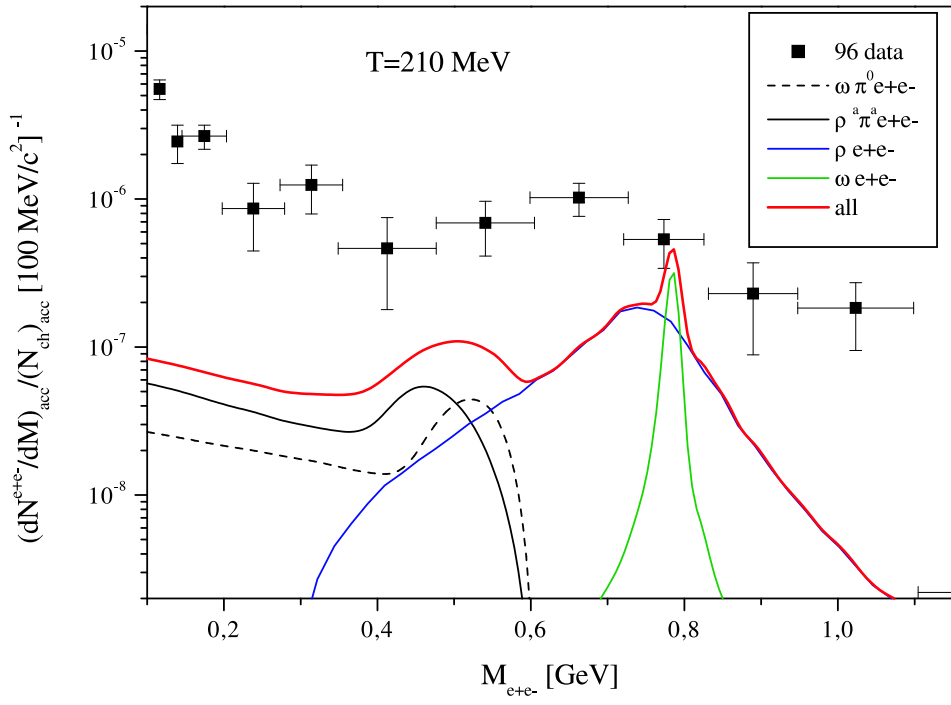


Figure 6.3: Dilepton emission rate for 158 AGeV Pb+Au CERES experiment from the Dalitz and direct decays (for $p_{\perp} > 0.2$ GeV). The dashed and solid line correspond to the $\omega \rightarrow \pi^0 e^+ e^-$ and $\rho^a \rightarrow \pi^a e^+ e^-$ decays, respectively. The solid blue and green line correspond to direct contributions $\rho \rightarrow e^+ e^-$ and $\omega \rightarrow e^+ e^-$. We show our results for temperature $T = 210$ MeV and double normal value of the baryon density.

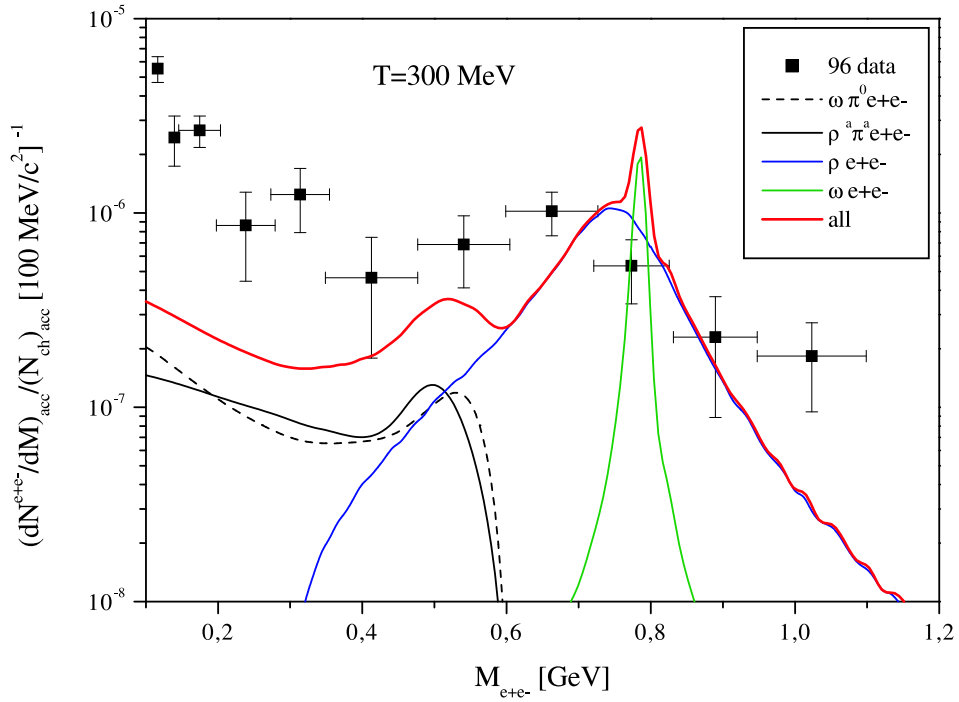


Figure 6.4: Same as Fig. 6.3 but for $T = 300$ MeV.

Chapter 7

Summary and discussion

In this thesis we have considered the modifications of the $\pi\omega\rho$ coupling in dense nuclear matter and its influence on dilepton spectra in relativistic heavy-ion collisions coming from the Dalitz decays.

In the first part we have analyzed the $\pi\omega\rho$ vertex in the context of the Dalitz decays of π^0 , ω and ρ particles. Our calculations were done in the framework of a fully relativistic hadronic theory with mesons, nucleons and Δ isobars. We have presented diagrams, propagators, typical vertices for the interactions with and without Δ resonance, and the in-medium tensor structure of the $\pi\omega\rho$ coupling constant. Presence of the additional four-vector, the four-velocity of the medium, made this structure more complicated. We have worked at zero temperature and in the leading-density approximation. We have considered decays of particles in the rest and the moving frame with respect to the medium.

In the case where the decaying particles are moving with respect to the medium we have analyzed the kinematics in a convenient way, in the rest frame of the nuclear matter, not in the rest frame of decaying particle, as it frequently done in the vacuum calculations. Because each polarization of the decaying particles behaves differently the properties of these particles are different, in particular their widths. Thus, we have analyzed the dependence of the widths for transverse and longitudinal polarizations on the invariant mass of dileptons.

The main conclusion of our investigation is that the medium effects on the $\pi\omega\rho$ coupling are large and primarily come from the process where the Δ is excited in the intermediate state. On the other hand, for the $\pi^0 \rightarrow \gamma\gamma^*$ decay the effects of the Δ isobar cancel almost exactly the nucleon particle-hole excitation, such that the medium contribution is small. The dilepton yield from the π^0 decays are not changed by the medium, because virtually all pions, due to their long lifetime, decay

outside the fireball and because the width for this decay is practically unaltered by the nuclear matter. However, we have found a sizeable increase of the $\pi\omega\rho$ vertex compared to its vacuum value for the Dalitz decays from ω and ρ mesons. This coupling constant is enhanced by about a factor of 2 for the $\omega \rightarrow \pi^0\gamma^*$ decay and by a factor of 5 for the $\rho^a \rightarrow \pi^a\gamma^*$ decay. For the decaying particle moving with respect to the nuclear matter, the medium effects decrease with growing magnitude of three momentum, but remain significant for a momenta up to ~ 200 MeV, the relevant value for temperatures typical in heavy-ion collisions. This results confirm that the medium effects are substantial.

Through-out our calculations we were following a relativistic covariant approach. We have also shown in detail how to obtain the leading-density approximation for dileptons involving loops with density-dependent nucleon propagators. In order to simplify our approach we have not included any form factors in the vertices, because they lead to fundamental problems with gauge symmetry conservation, in particular the Ward-Takahashi identities and current conservation are violated. We have considered the Dalitz decay of the ρ meson which was never analyzed before.

In the second part we have applied our model to evaluate the dilepton production rate from the Dalitz decays of vector mesons in relativistic heavy ion collisions. In order to estimate the dilepton yields we have used the VDM and including expansion of the medium. In our calculations we have adopted the Rapp-Wambach model of the hydrodynamic expansion of the fire-cylinder, which includes longitudinal and transverse expansion. The kinematic constraints of the CERES experiment also is used. The construction of the acceptance function required a numerical calculation of a two-dimensional integral involving the product of step functions, which we have obtained by a Monte Carlo method.

In order to compare our results with other works, we have shown the dilepton yield as a function of the invariant mass for calculations without expansion of the fire-cylinder and without the acceptance cuts. We have presented plots for two temperatures, 210 MeV and 150 MeV, with conclusions that the Dalitz decays are enhanced by about a factor of 2 compared to the vacuum and that the number of particles increases with temperature. On the other hand, the direct decays are dominant in the region around 0.4 GeV.

Next, we have included the expansion and the CERES acceptance function. Our final plots are done for two fireball temperatures ($T = 210$ MeV and $T = 300$ MeV) and for density equal to twice of the normal baryon density. Comparing our results to the dilepton invariant mass spectrum measured by the CERES collaboration at

CERN SPS we have found that the Dalitz decays are enhanced in the region of $0.2 - 0.6$ GeV, and medium modifications of coupling constant increase the effect. It is worth pointing out that the contribution from Dalitz decay of the ρ meson is equally important as the ω . However our results still underestimate the experimental data.

Our model together with other effects, which are not considered here, such as creation of dileptons from other decays (η and η'), dropping masses or broadening widths, may be able to explain the present experimental data. The other effects should be taken into account in future work.

For our numerical analysis we have developed a program written in 'Mathematica' with the very useful FeynCalc package for algebraic calculation in elementary particle physics. We have included in the Mathematica code the acceptance function, which was calculated in Fortran.

The low-mass dilepton research is a quickly evaluating branch of theoretical and experimental physics. Inclusion of more sources of dileptons or detailed verifications of existed theoretical models, together with new experimental data will provide new insight into that relevant problem in relativistic heavy-ion collisions physics.

Chapter 8

Appendices

8.1 Appendix A

The contributions to B from diagrams (a), (b) and (c) of Fig. 2.3 for the process $\pi^0 \rightarrow \gamma(\omega)\gamma^*$ are as follows:

$$\begin{aligned}
B_{(a)}^{\pi^0(\omega)} &= \frac{m_N(\kappa_\rho + 1)g_A g_\rho g_\omega m_\pi^2(3x^2 + m_\pi^2)}{(4m_N^2 - m_\pi^2)((m_N x^2 + m_N m_\pi^2)^2 - x^4 m_\pi^2)}, \\
B_{(b)}^{\pi^0(\omega)} &= -\frac{g_{N\Delta\pi} g_{N\Delta\rho} g_\omega F_\pi m_\pi}{9M_\Delta^2 m_N [(m_N x^2 + m_N m_\pi^2)^2 - (m_N^2 - M_\Delta^2 + x^2)^2 m_\pi^2]} ((m_N^2 - M_\Delta^2) \times \\
&\quad (m_N^2 + m_N M_\Delta - M_\Delta^2 + x^2) m_\pi^2 - (m_N x^2 (m_N^3 - m_N M_\Delta^2 M_\Delta x^2)) - m_N^2 m_\pi^4), \\
B_{(c)}^{\pi^0(\omega)} &= -\frac{g_{N\Delta\pi} g_{N\Delta\rho} g_\omega F_\pi}{27M_\Delta^4 m_\pi [(m_N^2 - M_\Delta^2 + x^2)^2 m_\pi^2 - (m_N m_\pi^2 + m_N x^2)^2]} (- (m_N^2 (2m_N + \\
&\quad + 3M_\Delta) x^6) + x^2 (4m_N^5 + 6m_N^4 M_\Delta - 8m_N^3 x^2 + 3m_N^2 (M_\Delta^3 - 3M_\Delta x^2) + \\
&\quad + 2m_N (4M_\Delta^4 - 2M_\Delta^2 x^2 + x^4) + 3M_\Delta (M_\Delta^4 - 3M_\Delta^2 x^2 + 2x^4)) m_\pi^2 + (4m_N^5 + \\
&\quad + 6m_N^4 M_\Delta + 11M_\Delta^5 - 17M_\Delta^3 x^2 + 6M_\Delta x^4 - 2m_N^3 (4M_\Delta^2 + x^2) - m_N^2 (5M_\Delta^3 + \\
&\quad + 9M_\Delta x^2) + 4m_N (4M_\Delta^4 - 5M_\Delta^2 x^2 + 2x^4)) m_\pi^4 - m_N (4m_N^2 + 3m_N M_\Delta + \\
&\quad + 2x^2) m_\pi^6),
\end{aligned} \tag{8.1}$$

where $x = m_\omega$

The contributions to B from $\pi^0 \rightarrow \gamma(\rho)\gamma^*$ decay are as follows:

$$\begin{aligned}
B_{(a)}^{\pi^0(\rho)} &= \frac{g_A g_\rho g_\omega m_\pi^2 (2m_N^2 x^2 (3 + \kappa_\rho) + (x^2 \kappa_\rho + 2m_N^2 (1 + \kappa_\rho)) m_\pi^2)}{2m_N (4m_N^2 - m_\pi^2) ((m_N x^2 + m_N m_\pi^2)^2 - x^4 m_\pi^2)}, \\
B_{(b)}^{\pi^0(\rho)} &= \frac{g_{N\Delta\pi} g_{N\Delta\rho} g_\omega F_\pi m_\pi (x^2 - m_\pi^2) (m_N^2 x^4 (m_N^3 - 2M x^2 - m_N (M_\Delta^2 + 2x^2)) + x^2}{9M_\Delta^2 ((M_\Delta^2 - m_N^2)^2 m_\pi^2 - (m_N x^2 - m_N m_\pi^2)^2) ((m_N x^2 + m_N m_\pi^2)^2 - x^4 m_\pi^2)} \times \\
&\quad (4m_N^5 + m_N^4 M_\Delta + 3m_N M_\Delta^4 + 2M_\Delta^5 + m_N^3 (-7M_\Delta^2 + 6x^2) - 3m_N^2 (M_\Delta^3 - \\
&\quad - M_\Delta x^2)) m_\pi^2 - m_N (m_N^4 + m_N^3 M_\Delta + M_\Delta^4 + m_N^2 (-2M_\Delta^2 + 5x^2) + \\
&\quad + m_N (-M_\Delta^3 + M_\Delta x^2)) m_\pi^4 + m_N^3 m_\pi^6), \\
B_{(c)}^{\pi^0(\rho)} &= \frac{g_{N\Delta\pi} g_{N\Delta\rho} g_\omega F_\pi (- (m_N^2 (2m_N + 3M_\Delta) x^6) + x^2 (4m_N^5 + 6m_N^4 M + 8m_N M_\Delta^4)}{27M_\Delta^4 m_\pi ((M_\Delta^2 - m_N^2)^2 m_\pi^2 - (m_N x^2 - m_N m_\pi^2)^2)} + \\
&\quad + 3M_\Delta^5 + 8m_N^3 x^2 + 3m_N^2 (M_\Delta^3 + 3M_\Delta x^2)) m_\pi^2 - (4m_N^5 + 6m_N^4 M_\Delta + \\
&\quad + 16m_N M_\Delta^4 + 11M_\Delta^5 - 2m_N^3 (4M_\Delta^2 - 5x^2) + m_N^2 (-5M_\Delta^3 + 9M_\Delta x^2)) m_\pi^4 + \\
&\quad + m_N^2 (4m_N + 3M_\Delta) m_\pi^6)
\end{aligned} \tag{8.2}$$

with $x = m_\rho$.

8.2 Appendix B

Numerators and denominators of Eq. 2.33

For the case $\mathbf{q} = \mathbf{0}$ the contributions to B from Eq.2.33 corresponding to the diagrams (a,b,c) from Fig.2.3, can be written as

$$A_{(i)}^{\mu\nu} = \frac{i}{F_\pi} \frac{e^2}{g_\rho g_\omega} \left(g_{\pi\rho\omega} + \rho_B \frac{N_{(i)}}{D_{(i)}} \right) \epsilon^{\nu\mu p Q}, \tag{8.3}$$

The formulas for $N_{(i)}$ and $D_{(i)}$ are very long. Numerators $N_{(i)}$ become manageable in the formal case $\Gamma_\Delta = 0$. Below we show the numerators for the diagrams with nucleons only, because those with Δ isobar are too long. We find

$$\begin{aligned}
N_{(a)}^\omega &= g_A g_\rho g_\omega (m_N^2 \kappa_\rho m_\pi^8 (m_N^2 - m_\omega^2) + 2m_N^2 m_\pi^6 (-2m_N^2 x^2 \kappa_\rho + (x^2 \kappa_\rho - 3m_N^2 \times \\
&\quad \times (1 + \kappa_\rho)) m_\omega^2 + \kappa_\rho m_\omega^4) - m_N^2 (x^2 - m_\omega^2)^2 (- (m_N^2 x^4 \kappa_\rho) + x^2 (x^2 \kappa_\rho + \\
&\quad + m_N^2 (6 + 4\kappa_\rho)) m_\omega^2 + m_N^2 (2 + \kappa_\rho) m_\omega^4) + m_\pi^4 (6m_N^4 x^4 \kappa_\rho + 2m_N^2 x^2 (- (x^2 \kappa_\rho) + \\
&\quad + 3m_N^2 (1 + \kappa_\rho)) m_\omega^2 + (2m_N^2 x^2 + x^4 \kappa_\rho + 2m_N^4 (5 + 4\kappa_\rho)) m_\omega^4 - m_N^2 \kappa_\rho m_\omega^6) - \\
&\quad - 2m_N^2 m_\pi^2 (2m_N^2 x^6 \kappa_\rho - x^4 (x^2 \kappa_\rho + 3m_N^2 (1 + \kappa_\rho)) m_\omega^2 + x^2 (-x^2 + 2m_N^2 (5 + \\
&\quad + 4\kappa_\rho)) m_\omega^4 + (m_N^2 - x^2) (1 + \kappa_\rho) m_\omega^6)),
\end{aligned}$$

$$\begin{aligned}
N_{(a)}^\rho = & -(g_A g_\rho g_\omega m_\rho^2 (6m_N^4 (1 + \kappa_\rho) m_\pi^6 + m_N^2 (x^2 - m_\rho^2)^2 (2m_N^2 x^2 (3 + \kappa_\rho) + (x^2 \kappa_\rho + \\
& + 2m_N^2 (1 + \kappa_\rho)) m_\rho^2) - m_\pi^4 (2m_N^4 x^2 (3 + 5\kappa_\rho) + m_N^2 (x^2 (2 - 3\kappa_\rho) + 10m_N^2 \times \\
& \times (1 + \kappa_\rho)) m_\rho^2 + x^2 \kappa_\rho m_\rho^4) + 2m_N^2 m_\pi^2 (m_N^2 x^4 (-3 + \kappa_\rho) - x^2 (x^2 (1 + \\
& + 2\kappa_\rho) - 2m_N^2 (5 + 3\kappa_\rho)) m_\rho^2 + (-x^2 + m_N^2 (1 + \kappa_\rho)) m_\rho^4)). \tag{8.4}
\end{aligned}$$

The expressions for D_i for the case $\Gamma_\Delta = 0$ for $\omega \rightarrow \pi^0 \gamma^*$ decay, where $x = m_\rho$, are

$$\begin{aligned}
D_{(a)}^\omega = & 2(2m_N - m_\omega)(2m_N + m_\omega)(m_N x^2 - m_N m_\pi^2 - x^2 m_\omega + m_N m_\omega^2)(m_N x^2 - \\
& - m_N m_\pi^2 + x^2 m_\omega + m_N m_\omega^2)(m_\pi^2 (m_N - m_\omega) + m_N (-x^2 + m_\omega^2)) \times \\
& \times (m_\pi^2 (m_N + m_\omega) + m_N (-x^2 + m_\omega^2)), \\
D_{(b)}^\omega = & 9M_\Delta^2 m_\omega (-(m_N x^2) + m_N m_\pi^2 + (m_N^2 - M_\Delta^2 + x^2) m_\omega - m_N m_\omega^2)(m_N x^2 - \\
& - m_N m_\pi^2 + (m_N^2 - M_\Delta^2 + x^2) m_\omega + m_N m_\omega^2)(m_N x^2 + (m_N^2 - M_\Delta^2) m_\omega - m_N \times \\
& \times m_\omega^2 + m_\pi^2 (-m_N + m_\omega)) (-(m_N x^2) + (m_N^2 - M_\Delta^2) m_\omega + m_N m_\omega^2 + \\
& + m_\pi^2 (m_N + m_\omega)), \\
D_{(c)}^\omega = & 27M_\Delta^4 m_\omega (-(m_N x^2) + m_N m_\pi^2 + (m_N^2 - M_\Delta^2 + x^2) m_\omega - m_N m_\omega^2)(m_N x^2 - \\
& - m_N m_\pi^2 + (m_N^2 - M_\Delta^2 + x^2) m_\omega + m_N m_\omega^2)(m_N x^2 + (m_N^2 - M_\Delta^2) m_\omega - \\
& - m_N m_\omega^2 + m_\pi^2 (-m_N + m_\omega)) (-(m_N x^2) + (m_N^2 - M_\Delta^2) m_\omega + m_N m_\omega^2 + \\
& + m_\pi^2 (m_N + m_\omega)) \tag{8.5}
\end{aligned}$$

The expressions for D_i for the case $\Gamma_\Delta = 0$ are for the $\rho \rightarrow \pi^0 \gamma^*$ decay, where $x = m_\omega$

$$\begin{aligned}
D_{(a)}^\rho = & 2(2m_N - m_\rho)(2m_N + m_\rho)(m_N x^2 - m_N m_\pi^2 - x^2 m_\rho + m_N m_\rho^2)(m_N x^2 - \\
& - m_N m_\pi^2 + x^2 m_\rho + m_N m_\rho^2)(m_\pi^2 (m_N - m_\rho) + m_N (-x^2 + m_\rho^2)) \times \\
& \times (m_\pi^2 (m_N + m_\rho) + m_N (-x^2 + m_\rho^2)), \\
D_{(b)}^\rho = & 9M_\Delta^2 (m_N + M_\Delta - m_\rho)(m_N + M_\Delta + m_\rho)(m_N x^2 - m_N m_\pi^2 - x^2 m_\rho + \\
& + m_N m_\rho^2)(m_N x^2 - m_N m_\pi^2 + x^2 m_\rho + m_N m_\rho^2)(m_N x^2 + (m_N^2 - M_\Delta^2) m_\rho - \\
& - m_N m_\rho^2 + m_\pi^2 (-m_N + m_\rho)) (-(m_N x^2) + (m_N^2 - M_\Delta^2) m_\rho + m_N m_\rho^2 + \\
& + m_\pi^2 (m_N + m_\rho)), \\
D_{(c)}^\rho = & 27M_\Delta^4 (m_N + M_\Delta - m_\rho) m_\rho (m_N + M_\Delta + m_\rho)(m_N x^2 + (m_N^2 - M_\Delta^2) m_\rho - \\
& - m_N m_\rho^2 + m_\pi^2 (-m_N + m_\rho)) (-(m_N x^2) + (m_N^2 - M_\Delta^2) m_\rho + m_N m_\rho^2 + \\
& + m_\pi^2 (m_N + m_\rho)). \tag{8.6}
\end{aligned}$$

8.3 Appendix C

Ceres Acceptance function

In this appendix we develop the expression for the acceptance function of the CERES experiment. The kinematics cuts include the pseudo rapidity range, reflecting the angular acceptance of the detector cuts for transverse momenta of the measured e^+ and e^- , as well as the minimum angle between the directions of the e^+ and e^- . The kinematics of the decay is depicted in Fig. 8.1.

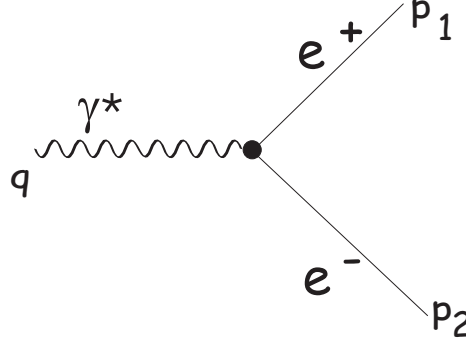


Figure 8.1: The decay of γ^* into a lepton pair.

We use the energy and momentum conservation

$$\begin{aligned} E &= E_1 + E_2, \\ q_{\parallel} &= p_{\parallel 1} + p_{\parallel 2}, \end{aligned} \tag{8.7}$$

where

$$\begin{aligned} E &= m_{\perp} \cosh(y), & E_{1,2} &= p_{\perp 1,2} \cosh(y_{1,2}), \\ q_{\parallel} &= m_{\perp} \sinh(y), & p_{\parallel 1,2} &= p_{\perp 1,2} \sinh(y_{1,2}), \end{aligned} \tag{8.8}$$

with y denoting the rapidity of γ^* , and $m_{\perp} = \sqrt{m^2 + q_{\perp}^2}$. Next, from the relation $q_{\perp} = p_{\perp 1} + p_{\perp 2}$ we obtain

$$p_{\perp 2} = \sqrt{q_{\perp}^2 + p_{\perp 1}^2 - 2q_{\perp} p_{\perp 1} \cos \xi}, \tag{8.9}$$

where ξ is the angle between q_{\perp} and $p_{\perp 1}$. Solving Eqs. 8.7 with the help of Eq. 8.8 we obtain the solution for the rapidities of e^+ and e^- of the form

$$\begin{aligned} \sinh(y_1)^{(1),(2)} &= \frac{1}{2m_{\perp} p_{\perp 1}} \sinh(y) (m_{\perp}^2 + p_{\perp 1}^2 - p_{\perp 2}^2) \pm \\ &\pm \sqrt{m_{\perp}^4 - 2(p_{\perp 1}^2 + p_{\perp 2}^2)m_{\perp}^2 + (p_{\perp 1}^2 - p_{\perp 2}^2)^2} \cosh(y), \end{aligned} \tag{8.10}$$

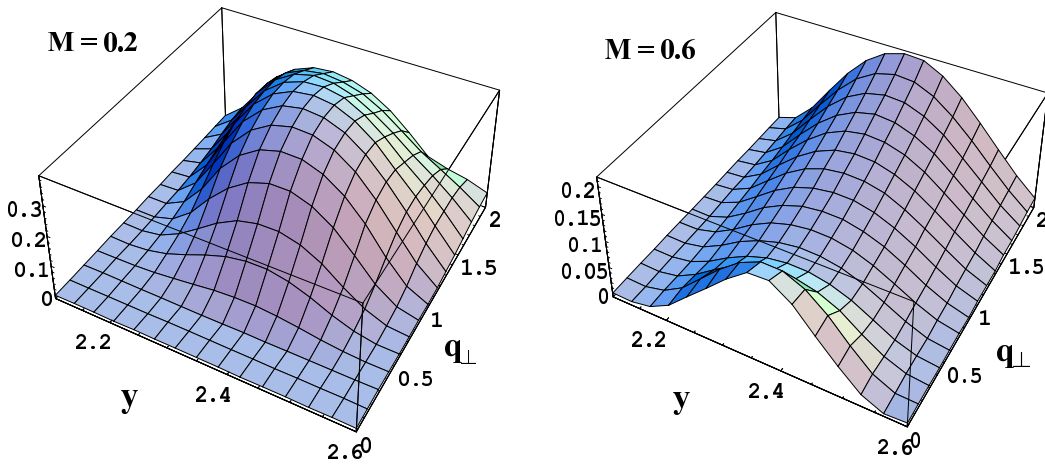


Figure 8.2: The Ceres acceptance function for different value of M , left-hand side $M = 0.2$, right-hand side $M = 0.6$.

and

$$\begin{aligned} \sinh(y_2)^{(1),(2)} &= \frac{1}{2m_{\perp}p_{\perp 2}} \sinh(y)(m_{\perp}^2 - p_{\perp 1}^2 + p_{\perp 2}^2) \pm \\ &\pm \sqrt{m_{\perp}^4 - 2(p_{\perp 1}^2 + p_{\perp 2}^2)m_{\perp}^2 + (p_{\perp 1}^2 - p_{\perp 2}^2)^2} \cosh(y). \end{aligned} \quad (8.11)$$

The (1) and (2) label the two possible branches (the situation is similar to the case discussed in Chapter 2, section 2.3.) These solutions are real if the condition

$$\sqrt{m_{\perp}^4 - 2(p_{\perp 1}^2 + p_{\perp 2}^2)m_{\perp}^2 + (p_{\perp 1}^2 - p_{\perp 2}^2)^2} > 0, \quad (8.12)$$

is fulfilled. The upper limit for the integration over $p_{\perp 1}$ we obtain when $\xi = 0$ in Eq. 8.9. Then

$$p_{\perp 1} = \frac{1}{2}(q_{\perp} + \sqrt{m^2 + q_{\perp}^2}). \quad (8.13)$$

The Ceres acceptance function is

$$Acc(M, y, q_{\perp}) = \frac{\int d^2p_{1\perp} d^2p_{2\perp} dy_1 dy_2 \phi \delta(E_q - E_{p_1} - E_{p_2}) \delta^{(3)}(\mathbf{q} - \mathbf{p}_1 - \mathbf{p}_2)}{2\pi}, \quad (8.14)$$

Using $\delta^{(3)}(\mathbf{q} - \mathbf{p}_1 - \mathbf{p}_2) = \delta^{(2)}(\mathbf{q}_{\perp} - \mathbf{p}_{\perp 1} - \mathbf{p}_{\perp 2})\delta(q_{\parallel} - p_{\parallel 1} - p_{\parallel 2})$, where the two dimensional delta eliminates integration over $p_{\perp 2}^2$, we are left with

$$\delta(E_q - E_{p_1} - E_{p_2})\delta(q_{\parallel} - p_{\parallel 1} - p_{\parallel 2}) = \frac{\sum_{i=1}^2 \delta(y_1 - y_1^{(i)})\delta(y_2 - y_2^{(i)})}{p_{\perp 1}p_{\perp 2}\cosh(y_1 - y_2)}. \quad (8.15)$$

In Eq. 8.14, ϕ is the product of step functions which includes the experimental cuts, such as $2.1 < y_{1,2} < 2.65$, $p_{\perp 1,2} > 200$ MeV, $\theta_{ee} > 35$ mrad. It has the explicit form

$$\begin{aligned} \phi &= \Theta(y_1 - 2.1)\Theta(2.65 - y_1)\Theta(y_2 - 2.1)\Theta(2.65 - y_2)\Theta(p_{\perp 1} - 0.2)\Theta(p_{\perp 2} - 0.2) \times \\ &\times \Theta\left[\cos(0.35) - \frac{p_{\perp 1}p_{\perp 2} + p_{\perp 1}\sinh y_1 p_{\perp 2}\sinh y_2}{p_{\perp 1}\cosh y_1 p_{\perp 2}\cosh y_2}\right] \end{aligned} \quad (8.16)$$

As an example in Fig. 8.2, we show a plot of $Acc(M, y, q_\perp)$ for different values of mass M . We calculate the CERES acceptance function using the Monte Carlo integration method in Fortran.

8.4 Appendix D

We are going to proof that the diagrams of Fig. 2.3 with more than one S_D propagator vanish for kinematic reasons. We write the two nucleon density propagators, S_{D1} and S_{D2} in the following way

$$S_{D1} = i(\gamma^\mu k_\mu + m_N) \frac{i\pi}{E_k} \delta(k_0 - E_k) \theta(k_F - |\mathbf{k}|), \quad (8.17)$$

$$S_{D2} = i(\gamma^\mu k_\mu + \gamma^\mu p_\mu + m_N) \frac{i\pi}{E_{k+p}} \delta(k_0 + p_0 - E_{k+p}) \theta(k_F - |\mathbf{k} + \mathbf{p}|). \quad (8.18)$$

From above expressions 8.17 and 8.18 we have

$$k_0 = E_k = \sqrt{\mathbf{k}^2 + m_N^2} \quad \text{and} \quad k_0 + p_0 = E_{k+p} = \sqrt{(\mathbf{k} + \mathbf{p})^2 + m_N^2}, \quad (8.19)$$

thus, after simply calculations, we obtain

$$m_\rho^2 + 2p_0 k_0 = 2 \mathbf{k} \cdot \mathbf{p} \cos \theta, \quad (8.20)$$

with $p_0 = E_p = \sqrt{\mathbf{p}^2 + m_\rho^2}$. We have that

$$\cos \theta = \frac{m_\rho^2 + 2\sqrt{\mathbf{p}^2 + m_\rho^2} \sqrt{\mathbf{k}^2 + m_N^2}}{2 \mathbf{k} \cdot \mathbf{p}} > 1, \quad (8.21)$$

which ends the proof.

Bibliography

- [1] G. E. Brown and M. Rho, Phys. Rev. Lett. **66** (1991) 2720
- [2] S. A. Chin, Ann. Phys. (NY) **108** (1977) 301
- [3] T. Hatsuda, H. Shiomi, and H. Kuwabara, Prog. Theor. Phys. **95** (1996) 1009
- [4] CERES Collab., G. Agakichiev *et al.*, Phys. Rev. Lett. **75** (1995) 1272
- [5] HELIOS/3 Collab., M. Masera *et al.*, Nucl. Phys. **A590** (1995) 93c
- [6] A. Martin for the CERES collaboration, nucl-ex/0406007 (2004)
- [7] L. S. Celenza, A. Pantziris, C. M. Shakin, and W.-D. Sun, Phys. Rev. **C45** (1992) 2015
- [8] M. Herrmann, B. L. Friman, and W. Noerenberg, Nucl. Phys. **A560** (1993) 411
- [9] M. Herrmann, B. L. Friman, and W. Noerenberg, Nucl. Phys. **A545** (1992) 267C
- [10] A. Mishra, J. Reinhardt, H. Stoker, and W. Greiner, Phys.Rev. **C66** (2002) 064902
- [11] T. Renk and A. Mishra, Phys.Rev. **C69** (2004) 054905
- [12] A. Bieniek, A. Baran, and W. Broniowski, Phys.Lett. **B526** (2002) 329
- [13] G. Agakichiev *et.al*, Nucl. Phys. **A610** (1996) 317c
- [14] G. Agakichiev *et.al*, Phys. Lett. **B422** (1998) 405
- [15] NA38 collaboration, S. Ramos, Nucl. Phys. **A590** (1995) 93c
- [16] NA30 collaboration, M. C. Abreu *et al.*, Phys. Lett. **B368** (1996) 230
- [17] NA50 collaboration, M. C. Abreu *et al.*, Nucl. Phys. **A610** (1996) 331

- [18] H. Satz, hep-ph/0405051 (2004)
- [19] DLS collaboration, R. J. Porter *et al.*, Phys. Rev. Lett **79** (1997) 1229
- [20] DLS collaboration, W. K. Wilson *et al.*, Phys. Rev. **C57** (1997) 1865
- [21] G. Q. Li, C. M. Ko, and G. E. Brown, Nucl. Phys. **A606** (1996) 568
- [22] G. Q. Li, C. M. Ko, and G. E. Brown, Phys. Rev. Lett. **75** (1995) 4007
- [23] W. Cassing, W. Ehehalt, and C. M. Ko, Phys. Lett. **B363** (1995) 35
- [24] T. Hatsuda and S. H. Lee, Phys. Rev. **C46** (1992) R34
- [25] S. Leupold, W. Peters, and U. Mosel, Nucl. Phys. **A628** (1998) 311
- [26] R. Rapp and J. Wambach, Eur. Phys. J. **A6** (1999) 415
- [27] R. Rapp and E. Shuryak, Phys. Lett. **B473** (2000) 13
- [28] *Hadrons in Nuclear Matter*, edited by H. Feldmaier and W. Noerenberg (GSI, Darmstadt, 1995), proc. Int. Workshop XXIII on Gross Properties of Nuclei and Nuclear Excitations, Hirschegg, Austria, 1995
- [29] Quark matter '97. Ultra-relativistic nucleus nucleus collisions. Proceedings, 48th Yamada Conference, 13th International Conference, Tsukuba, Japan, December 1- 5, 1997, edited by T. Hatsuda, Y. Miake, K. Yagi, and S. Nagamiya, Nucl. Phys. **A638** (1998) 1
- [30] Quark matter '99. Proceedings, 14th International Conference on ultra-relativistic nucleus nucleus collisions, Torino, Italy, May 10-15, 1999, edited by L. Riccati, M. Masera, and E. Vercellin, Nucl. Phys. **A661** (1999) 1
- [31] H.-C. Jean, J. Piekarewicz, and A. G. Williams, Phys. Rev. **C49** (1994) 1981
- [32] M. Herrmann, B. L. Friman, and W. Noerenberg, Z. Phys. **A343** (1992) 119
- [33] B. Friman and H. J. Pirner, Nucl. Phys. **A617** (1997) 496
- [34] M. Urban, M. Buballa, R. Rapp, and J. Wambach, Nucl. Phys. **A641** (1998) 433
- [35] M. Urban, M. Buballa, R. Rapp, and J. Wambach, Nucl. Phys. **A673** (2000) 357

- [36] R. Rapp, G. Chanfray, and J. Wambach, Nucl. Phys. **A617** (1997) 472
- [37] M. Post, S. Leupold, and U. Mosel, preprint (2000), nucl-th/0008027
- [38] W. Peters, M. Post, H. Lenske, S. Leupold, and U. Mosel, Nucl. Phys. **A632** (1998) 109
- [39] S. Leupold and U. Mosel, Prog. Part. Nucl. Phys. **42** (1999) 221
- [40] S. Gao, C. Gale, C. Ernst, H. Stocker, and W. Greiner, Nucl. Phys. **A661** (1999) 518
- [41] B. D. Serot and J. D. Walecka, Advances in Nuclear Physics **16** (1986) 1
- [42] S. H. Lee, Nucl. Phys. **A670** (2000) 119
- [43] P. Fachini, J. Phys. **G30** (2003) S565
- [44] V. L. Eletsky, B. L. Ioffe, and J. I. Kapusta, Eur. J. Phys. **A3** (1998) 381
- [45] B. Friman, Acta Phys. Pol. **B29** (1998) 3195
- [46] M. Lutz, B. Friman, and G. Wolf, Nucl. Phys. **A661** (1999) 526
- [47] J. D. Walecka, Ann. of Phys. **83** (1974) 491
- [48] C. J. Horowitz and B. D. Serot, Nuclear Physics **A368** (1981) 503
- [49] C. J. Horowitz and B. D. Serot, Phys. Lett. **B140** (1984) 181
- [50] T. D. Cohen, R. J. Furnstahl, and D. K. Griegel, Phys. Rev. **C45** (1992) 1881
- [51] X. Jin and D. Leinweber, Phys. Rev. **C52** (1995) 3344
- [52] M. Asakawa and C. Ko, Nucl. Phys. **A560** (1993) 399
- [53] V. L. Eletsky and B. L. Ioffe, Phys. Rev. Lett. **78** (1997) 1010
- [54] C. Gale and B. Lichard, Phys. Rev. Lett. **D49** (1994) 338
- [55] C. Song and V. Koch, Phys. Rev. **C54** (1996) 3218
- [56] B. Krippa, Nucl. Phys. **A672** (2000) 270
- [57] W. Broniowski, W. Florkowski, and B. Hiller, Acta Phys. Pol. **B30** (1999) 1079
- [58] W. Broniowski, W. Florkowski, and B. Hiller, Eur. Phys. J. **A7** (2000) 287

- [59] W. Broniowski, W. Florkowski, and B. Hiller, in *Hadron Physics: Effective theories of low-energy QCD, Coimbra, Portugal, September 1999, AIP Conference Proceedings*, edited by A. H. Blin *et al.* (AIP, Melville, New York, 2000), Vol. 508, p. 218, nucl-th/9910057
- [60] W. Broniowski, W. Florkowski, and B. Hiller, Nucl. Phys. **A696** (2001) 870
- [61] W. Rarita and J. Schwinger, Phys. Rev. **60** (1941) 61
- [62] M. Benmerrouche, R. M. Davidson, and N. C. Mukhopadhyay, Phys. Rev. **C39** (1989) 2339
- [63] T. O. E. Ericson and W. Weise, *Pions and nuclei* (Clarendon Press, Oxford, 1988)
- [64] J. A. G. Tejedor and E. Oset, Nucl. Phys. **A571** (1994) 667
- [65] C.-Y. Ren and M. Banerjee, Phys. Rev. **C41** (1990) 2370
- [66] G. Hohler and E. Pietarinen, Nucl. Phys. **B95** (1976) 1
- [67] V. Pascalutsa and R. Timmermans, Phys. Rev. **C60** (1999) 042201
- [68] T. R. Hemmert, B. R. Holstein, and J. Kambor, J. Phys. G **G24** (1998) 1831
- [69] H. Haberzettl, preprint (1998), nucl-th/9812043
- [70] R. Merting and F. Orellana, <http://www.feyncalc.org>
- [71] W. Broniowski, W. Florkowski, and B. Hiller, Acta Phys. Polon. **B30** (1999) 1079
- [72] W. Florkowski and W. Broniowski, Nucl. Phys. **A651** (1999) 397
- [73] R. Rapp and J. Wambach, Adv. Nucl. Phys **25** (2000) 1
- [74] C. A. Dominguez and M. Loewe, Z. Phys. **C49** (1991) 423
- [75] E. L. Bratkovskaya and C. M. Ko, Phys. Lett. **B445** (1999) 265
- [76] R. Rapp, G. Chanfray, and J. Wambach, Phys. Rev. Lett. **76** (1996) 368
- [77] E. Shuryak, hep-ph/0405066 (2004)
- [78] M. Gyulassy and L. McLerran, nucl-th/0405013 (2004)

- [79] T. Matsui and H. Satz, Phys. Lett. **B178** (1986) 416
- [80] S. Gavin and R. Vogt, Nucl. Phys. **A610** (1996) 442c
- [81] D. Kharzeev, Nucl. Phys. **A610** (1996) 418c
- [82] J. P. Blaizot, Nucl. Phys. **A610** (1996) 452c
- [83] P. Braun-Munzinger, I. Heppe, and J. Stachel, Phys. Lett. **B465** (1999) 15
- [84] M. Bourguin and J.M. Gaillard, Nucl.Phys. **B114** (1976) 334
- [85] T. Alber *et al.*, Nucl.Phys. **A566** (1994) 35c
- [86] N. Kroll and W. Wada, Phys.Rev **98** (1955) 1355
- [87] L.S. Landsberg, Phys.Rep **128** (1985) 301
- [88] G.J. Gounaris and J.J. Sakurai, Phys.Rev **21** (1968) 244
- [89] P. M. A. G. Hering, nucl-ex/0203004 (2002)
- [90] D. Adamova, G. Agakichiev, *et al.*, nucl-exp/0209024. (2004)
- [91] HELIOS-1 collaboration, T. Akesson *et al.*, Z. Phys. **C68** (1995) 47
- [92] G. Q. Li and C. M. Ko and G. E. Brown and H. Sorge, Nucl. Phys. **A611** (1996) 539
- [93] HELIOS-2 collaboration, T. Akesson *et al.*, Z. Phys. **C51** (1990) 369
- [94] K. Ozawa *et al.*, Phys.Rev.Lett. **86** (2001) 5019
- [95] J. Friese, for HADES collaboration, Nucl. Phys. **A654** (1999) 1017c
- [96] W. Cassing and W. Ehehalt and I. Kralik, Phys. Lett. **B377** (1996) 5
- [97] J. Kapusta, D. Kharzeev, and L. McLerran, Phys. Rev. **D53** (1996) 5028
- [98] Z. Huang and X. N. Wang, Phys. Rev. **D53** (1996) 5041
- [99] C. Gale and J. Kapusta, Phys. Rev. **C35** (1987) 2107
- [100] C. Song, V. Koch, S. H. Lee, and C. M. Ko, Phys. Lett. **B366** (1996) 379
- [101] K. Haglin, Phys. Rev. **C53** (1996) R2606
- [102] J. Murray, W. Bauer, and K. Haglin, Phys. Rev. **C57** (1998) 492

- [103] C. M. Hung and E. V. Shuryak, Phys. Rev. **C56** (1997) 453
- [104] Y. Kluger and V. Koch and J. Randrup and X. N. Wang, Phys. Rev. **C57** (1998) 208
- [105] Particle Data Group, Phys. Rev. **D66** (2002) 010001
- [106] P. Koch, Z. Phys. **C57** (1993) 283
- [107] R. A. Schneider and W. Weise, Eur. Phys. J. **A617** (1997) 472
- [108] R. Baier, M. Dirks, and K. Redlich, Phys. Rev. **D55** (1997) 4344
- [109] A. Bieniek, nucl-th/0401022 (2004)